TUNABLE FLUORESCENT ORGANIC SALTS FOR IMAGING AND THERAPY

By

Deanna May Broadwater

A DISSERTATION

Submitted to
Michigan State University
in partial fulfillment of the requirements
for the degree of

Biochemistry and Molecular Biology – Doctor of Philosophy

2022

ABSTRACT

TUNABLE FLUORESCENT ORGANIC SALTS FOR IMAGING AND THERAPY

By

Deanna May Broadwater

Cancer remains a leading cause of death worldwide and many treatments still rely on non-targeted chemotherapy, which has inadequate efficacy and is plagued by toxic side effects. A promising solution is photodynamic therapy (PDT), a noninvasive clinical cancer treatment that combines a light activated photosensitizer (PS) with excitatory light to generate toxic reactive oxygen species (ROS). These photoactive agents can also produce detectable wavelengths of light upon photoactivation, which has been used clinically to image tumors in cancer diagnostics and image-guided surgery. Having uses as both diagnostic and therapeutic agents, these molecules are known as theranostics. However, current light-activated theranostics are limited by low brightness, poor tissue penetration, and nonspecific cytotoxicity independent of light excitation. Due to these obstacles, PDT is currently limited to precancerous lesions, superficial neoplastic tissue, or palliative care. Therefore, improved theranostic agents are needed. Prevailing efforts to improve existing photoactive agents focus on chemical modifications that cannot independently control electronic properties (which dictate toxicity) from optical properties. To overcome these limitations, work in this dissertation develops a novel counterion pairing platform to modulate the toxicity of organic salts composed of a photoactive cationic heptamethine cyanine (Cy^+) and a non-photoactive anion. These counterion-tuned fluorescent organic salts can be designed to be either nontoxic for imaging, or phototoxic for PDT. Organic salts self-organize into

nanoparticles with shifted frontier molecular orbital levels dependent on the counterion while the bandgap remains the same. This allows for tuning of electronic properties without affecting optical properties. Improvements in these areas could expand light-activated theranostics into a wider range of cancers and improve patient outcomes.

This dissertation will begin with a review of current photoactive agents used in cancer therapy and ongoing challenges to the adoption of PDT as a frontline therapy. Modern PDT regimens and potential combinatorial therapies will be appraised, and recent advances in rational PS design will be highlighted. Initial *in vitro* studies investigated the optoelectronic tuning capabilities of counterion pairing in human lung carcinoma (A549) and melanoma (WM1158) cell lines. Viability assays establish that pairings with weakly coordinating bulky anions could generate organic salts that are non-cytotoxic and selectively phototoxic, while pairing with standard hard anions yield cytotoxic organic salts. These studies demonstrate that anion pairing can be exploited to shift energy levels and influence ROS generation to either enhance photokilling of cancer cells or improve cell imaging. Organic salts were further investigated in a metastatic breast cancer mouse model to characterize biodistribution, antitumor efficacy within a complex tumor microenvironment, and off-site toxicity. *In vivo* experiments confirm that counterion tuning can generate a selectively phototoxic antitumor PS which abolishes tumor growth and reduces metastasis without systemic toxicity in a breast cancer mouse model. Overall, this work demonstrates the utility of using counterion tuning to control phototoxicity, and further demonstrates the untapped potential of photoactive theranostic agents for clinical cancer therapy.

This work is dedicated to my mother and father:
one taught me a passion for science,
one taught me how to laugh,
both have always been unfailingly supportive
in their own unique way

ACKNOWLEDGMENTS

Over the course of my PhD I have been gifted with support from a number of individuals, unfortunately too many to list entirely by name. I am humbled and eternally grateful to the people who took the time to nurture my growth as a scientist and as an individual. Whether it was working together late into the night, or being understanding over my absences, this thesis would not have been accomplished without a vast network of support.

I would be remiss to not first thank the Lunt Lab, who have provided a rigorous scientific environment for me to learn and grow. None of this would be possible without my advisor, Dr. Sophia Lunt. Thank you for your guidance in both science and the hurdles of graduate school. You have been a supportive presence in a very tumultuous time, and I am forever grateful. Thank you for believing in my project and me, even when I did not. I have been privileged to work alongside a number of exceptional scientists and people in my lab - especially Mayank Jayaram, Elliot Ensink, Dr. Martin Ogrodzinski, Dr. Hyllana Medeiros, and Dr. Shao Thing Teoh. I would like to especially thank Marty and Shao. We all joined the lab within a year of each other, and the four years we spent discussing science, life, and wine together will forever be a highlight in my memories. As you have moved on to even greater opportunities, the last year without you has been difficult, but the skills and encouragement you provided have allowed me to finish this process. I would not be the scientist or the person I am today without your guidance, help, and humor. Hyllana, even though our time together has been briefer, your patience, encouragement, and scientific insight has been integral for

my scientific progress. I have also worked closely with my committee member and collaborator Dr. Richard Lunt; you have been a true scientific role model with your enthusiasm for research, any kind of knowledge, and scientific rigor. I would also like to thank my fellow graduate student Matt Bates for following this project wherever it went with me. I have had the privilege of working with number exceptional collaborators who exposed me to a wide range of science and thinking, including Dr. Babak Borhan, without whom much of this thesis work would not have been possible.

Michigan State University has provided me with a vast array of resources that have allowed me to pursue research and fueled my growth as a scientist. The faculty I learned from have both molded and tested my scientific prowess. I would especially like to thank the remainder of my committee: Dr. Rick Neubig, Dr. Tim Zacharewski, and Dr. Michaela TerAvest - your patience while listening to me talk for hours and crucial feedback are deeply appreciated. Completion of this dissertation would not have been possible without the support of the Department of Biochemistry and Molecular Biology, particularly Dr. David Arnosti and Jessica Lawrence for all the help they provide to graduate students. I would also like to thank my sources of technical and financial support over the years: campus animal resources, the investigative histopathology laboratory, the mass spectrometry and metabolomics core, Spartan Innovations, and the Aitch Foundation. I would especially like to thank Lauren Aitch, who reminded me of the personal weight of cancer on our society and why we work so hard.

The highs and lows of graduate school have made me appreciate even more the loving support system I have around me. Thank you for your unconditional faith in me and grounding me to what is truly important. To my parents Michael and Laurie, thank

you for your decades of effort shaping the person I am today. Thank you to my brothers - Philip, Cory, and Jason, who have always made sure I never took myself or my problems too seriously. To my fellow graduate students and dear friends - Reid, Hannah, and Lisa; I could not have accomplished this without you cheering for me from the sidelines. I am so excited to watch you succeed in all your future endeavors. To my fluffy companions, Reesie and Finn, thank you for always making sure I received plenty of sunshine and exercise, and keeping me company writing late into the night. Adam and Beau, thank you for providing a stable environment of love and support for me to complete this adventure in. This process has reminded me how surrounded and blessed by love I am, thank you all so much.

TABLE OF CONTENTS

LIST OF TABLES xi

LIST OF FIGURES xii

KEY TO ABBREVIATIONS xv

CHAPTER 1. CURRENT ADVANCES IN PHOTOACTIVE AGENTS FOR IMAGING AND THERAPY 1
1.1 PREFACE 2
1.2 Abstract 3
1.3 Background 3
1.4 Clinical Indications 9
1.5 First-Generation Photosensitizers 13
1.6 Second-Generation Photosensitizers 14
1.7 Third-Generation Photosensitizers 19
1.7.1 Fluorescent small molecules 19
1.7.2 Nanomedicine 20
1.8 Mode of Action 27
1.9 Targeting 30
1.9.1 Passive targeting 30
1.9.2 Active targeting 31
1.10 Light Dosing Regimens 32
1.11 Resistance Mechanisms 33
1.12 Combinatorial Therapy 36
1.12.1 Impairment of Cellular Redox 36
1.12.2 Ferroptosis 37
1.12.3 Tumor Sensitization 38
1.12.4 Immunostimulators 39
1.13 Conclusions and Future Outlook 40
1.14 Acknowledgments 41
1.15 Dissertation Goals 41
REFERENCES 45

CHAPTER 2. MODULATING CELLULAR CYTOTOXICITY AND PHOTOTOXICITY FOR IMAGING AND THERAPY 63
2.1 PREFACE 64
2.2 Abstract 65
2.3 Introduction 65
2.4 Results 71
2.4.1 Characterization of fluorescent organic salts 71
2.4.2 Tunable cellular toxicity 76
2.4.3 Mechanism of toxicity 78

2.4.4 Applications in imaging 85
2.5 Discussion 87
2.6 Methods 90
2.6.1 Synthesis 90
2.6.2 Cell culture 92
2.6.3 Viability studies 92
2.6.4 Fluorescent imaging 93
2.6.5 Flow cytometry 94
2.6.6 Ultraviolet visible spectroscopy 94
2.6.7 Zeta potential measurements of nanoparticles 95
2.6.8 Scanning electron microscopy 95
2.6.9 Small-angle x-ray scattering 96
2.6.10 Differential pulse voltammetry 96
2.6.11 Photoluminescence 97
2.6.12 Quantum yield 97
2.6.13 Determination of intracellular organic salt concentrations 97
2.6.14 *In vivo* imaging 99
2.6.15 Statistical analysis 99
2.7 Acknowledgments 100
2.8 Author Contributions 100
APPENDIX 101
REFERENCES 105

CHAPTER 3. COUNTERION TUNING OF NIR ORGANIC SALTS IMPROVES PHOTOTOXICITY TO INHIBIT TUMOR GROWTH IN A METASTATIC BREAST CANCER MODEL 110
3.1 PREFACE 111
3.2 Abstract 112
3.3 Introduction 112
3.4 Results 117
3.4.1 Counterion tuning of organic salts controls toxicity during photodynamic therapy of mouse metastatic mammary cancer cells *in vitro* 117
3.4.2 Oatps and albumin mediate cellular uptake of organic salts 118
3.4.3 Organic salts display differential *in vivo* biodistribution 124
3.4.4 CyFPhB is a selectively phototoxic antitumor agent when combined with NIR irradiation 127
3.4.5 CyFPhB + NIR antitumor treatment has minimal side effects to normal tissue 133
3.5 Discussion 137
3.6 Methods 140
3.6.1 Synthesis and purification of organic salts 140
3.6.2 Cell culture conditions 141
3.6.3 Cell viability studies 141
3.6.4 Kinetic inhibition studies 142
3.6.5 Endocytosis inhibition studies 142
3.6.6 Ultraviolet visible spectroscopy 143

3.6.7 Bovine serum albumin uptake studies 143
3.6.8 Photoluminescence 143
3.6.9 Orthotopic cancer model 144
3.6.10 *In vivo* imaging 144
3.6.11 Photodynamic therapy 145
3.6.12 Histology 146
3.6.13 Ki67 nuclei staining assessment 146
3.6.14 TUNEL-area quantification 147
3.6.15 AST and ALT assays 147
3.6.16 Statistical Analyses 147
3.7 Acknowledgments 148
3.8 Author Contributions 148
APPENDIX 149
REFERENCES 152

CHAPTER 4. ADDITIONAL STUDIES 158
4.1 Introduction 159
4.2 Organic salts in a normal breast cancer cell line 159
4.3 Antioxidant rescue studies 161
4.4 Papillary mouse model studies 165
4.5 Cellular uptake of organic salt nanoparticles 167
APPENDIX 174
REFERENCES 176

CHAPTER 5. SUMMARY AND FUTURE DIRECTIONS 179
5.1 SUMMARY 180
5.2 FUTURE DIRECTIONS 182
5.2.1 Exploration of additional fluorescent organic salts 182
5.2.2 Expansion of *in vivo* studies 184
5.2.3 Active targeting moieties and nanoparticle incorporation 187
REFERENCES 191

LIST OF TABLES

Table 1.1 Overview of photosensitizer generations.....9

Table 1.2 Clinically relevant photosensitizers..... 11

Table 1.3 The outcomes and parameters of nanostructured formulations used as theranostics and the potential applications to treat different types of cancer *in vitro* and *in vivo* 25

Table S2.1 Zeta potential changes as a function of counterion pairing 102

Table S2.2 Quantum yields for CyX and Cy7X salts 102

Table S2.3 CyX salts display similar solubilities in water 103

Table S2.4 Toxicity of photoactive cation heptamethine cyanine (Cy^+) is determined by counterion pairing 103

Table S2.5 Intracellular localization of the fluorescent ion in A549 cells does not change with the counterion 104

Table S3.1 Half maximal inhibitory concentrations (IC_{50}) of fluorescent organic salts with and without NIR irradiation in 6DT1 cells 150

Table S3.2 6DT1 gene expression values.....150

Table S3.3 Sigmoidal curve fitting values.....150

Table S3.4 Urinary protein throughout course of PDT.....151

Table S4.1 Brugge Media recipe for culturing MCF10A cells 175

Table S4.2 Theoretical cation and anion elements detectable by TEM-EDS. 175

Table S4.3 Experimental CyI elements detected by TEM-EDS.....175

Table S4.4 Experimental CyTFM elements detected by TEM-EDS 175

LIST OF FIGURES

Figure 1.1 Common reactive oxygen species (ROS) generated during photodynamic therapy 6

Figure 1.2 Overview of the three generations of photosensitizers (PSs) 8

Figure 1.3 Photodynamic therapy (PDT) induces tumor cell death through various mechanisms depending on photosensitizer (PS) localization..... 28

Figure 2.1 Solid state absorption coefficient versus wavelength comparison for an exemplary organic salt ($CySbF_6$) and nanocrystal (PbS), both with bandgap around 1.3 eV..... 67

Figure 2.2 Pairing a fluorescent cation such as heptamethine cyanine (Cy^+) with varying counterions enables tunability in cellular toxicity through optoelectronic control to improve near-infrared (NIR) imaging and photodynamic therapy..... 70

Figure 2.3 Molecular structures of anions investigated in the study 71

Figure 2.4 Differential pulse voltammetry measurements 72

Figure 2.5 Photoluminescence measurements of Cy7X and CyX salts 73

Figure 2.6 UV-vis absorption spectra of A549 cells treated with organic salts 74

Figure 2.7 Nanoparticle size distribution is similar for all nanoparticles 75

Figure 2.8 Nanoparticle lifetime and stability is demonstrated with CyFPhB and CyTPFB 76

Figure 2.9 Organic salts with tunable toxicity can be used to target human cancer cells 77

Figure 2.10 Organic salts with tunable toxicity can be used to target metastatic human melanoma cells 78

Figure 2.11 $CyPF_6$ preferentially accumulates in the mitochondria and lysosomes of cells..... 79

Figure 2.12 Fluorescent organic salts preferentially accumulate in the mitochondria and lysosomes of cells 80

Figure 2.13 Fluorescent organic salts generate mitochondrial superoxide..... 81

Figure 2.14 Levels of intracellular fluorescence in A549 cells at 24 hours 81

Figure 2.15 Different ion pairings display varying degrees of nanoparticle stability in cell media. 82

Figure 2.16 Tunability in phototoxicity is not due to cellular accumulation or counterion toxicity. 83

Figure 2.17 Novel and commercial fluorescent dyes can be tuned to be less toxic for brighter imaging. 86

Figure 2.18 Toxicity of organic salts is directly related to changes in zeta potential..... 88

Figure 3.1 Schematic for a CyTPFB nanoparticle..... 114

Figure 3.2 Fluorescent organic salts can be used as photosensitizing agents to treat breast cancer cells..... 118

Figure 3.3 Addition of Oatps inhibitor bromosulfophthalein (BSP) does not affect organic salt nanoparticle composition or absorption in cell media. 120

Figure 3.4 Organic anion transporter polypeptides (Oatps) mediate cellular uptake of $CyPF_6$, but only partially account for CyTPFB and CyFPhB uptake 120

Figure 3.5 Endocytotic inhibition does not inhibit uptake of organic salts. 122

Figure 3.6 Albumin plays a critical role in organic salt stability and uptake..... 123

Figure 3.7 Absorption (100-%T) data collected with UV-Vis spectroscopy for 5 µM $CyPF_6$, CyFPhB, and CyTPFB with increasing concentrations of bovine serum albumin (BSA) in serum free DMEM, and complete cell media (DMEM + serum)..... 124

Figure 3.8 Photoluminescence spectra of $CyPF_6$ monomers..... 125

Figure 3.9 *In vivo* biodistribution data shows organic salts preferentially accumulate and are retained within 6DT1 tumors..... 126

Figure 3.10 Counterion tuning of organic salts produces a potent photosensitizer (PS) for photodynamic therapy (PDT) in a metastatic breast cancer mouse model..... 128

Figure 3.11 Tumor growth with 3 µmol/kg $CyPF_6$. 129

Figure 3.12 Tumor growth with 1 µmol/kg $CyPF_6$. 130

Figure 3.13 Tumor growth with 1 µmol/kg CyI. 130

Figure 3.14 Tumor growth with 5 μmol/kg CyFPhB. 131

Figure 3.15 CyFPhB irradiated with NIR light induces an antitumor effect via tumor necrosis and impedes cancer progression in a metastatic breast cancer mouse model 132

Figure 3.16 TUNEL assay color thresholds for treatment groups at experimental endpoint (28 days) 134

Figure 3.17 TUNEL assay color thresholds for Vehicle and CyFPhB + NIR treatment groups 3 days after PDT 134

Figure 3.18 Minimal systemic toxicity is observed with CyFPhB + NIR treatment 136

Figure 3.19 Serum levels of liver enzymes AST and ALT..... 137

Figure 4.1 Organic salts in human breast epithelial cell lines 160

Figure 4.2 Antioxidant supplementation does not lead to a rescue effect in PDT studies with CyTPFB in A549 cells..... 162

Figure 4.3 Antioxidant supplementation does not lead to a rescue effect in PDT studies with $CyPF_6$ in A549 cells 164

Figure 4.4 Photodynamic therapy studies in a papillary tumor model..... 166

Figure 4.5 TEM-EDS of organic salt particle mounted on a lacy carbon grid..... 168

Figure 4.6 TEM-EDS detection of intracellular CyTPFB in an A549 cell..... 169

KEY TO ABBREVIATIONS

ABCG2 – ATP-binding cassette super-family G member 2

Abs – Absorbance

ACQ – Aggregation-caused quenching

AIE – Aggregation-induced emission

ALA – Aminolevulinic acid

ALT – Alanine aminotransferase

AST – Aspartate aminotransferase

BSA – Bovine serum albumin

BSP – Bromosulfophthalein

C60 – Buckminsterfullerene

CBN – Carbon-based nanostructure

CCL-22 – C-C motif chemokine 22

CD – Carbon dot

cm – Centimeter

CRT – Calreticulin

CXCL-12 – Stromal cell-derived factor-12

Cy^+ – Heptamethine cyanine cation

Cy7 – Cyanine7 NHS ester

CytC – Cytochrome C

DAMP – Damage-associated molecular pattern

DCM – Dichloromethane

d-CPP – d-type cell-penetrating peptide

DMEM – Dulbecco's modified Eagle's Medium

DMOG – Dimethyloxalylglycine

DMSO – Dimethyl sulfoxide

E – Eosin

ECNT – Evan blue carbon nanotube

EPR – Enhanced permeability and retention

ER – Endoplasmic reticulum

EtNBS – Phenylbenzothiazole

eV – Electron volt

FA – Folic acid

FDA – Food and Drug Administration

FGS – Fluorescence-guided surgery

GEO – Gene expression omnibus

GLUT-1 – Glucose transporter 1

GPH – Gold-nanoshell pegylated magnetic hybrid nanoparticle

GPX – Glutathione peroxidase

GQD – Graphene quantum dot

H – Hematoxylin

HAL – Hexaminolevulinate

HBSS – Hank's buffered salt solution

Her2 – Human epidermal growth factor receptor 2

HIF – Hypoxia-inducible factor

HMBG1 – High mobility group protein B1

Ho – Hoechst

HOMO – Highest occupied molecular orbital

HPLC – High performance liquid chromatography

HSA – Human serum albumin

HSP – Heat shock protein

IACUC – Institute of Animal Care and Use Committee

IC_{50} – Half-maximal inhibitory concentration

ICG – Indocyanine green

IHC – Immunohistochemical

IL-6 – Interleukin 6

iNOS – Inducible nitric oxide synthase

IONP – Iron oxide nanoparticle

J – Joule

Kg – Kilogram

LDL – Low-density lipoprotein

LED – Light-emitting diode

LIF – Leukemia inhibitory factor

LUMO – Lowest occupied molecular orbital

MAL – Methyl aminolevulinate

MeOH – Methanol

ml - Milliliter

ml - Milliliter

mm – Millimeter

mM – Millimolar

mM – Millimolar

MRI – Magnetic resonance imaging

MS – Mass spectrometer

mW – Milliwatt

N – Sample size

NA – Not applicable

nanoGO – Nanographene oxide

NDI – Naphthalene diimide derivative

NF-κB – Nuclear factor–κB

NIR – Near-infrared

nm – nanometer

nM – Nanomolar

NP – Nanoparticle

NR – Nanorod

NS – nanoshell

OATP – Organic anion transporter polypeptide

PAA – Poly(acrylic acid)

PAT – Photoacoustic tomography

PbS – Lead sulfide

PBS – Phosphate buffered saline

PbSe – Lead selenide

PD-1 – Programmed cell death protein 1

PD-L1 – Programmed cell death ligand 1

PDT – Photodynamic therapy

PDX – Patient derived xenograft

PDX – Patient derived xenograft

PEG – Polyethylene glycol

PIT – Photoimmunotherapy

PL – Photoluminescence

PLGA – Poly(lactic-co-glycolic acid)

pO_2 – Intratumoral oxygen pressure

PpIX – Protoporphyrin IX

PS – Photosensitizer

PTT – Photothermal therapy

QY – Quantum yield

Ref – Reference

ROS – reactive oxygen species

RTT – Radiofrequency thermal therapy

s – Second

S – Supplementary

SAXS – Small angle X-ray scattering

SCC – Squamous cell carcinoma

SEM – Scanning electron microscopy

SLN – Sentinel lymph node

SOD – Superoxide dismutase

SUPR – Super-enhanced permeability and retention

SWCNT – Single-walled carbon nanotube

TAZ – Transcriptional coactivator with PDZ-binding motif

TEAD – Transcriptional enhanced associate domain

TNF – Tumor necrosis factor

TRITC – Tetramethyl rhodamine isothiocyanate

TUNEL – Terminal deoxynucleotidyl transferase dUTP nick end labeling

UCNP – Upconversion nanoparticle

UPLC – Ultra-high performance liquid chromatography

UV – Ultraviolet

UV-vis – Ultraviolet-visible spectroscopy

Veh – Vehicle

YAP – Yes-associated protein

µl – Microliter

µl – Microliter

µl – Microliter

µm – Micrometer

µmol – Micromole

µM – Micromolar

CHAPTER 1.

CURRENT ADVANCES IN PHOTOACTIVE AGENTS FOR IMAGING AND THERAPY

1.1 PREFACE

This chapter is a modified version of a previously published article:

> Broadwater D. M., Medeiros H. C. D., Lunt R. R., Lunt S. Y. (2021). Current Advances in Photoactive Agents for Cancer Imaging and Therapy. *Annual Review of Biomedical Engineering*, *23*, 29-60.

1.2 Abstract

Photoactive agents are promising complements for both early diagnosis and targeted treatment of cancer. The dual combination of diagnostics and therapeutics is known as theranostics. Photoactive theranostic agents are activated by a specific wavelength of light and emit another wavelength, which can be detected for imaging tumors, used to generate reactive oxygen species for ablating tumors, or both. Photodynamic therapy (PDT) combines photosensitizer (PS) accumulation and site-directed light irradiation for simultaneous imaging diagnostics and spatially targeted therapy. Although utilized since the early 1900s, advances in the fields of cancer biology, materials science, and nanomedicine have expanded photoactive agents to modern medical treatments. In this review we summarize the origins of PDT and the subsequent generations of PSs and analyze seminal research contributions that have provided insight into rational PS design, such as photophysics, modes of cell death, tumor-targeting mechanisms, and light dosing regimens. We highlight optimizable parameters that, with further exploration, can expand clinical applications of photoactive agents to revolutionize cancer diagnostics and treatment.

1.3 Background

Photoactive agents are materials that absorb light and transform this energy into heat, luminescence, or excited reactive species. Photoactive compounds can be fluorescent (e.g., cyanines), phosphorescent (e.g., porphyrins and phthalocyanines), both fluorescent and phosphorescent (rare), or neither (dark—not luminescent). A dark photoactive compound without luminescence can still generate heat and chemically reactive species. Luminescent agents are generally composed of phosphorescent or

fluorescent emitters, depending on the spin states involved in the emission process; phosphors generally exhibit long-lived (microseconds to milliseconds) luminescence from excited triplet states, whereas fluorophores exhibit short-lived (picoseconds to nanoseconds) luminescence from excited singlet states. Fluorescent and phosphorescent dyes, which absorb light of a specific wavelength and emit light of a different wavelength, offer great potential as both diagnostic and therapeutic agents for cancer treatment. These dyes can be utilized as a photosensitizer (PS) for phototherapy, in which light is used to activate the PS to induce biological damage, a technique commonly known as phototherapy. In the cancer field, phototherapy is a promising minimally invasive alternative to traditional chemotherapy, radiotherapy, and surgical intervention and can be used to treat a variety of cancers (1, 2). As PSs have advanced, they can now also be employed as contrast agents for tumor imaging; this combined application of therapy and diagnostics is commonly termed theranostics (3). Luminescent theranostic agents increase the precision and effectiveness of treatment, as they can detect and treat the tumor while monitoring the pharmacokinetics and pharmacodynamics of the PS injected into the patient (4). This review focuses on the clinical use of PSs as theranostic agents in cancer therapy.

The first use of phototherapy was reported over 3,000 years ago, when ancient Egyptian, Indian, and Chinese civilizations applied light to treat different diseases, including psoriasis, rickets, and vitiligo. Treatments for these diseases generally consisted of ingesting plant and seed extracts followed by exposure to sunlight (5, 6). Modern phototherapy began with Niels Ryberg Finsen, the father of ultraviolet therapy. In 1903, Finsen received the Nobel Prize in Physiology or Medicine for using short-

wavelength light, the Finsen lamp, to treat lupus vulgaris and helped bring phototherapy to mainstream medicine. In 1907, Hermann von Tappeiner and Albert Jodlbauer introduced the term photodynamic action to describe this phenomenon (7), and photodynamic therapy (PDT) is now synonymous with phototherapy.

Agents with distinct mechanisms based on photothermal therapy (PTT) and PDT have been developed. These agents have been used against several targets including tumor tissues, bacteria, and fungi. To cause cell death, the PS generates either heat for PTT or excessive reactive oxygen species (ROS) for PDT (8). In PTT, the heat generated through the PS agent increases the temperature of the surrounding environment, ablating cells through either necrosis or apoptosis depending on the irradiation level (9). PDT requires three basic elements: a PS, light, and bioavailable oxygen in the tissue being treated. The PS absorbs a photon, transforming it from the ground singlet state to an excited singlet state, and then transfers this energy to form ROS. Often there is an intermediate step in which the excited PS first transfers the energy to a triplet state on the PS prior to transferring the energy to form a ROS. The generation of ROS is based on two different photochemical reaction processes, type I and type II PDT. Type I PDT involves an electron transfer reaction between the PS in the singlet excited state with cellular components and the triplet ground state oxygen (O_2), forming free radicals including superoxide anion ($O_2^{\cdot -}$), hydrogen peroxide (H_2O_2), and hydroxyl radicals ($^{\cdot}OH$) (10). In type II PDT, an excited triplet state on the PS transfers its energy directly to oxygen, converting the (O_2) triplet ground state to a reactive singlet oxygen ($^1O_2$) excited state, which can cleave many organic carbon-

carbon bonds or can subsequently generate other known ROS (6, 11) (**Figure 1.1**).

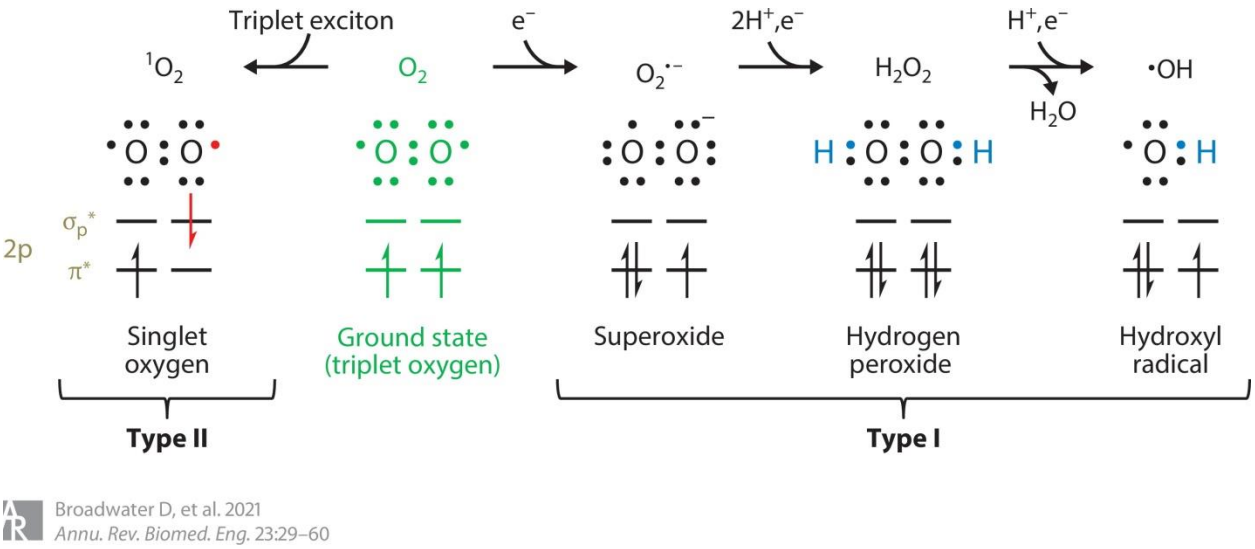

Figure 1.1 Common reactive oxygen species (ROS) generated during photodynamic therapy. Type I photoreactions lead to electron transfer, reacting with oxygen to generate superoxide ($O_2^{\cdot}-$), which can further react to generate hydrogen peroxide (H_2O_2) and hydroxyl radicals ($^{\cdot}OH$). In type II photoreactions, an excited triplet exciton is transferred to the triplet ground state oxygen, generating a highly reactive singlet state oxygen. Collectively, these ROS react with cellular components to induce damage by cleaving, oxidizing, and oxygenating biomolecules

These type II photoreactions require PSs (such as phosphors) with highly efficient intersystem crossing to form triplet exciton species.

Ideal chemical properties for a theranostic PS include high extinction coefficients, chemical stability, water solubility, and long wavelengths for optimal tissue penetrance. Longer wavelengths of light are not as readily absorbed by biological endogenous fluorophores, leading to decreased light scatter and autofluorescence while improving penetrance and resolution, respectively. In biological contexts, an ideal PS should accumulate in tumor tissue while rapidly clearing from the rest of the body. It should

also avoid forming toxic secondary metabolites, be nonmutagenic, and display high phototoxicity (toxicity with light activation) with low cytotoxicity (toxicity in the dark) (12).

PDT has several clinical uses outside of cancer. The facile and immediate delivery of PS and light is ideal for the treatment of superficial dermatologic diseases. It can be used to treat various skin disorders, such as actinic keratosis, photorejuvenation, warts, and acne (13). Phototherapy is also effective for treating infectious diseases. At the beginning of the twentieth century, the first demonstration of photodynamic effect against microorganisms was described by Raab (14), when he used acridine orange and light to induce the death of a paramecium. In 1960, Macmillan and colleagues (15) showed the efficiency of toluidine blue against microorganisms such as bacteria, algae, and yeast. Since the 1990s, studies have shown the efficiency of PDT against microorganisms, and due to microbial resistance to many antibiotics/biocides, photodynamic inactivation and PDT are alternative treatments against bacteria such as Helicobacter pylori, Staphylococcus aureus, and Escherichia coli (16, 17). PDT can also be used to treat fungal and viral infections (18). For example, human papillomavirus infections, which cause genital warts (condyloma acuminate) and increase risk for cervical cancer, can be treated with PDT by using a porphyrin precursor, aminolevulinic acid (ALA) (19, 20).

The US Food and Drug Administration (FDA) has approved several PSs. An overview of first-, second-, and third-generation PSs is shown in **Figure 1.2**, and their characteristics are summarized in **Table 1.1**. For cancer treatment, most FDA-approved agents for PDT are based on the first generation PS, porfimer sodium (Photofrin), a ROS-forming PS that is still in use today. PSs can induce a variety of effects, including

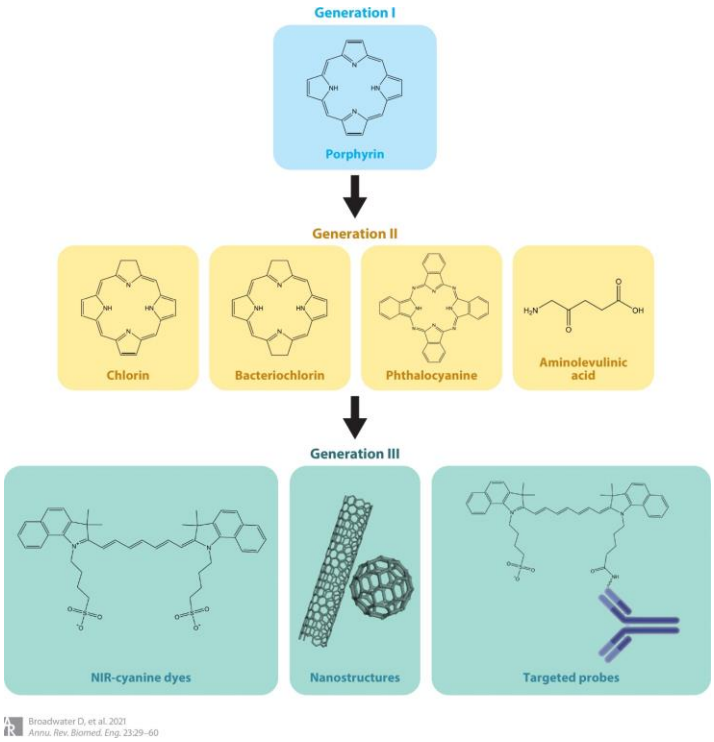

Figure 1.2 Overview of the three generations of photosensitizers (PSs). First-generation PSs are porphyrins, most notably Photofrin. Second-generation PSs include chlorins, bacteriochlorins, phthalocyanines, and aminolevulinic acid prodrugs. Structural differences between porphyrin, chlorin, and bacteriochlorin are highlighted with double bonds in boldface. Third-generation PSs include near-IR (NIR)-cyanine dyes, such as indocyanine green (ICG), and targeted PSs incorporated into nanostructures or bound to tumor-binding moieties, such as ICG-antibody conjugates.

ROS generation, ligand dissociation, toxic chemical reactions independent of oxygen, and PTT. This review focuses specifically on PSs for oxygen-dependent PDT, as they have had the most clinical success and are therefore more widely explored. Unlike PTT, which can damage adjoining tissues with high doses of laser irradiation, PDT can be repeated many times at the same site if needed. Furthermore, toxicity from oxygen-dependent PDT is the most tunable, allowing precise control of cellular toxicity to mitigate off-site tissue damage. Though important, advances made with alternative PSs are outside the scope of this review. We focus on summarizing the foundation of traditional PDT therapy and clinically approved PSs, with particular emphasis on clinical

criteria such as dosage, biological indications, light delivery, and potential combinatorial

	Advances	Abs peak (nm)	Targeting	Mode of action	Structure	Clinical significance	Limitations
First generation	NA	630	Passive	Tumor apoptosis	Oligomeric mixture	Established PDT as a cancer therapy	Low light penetration, skin photosensitivity, poor tissue selectivity, low photostability
Second generation	Deeper wavelength absorption, increased $^1O_2$ generation	630–750	Passive	Tumor apoptosis and necrosis through vasculature destruction	Monomeric	Expanded PDT to a broader range of cancer types	Insolubility, inadequate tumor targeting, incomplete tumor regression
Third generation	Active targeting, multimodal nanodelivery platforms, advanced optical properties	>700	Active	Combinatorial therapies with PDT, PTT, and chemotherapy	Conjugated to targeting moieties and nano-structures	Aims to establish PDT as a frontline cancer therapy	Biocompatibility, aggregation-caused quenching, inadequate clinical data

Table 1.1 Overview of photosensitizer generations. Abbreviations: NA, not applicable; PDT, photodynamic therapy; PTT, photothermal therapy.

therapies. By highlighting advances in the field, we aim to identify key areas where further research is necessary for the extension of photoactive theranostic agents to a wider range of cancer types in order to improve diagnostics, therapy, and overall patient outcomes.

1.4 Clinical Indications

Clinically, fluorescent agents are used for early diagnostics, as intraoperative markers in surgical resection, and for direct tumor treatment via PDT. Currently, PDT with various PSs is clinically approved for obstructive esophageal and lung cancers (worldwide), high-grade dysplasia in Barrett's esophagus (worldwide), mild to moderate actinic keratosis (worldwide), basal cell carcinoma (worldwide), advanced head and

neck cancer (European Union), cutaneous T cell lymphoma (European Union), biliary tract cancer (European Union), and prostate cancer (European Union). These clinically approved PSs are summarized in **Table 1.2** (21, 22). Although several clinical trials have shown effective results, PDT has had a slow transition to frontline cancer treatment. PDT is currently utilized for early intervention of neoplasms or for palliative care (23). PDT is not yet appropriate for major tumor debulking due to the physical limitations of light penetrance and hypoxia common in large tumors (24). Work in the past 10 years has pushed PDT development, demonstrating its use for first-line treatment for small, centrally located tumors, inoperable or widely disseminated tumors, cancers with a high rate of recurrence, and metastasis (23, 25). PDT has the potential to become a potent frontline cancer treatment due to its ability to increase drug delivery, induce cancer cell resensitization to traditional therapies, and trigger the body's antitumor immune response.

In addition to acting as direct antitumor agents, fluorescent molecules are used as real-time imaging probes. Many fluorescence-guided surgery (FGS) trials are utilizing PSs as real-time markers for tumor margins during surgery, allowing physicians to assess tumor growth, aggressiveness, and possible metastasis during tumor debulking. Biopsies can be collected from the stained tumor for fluorescent histological analysis of specific tumor markers, allowing more precise diagnoses in order to determine appropriate treatment strategies (26). Indocyanine green (ICG) is commonly used for sentinel lymph node (SLN) mapping to detect metastasis, and it is also being assessed in clinical trials for improving complete surgical resection in pancreatic, breast, liver, and brain cancers (27–30). This is termed photodynamic diagnostics and has also been

Photosensitizer (brand name)	Chemical family	Localization tissue/cell	Mode of action	Abs (nm)	Cancer type[a]	Year approved	Country	National Clinical Trial no.[b]	Ref
Clinically approved									
Porfimer sodium (Photofrin)	Porphyrin	Tumor and vasculature/mitochondria and lysosomes	Vasculature collapse and tumor apoptosis/necrosis	630	**Lung, esophageal**, bile duct, bladder, brain, ovarian, breast, skin, pancreatic, metastatic	1993	United States, Canada, Japan, Russia, China, EU	NCT01770132, NCT00322699, NCT00513539, NCT03727061, NCT00118222, NCT01262716	189, 190
5-ALA (Gliolan)	Porphyrin precursor	Tumor/mitochondria	Tumor apoptosis	630	**High-grade glioma, actinic keratoses**, bladder, esophageal, skin	2017	United States	None	44, 191, 192
MAL (Metvix)	Porphyrin precursor	Tumor/mitochondria	Tumor apoptosis	630	**Actinic keratoses, nonmelanoma skin**	2004	United States, EU	NCT00473343	193
h-ALA (Hexvix, Cysview)[c]	Porphyrin precursor	Tumor/mitochondria	Tumor apoptosis	360–450	**Bladder**	2010	United States, EU	None	194
Verteporfin (Visudyne)	Porphyrin	Tumor/mitochondria	Tumor apoptosis	690	**Age-related macular degeneration,** pancreatic, breast	2000	United States, Canada, Japan, Russia, China, EU	NCT03033225, NCT02939274	25, 47, 195
Padeliporfin (TOOKAD)	Bacterio-chlorin	Vasculature/cell membrane	Vasculature collapse and tumor starvation	753	**Prostate**, renal	2017	EU	NCT01573156	141
Temoporfin (Foscan)	Chlorin	Tumor and vasculature/multiorgan-elle accumulation	Tumor and vasculature apoptosis with potential systemic immune activation	652	**Head and neck**, lung, brain, bile duct, pancreatic, skin	2001	EU	NCT03003065, NCT01854684	58, 195
Talaporfin (Laserphyrin)	Chlorin	Tumor/mitochondria	ROS-induced tumor apoptosis	660	**Lung**, liver, colon, brain, esophageal	2004	Japan	NCT00122876, NCT00028405	196, 197

Table 1.2 Clinically relevant photosensitizers.

Table 1.2 (cont'd)

Undergoing clinical trials									
HPPH (Photochlor)	Chlorin	Tumor/mitochondria and lysosome	ROS-induced tumor apoptosis	665	Head and neck, esophageal, lung	NA	NA	None	64, 65
Fimaporfin[d]	Chlorin	Tumor/endosome and lysosome	ROS-induced tumor apoptosis	633	Extrahepatic cholangiocarcinoma, colon	NA	NA	NCT04099888	None
Redaporfin	Bacterio-chlorin	Tumor/Golgi apparatus and ER	ROS-induced tumor apoptosis	750	Advanced head and neck	NA	NA	None	63

[a]Cancer types for which photosensitizer treatment has been clinically approved are in boldface, and those for which photosensitizer treatment is undergoing preclinical trials are in regular typeface. [b]The National Clinical Trial number is a unique identification code given to each clinical study registered on https://clinicaltrials.gov/. [c]h-ALA compounds are approved for photodynamic diagnostics of bladder cancer and are undergoing clinical trials for bladder cancer PDT. [d]Fimaporfin is not used as a direct antitumor agent, but is rather used in combination with gemcitabine/cisplatin to induce tumor cell uptake of chemotherapeutics. Abbreviations: 5-ALA, 5-aminolevulinic acid; ER, endoplasmic reticulum; h-ALA, 5-aminolevulinic acid hexyl ester; HPPH, 2-[1-hexyloxyethyl]-2-devinyl pyropheophorbide-α; MAL, methyl aminolevulinate; NA, not applicable; ROS, reactive oxygen species.

applied in bladder cancer with Hexvix (an ALA analog) to identify masses that were initially missed by visual tumor identification during surgery (26). Gliolan, another ALA analog, improved complete surgical resection and progression-free survival in malignant glioma in a randomized, controlled phase III trial and is now approved in the European Union, Japan, and Australia (31, 32). FGS outcomes can also be improved when followed by intraoperative PDT. For example, in a phase II clinical trial for patients with malignant brain tumors, the debulked tumor site was irradiated with excitatory wavelengths following FGS, reducing incomplete resection by PDT-induced phototoxicity of the leading tumor edge, a site commonly missed during surgical removal of tumor tissue. This strategy reduced recurrence and had a 95.5% 12-month overall survival rate with minimal side effects. This finding shows that PDT can be used to delineate tumor margins and protect against recurrence (33, 34). Additionally, PDT has been widely studied as a neoadjuvant therapy; for example, preoperative PDT in non-small-cell lung cancer can increase the number of potential surgery candidates and improve resection completeness (35, 36).

1.5 First-Generation Photosensitizers

First-generation PSs are hematoporphyrins, a heterocyclic macrocycle composed of four interconnected pyrrole subunits derived from hemin. Purified oligomeric mixtures of hematoporphyrins make up Photofrin, the first clinically approved photosensitizing agent. Photofrin was approved by the FDA in 1995 for palliative care of obstructive esophageal and endobronchial non-small-cell lung cancer (37). It is delivered intravenously and rapidly concentrates in the tumor and corresponding vasculature. Endoscope delivery of 630-nm light irradiation is administered to the tumor

48–72 hours following intravenous injection. Photofrin accumulates largely in the mitochondria and lysosomes of cells and induces cell death predominantly via apoptosis (38). Photofrin has been widely explored in clinical trials for other cancers such as lung, pancreatic, head and neck, bile duct, brain, gall bladder, and breast. However, inherent problems such as limited penetrance of excitation wavelengths, chemical instability, hydrophobicity-induced aggregation, low *in vivo* singlet oxygen generation, and offsite accumulation have hindered its diversification into additional cancers and broader establishment as a first-line treatment (39). While Photofrin is still undergoing clinical trials to assess the validity of PDT in a wider range of cancer types, the next generation of PSs are being developed to improve PDT efficacy and selectivity concurrently.

1.6 Second-Generation Photosensitizers

Second-generation PSs were designed to improve upon the limitations of the first-generation hematoporphyrins by exhibiting longer wavelength absorption, increased water solubility, and increased tumor-targeting ability. They are based on the general structures of porphyrin precursors, phthalocyanines, chlorins, and bacteriochlorins, with additional side chains to increase solubility. Whereas Photofrin is an oligomeric mix of hematoporphyrins, second-generation PSs, which are all monomeric mixtures, have faster clearance times and improved intratumoral distribution. Below, we discuss current clinically approved second-generation PSs, which are also summarized in **Table 1.2**.

ALA is the biosynthetic precursor to protoporphyrin IX (PpIX), an endogenous PS used in the synthesis of heme. Photosensitive porphyrins have poor solubility and chemical stability. Use of the water-soluble porphyrin precursor ALA leads to cellular

biosynthesis and substantial accumulation of PpIX (40). Cancer cells accumulate higher amounts of PpIX than normal cells do when dosed with ALA, and subsequent photoactivation with 633 nm of light induces ROS and cell death (41). The photodynamic effect is thought to be mediated by mitochondria- and cytoplasm localized ROS generation in tumor cells and the surrounding vasculature, similar to hematoporphyrins (42). Chemically stable ALA can be delivered topically, as well as orally or intravenously, which has seen great success in localized treatment of precancerous lesions such as actinic keratosis (43). There have been promising clinical trials for bladder cancer: Patients at intermediate or high risk received 50 mL of 8 to 16 mM of hexaminolevulinate (HAL) solution instilled into the bladder following transurethral resection. Following HAL-PDT for 3 months, lesions were absent in 52.9% of patients at 6 months, 23.5% at 9 months, and 11.8% at 21 months (44). Unfortunately, the same results have not been consistently observed with intravenous or oral delivery, which led to offsite accumulation in nerve endings, systemic toxicity, and poor efficacy in clinical trials for prostate cancer (45, 46). This is likely due to variable intratumoral distribution of HAL and oxygen levels, an important diagnostic criterion as discussed above.

Verteporfin is a benzoporphyrin derivative used primarily to treat age-related macular degeneration. It was originally investigated for cancer therapy because of its ability to suppress angiogenesis via vascular destruction, which downregulates genes involved in migration and invasion (47). Verteporfin is rapidly incorporated into plasma low-density lipoprotein (LDL), which allows preferential targeting of cancer and neovascular cells due to increased expression of LDL receptors (48). Once in the tumor

microenvironment, verteporfin accumulates intracellularly within the mitochondria, where it induces ROS-mediated apoptosis following 690-nm light irradiation. It has been reported to inhibit growth by interfering with the binding of yes-associated protein (YAP) and transcriptional coactivator with PDZ-binding motif (TAZ) oncoproteins to the transcriptional enhanced associate domain (TEAD) family of transcription factors, independent of light irradiation (49). Although promising in several *in vitro* studies, verteporfin does not have significant non-photoinduced effects *in vivo* (50–52). However, PDT with verteporfin has shown promise in pancreatic and breast cancers and has moved on to phase II clinical trials (25). Verteporfin is rapidly cleared through the bile, showing decreased photosensitivity and increased penetrance due to the longer wavelength. In the United States, verteporfin is approved for the treatment of macular degeneration and is undergoing clinical trials for the treatment of inoperable pancreatic tumors (NCT03033225) and cutaneous metastases of breast cancer (NCT02939274).

Padeliporfin (TOOKAD) is the third conceptualization of bacteriochlorophylls used for therapeutic PDT. The palladium core of the porphyrin enables greater possibility for excited-state intersystem crossing from the PS's singlet state to the triplet state, which can generate ROS. Padeliporfin has a strong absorbance at 763 nm and accumulates in vasculature-localized prostate tumors while clearing from systemic circulation within a few hours following binding to protein serum albumin (53). In a phase III clinical trial, men with low-risk, localized prostate cancer were given 4 mg/kg of TOOKAD intravenously followed by 753 nm of directed irradiation. At the 24-month follow-up only 28% of men treated with vascular-targeted PDT displayed disease

progression, with minimal side effects (54). Following these illuminating results, TOOKAD was approved in the European Union for the treatment of low-risk prostate cancer, and phase I trials have begun for the treatment of obstructing esophagogastric cancer.

Temoporfin (Foscan) is a reduced porphyrin, a chlorin analog with a red-shifted absorbance at 650 nm, which is more intense than that of Photofrin. Isotopically labeled temoporfin is incorporated into serum lipids and localizes in various cellular organelles, excluding the nucleus (55). Upon irradiation, a large number of vacuolization and structural alterations occur to the Golgi apparatus, endoplasmic reticulum (ER), and mitochondria (56). Similar to many PSs, tumor destruction occurs by direct tumor damage as well as vascular damage and the following immune response. Temoporfin was approved in the European Union in 2001 for palliative care of advanced head and neck squamous cell carcinoma (SCC). This was following a phase III clinical trial in which 53% of patients with recurrent/refractory head and neck SCC saw increased quality-of-life benefits (57). Temoporfin has also been investigated as the primary treatment in head and neck, skin, prostate, thoracic, brain, bile duct, breast, and pancreatic cancers (58).

Talaporfin (Laserphyrin) is a mono-l-aspartyl chlorin specifically designed to have lower clearance time than first-generation PSs. It can absorb longer (664 nm) wavelengths compared with first-generation PSs and demonstrates reduced skin photosensitivity (59). Its antitumor effect is mediated primarily by mitochondrial ROS-induced apoptosis, though it localizes in other cytoplasmic organelles, in a manner similar to that described above with verteporfin (60, 61). These improved qualities have

led to improved therapeutic outcomes when compared with Photofrin for esophageal cancer (62). It was approved in Japan in 2004 for the treatment of lung cancer and is undergoing clinical trials for the treatment of brain, head and neck, esophagus, liver, and metastatic cancers.

Other second-generation PSs also currently under clinical trials are redaporfin, fimaporfin (NCT04099888), and 2-[1-hexyloxyethyl]-2-devinyl pyropheophorbide-α (HPPH) (63–65). All function through ROS-induced apoptosis. Common drawbacks seen in second-generation PSs are insufficient phototoxicity, poor tumor targeting, and insolubility. Although second-generation PSs are chemically purer than first-generation PSs, self-aggregation has made drug delivery and pharmacokinetic analysis difficult. For example, the tendency of temoporfin to aggregate results in variable clearance times and intratumoral distribution (66). Intravascular aggregation complicates the passive tumor targeting on which second-generation PSs rely for tumor accumulation.

Unfortunately, this method of targeting is often not robust enough to mediate complete tumor destruction. When small-molecule second-generation PSs were designed, the primary focus was on increasing *in vitro* singlet oxygen generation, as a means to maximize potential tumor phototoxicity, and intracellular localization. This approach has not translated well to clinical models, as passive tumor targeting does not have the level of specificity desired for frontline therapies, and *in vitro* assessment of singlet oxygen generation does not consider oxygen consumption and intratumoral light scattering (67). Third-generation PSs have focused on tumor targeting, absorption and emission of even longer wavelengths, and improved phototoxicity

1.7 Third-Generation Photosensitizers

Third-generation PSs are currently being designed to improve targeting and advance optical properties including high extinction coefficients, longer wavelength absorbance, and photostability. Wavelengths in the near-infrared (NIR) spectrum (650–1,700 nm) are ideal for *in vivo* imaging, as they are less absorbed by endogenous biological fluorophores (68). This leads to deeper tissue penetration and improved resolution. The NIR-I window refers to wavelengths from 650 to 900 nm, and NIR-II wavelengths range from 1,000 to 1,700 nm (69).

1.7.1 Fluorescent small molecules

Cyanine dyes, which are fluorescent small molecules that can absorb in the UV, visible, or NIR range, have been widely investigated as PSs for PDT (70, 71). ICG, a disulfonated heptamethine cyanine that absorbs at 780 nm, has been utilized since 1959 for medical diagnostics to track hepatic function, blood flow, and tissue and organ perfusion, and in 2015 its use was expanded to cancer diagnostics. Due to its confinement within the vascular system, ICG's primary use in cancer is for detecting abnormal pulmonary drainage indicative of lymphatic metastasis by SLN mapping (27). Although well characterized, ICG suffers from aggregation, short half-life, poor photostability, nonspecific binding, and poor aqueous stability (72). However, the heptamethine scaffold on which ICG is based is promising for the development of alternative theranostic cyanine dyes. The alkyl side chains are easily conjugated to tumor-targeting moieties, addition of a carbocyclic ring increases the rigidity to improve quantum yields, and N-alkyl substitutions can improve phototoxic effects (73). In the past five years, the ability to modify the counterion of promising theranostic cyanine and

rhodamine salts has proved useful in increasing the quantum yield (74–77), forming self-assembling nanoparticles, and modulating the passive cytotoxicity without light irradiation (78, 79). Even more compelling, the organic salt formulation has been used to modulate electronic energy levels independent of the bandgap by way of counterion pairing to selectively generate ROS, enabling precise tunability of both cytotoxicity and phototoxicity (80). Several optimized cyanine dyes are currently undergoing preclinical trials to assess therapeutic efficacy capability (30, 81); however, there are many analogs undergoing clinical trials for diagnostics and FGS (82, 83).

NIR-II small molecules are harder to develop due to their need for increased molecular conjugation, instability, and hydrophobicity. In general, achieving light absorption and emission beyond 1,000 nm is a challenging material design problem, as nonradiative rates typically increase substantially when the conjugation is increased to reach bandgaps in this range. This typically results in low quantum yields of less than 1–10% for photoluminescent emission beyond 1,000 nm (84) and would similarly reduce ROS generation yields as well. Although there have been some recent demonstrations with the development of NIR-II dyes (85, 86), more preclinical work has focused on NIR-I dyes with emission tails that extend past 1,000 nm, such as ICG (87). Additional challenges for NIR-II-based molecules are related to available light sources and imaging cameras with a deep NIR photoresponse, which will need to become more cost-effective and widely available.

1.7.2 Nanomedicine

Nanostructures exhibit one or more dimensions at the nanometer scale, including atomic, molecular, nanocrystal, and nanoparticle assemblies (88). They can offer

specific physicochemical properties; have an increased surface area–to–mass ratio, which alters their reactivity; and possess a great deal of control over particle dimensions (89). They can be grouped on the basis of their class (organic, inorganic, and hybrid), origin (natural or synthetic), ordering (e.g., amorphous nanoparticle versus crystalline nanocrystal versus hierarchical assemblies), and dimensionality (0D, 1D, 2D, and 3D) according to the electron movement along the dimensions in the nanomaterial (90, 91). In the biomedical sciences, nanostructures have shown promise as theranostics, drug carriers, and formulations for drug assembly (92).

Nanoparticles can range from nanometers to several microns in size and can be simple, disordered aggregate ensembles or exhibit hierarchical structures such as with micelles or layered particles. Nanoparticles used as theranostics are primarily organic based, inorganic based, or hybrid composites (93–95). Organic nanoparticles, which can be based on small molecules or polymers, include carbon-based nanostructures (CBNs). CBNs are typically biocompatible, allowing for immune evasion, prolonged blood circulation time, and increased tumor-targeting ability. The most common CBNs used for theranostic purposes, both as direct PSs and as carriers for loading PSs, are graphene, carbon nanotubes, and fullerenes (96). They offer several advantages, including high quantum yield, high stability, and good biocompatibility (97). Although CBNs generally have low toxicity, researchers have raised concerns about their fibrous-like structure (98), which could induce inflammatory and fibrotic reactions, and about mesothelioma or carcinogenic responses in the lining of the lung (99).

Inorganic nanoparticles are predominantly metal (e.g., gold, silver, and aluminum), metal oxides (e.g., titanium oxide, iron oxide, and magnetite), or

semiconductors (e.g., silicon, lead sulfide, and cadmium telluride). Inorganic nanoparticles tend to enable more structural control over exact size and shape and the optical resonance can be tuned to NIR regions (100). However, inorganic nanoparticles are typically less biocompatible with cells, leading to poor penetration and superficial ROS generation. They also often have poor absorption coefficients near the bandgap, causing strong absorption of UV and blue wavelengths despite having a NIR bandgap (101). Common examples of inorganic nanoparticles as theranostics are quantum dots, nanorods, and nanoshells.

Quantum dots are luminescent colloidal nanocrystals (or nanoparticles) usually 1–10 nm in size and are composed of semiconductor materials. They have spatial dimensions smaller than the Bohr radius of the bulk excited state, which impart strong quantum confinement effects leading to blue shifts in absorption and emission (102). Nanorods are rod-like 1D nanostructures between 10 and 120 nm (103). Nanorods and nanoshells have a well-established chemistry, and their localized surface plasmon resonance, which comes from the coupling between the electromagnetic field and the collective oscillations of the free conduction electrons at the nanoparticle surface, can efficiently convert the excited-state photon energy to heat (104, 105). They can be made from metallic and nonmetallic elements, such as carbon, gold, and zinc oxide, among many others. The shape of gold nanostructures, such as nanorods and nanoshells, can not only change the absorption and scattering wavelength from visible to the NIR region but also increase their absorption and scattering cross sections, enabling imaging and PTT in this region with deeper optical penetration in biological tissues (106). Gold nanorods, when under irradiation, are also considered to be

excellent imagers for cancer and localizable heat sources, desirable traits in an imaging and PTT nanostructure (107). However, both gold nanorods and gold nanoshells possess a relatively low specific surface area, which limits drug loading and can induce aggregation, blue-shifting the absorption window and decreasing tissue penetration (108).

Hybrid nanoparticles for therapy typically rely on multimodal drug treatments, such as combining PDT with O_2 economizers/generators, immune activators, ROS generators, and apoptotic inhibitors. Potential combinatorial therapies are discussed in more detail in subchapter 1.12, but nanoparticles offer a clear benefit as a multidrug delivery system. Nanoparticle-mediated PDT allows two antitumor treatments to be combined into one delivery system, improving the synergistic effect compared with independent PSs and chemotherapeutic delivery. This is demonstrated with hybrid nanoparticle C dots, ultrasmall core shell silica nanoparticles, which encapsulate fluorescent molecules and can easily accommodate conjugation of a variety of targeting moieties, notably cyclic (arginine-glycine-aspartic acid-d-tyrosine-lysine) pentapeptide and α-melanocyte stimulating hormone (109, 110). C dots also undergo radiolabeling with ^{124}I, allowing preoperative positron emission tomography imaging as well as real-time fluorescent imaging. C dots have demonstrated tumor-specific accumulation in a minipig model of spontaneous melanoma, in which micrometastases in lymph nodes have been intraoperatively detected in real time (111). C dots are currently undergoing preliminary clinical trials in patients with melanoma or brain tumors to characterize biodistribution and pharmacokinetics (NCT01266096) as well as SLN mapping (NCT02106598). The clinical relevance of these hybrid-composite nanoparticles is

apparent and has the potential to improve surgical diagnostics and therapy. **Table 1.3** provides examples of nanostructures and their uses in theranostic cancer treatment.

Although nanostructures have proven to be efficient in nanomedicine, a common problem of PSs, especially organic dyes, lies in their high hydrophobicity and rigid planar structures. In particular, when PSs are used in the aggregated state or at high concentrations, the intrinsic fluorescence signals are reduced or disappear because of intermolecular π–π stacking (112). This is well known as the aggregation-caused quenching (ACQ) effect. The formation of aggregates results in diminished imaging quality due to the quenched fluorescence. To minimize the ACQ effect, Luo et al. (113) reported in 2001 that a type of luminogen (i.e., silole derivative) exhibited enhanced fluorescence in the aggregated state, and their finding gave rise to the concept of aggregation-induced emission (AIE). AIE is a photophysical phenomenon in which many organic luminophores show dim or no emission in the dissolved state (single molecular state) but show enhanced emission in the aggregated state because of restricted intramolecular motion (114). AIE nanoparticles present some desirable characteristics, such as excellent photostability, high emission efficiency, and efficient ROS generation in the aggregated state for imaged-guided PDT. In addition, AIE nanoparticles are suitable for *in vivo* imaging and have deep penetration ability and strong photobleaching resistance. Currently, AIE nanostructures have emerged for various applications, including cancer theranostics, and can occur as different nanostructures, for example, nanodots, nanorods, C dots, and nanosheets (115–118).

Class	Structure base	Nanostructure	Role of nanostructure	Nanocomplex structure	Main application(s)	Abs (nm)[a]	Cancer type	Remarks	Ref
Carbon	Graphene	nanoGO sheets	Photothermal and drug delivery agent	Methylene blue–loaded Pluronic F127 coating nanoGO	PDT/PTT	655/808	Cervical cancer (HeLa) in vitro, in vivo	Complete tumor regression with no visible necrotic tissue damage	198
		GQDs	Produce singlet oxygen with quantum yield greater than 1	UCNP-GQD/TRITC	PDT	980	Breast cancer (4T1) in vitro, in vivo	Mitochondria-specific PDT with in situ 1O2 generation in mitochondria; tumor inhibition efficacy rate 75.3%	81
	Carbon nanotubes	SWCNTs	Photothermal efficacy, improved cargo loading, improved cell penetration, strong Raman signals	Long circulating albumin-Ce6/ECNTs	Imaging/PDT/PTT	630/808	Head and neck carcinoma (SCC-7) in vitro, in vivo	Diagnostic imaging agent for head and neck carcinoma; PTT/PDT together presented complete tumor eradication in vivo	199
	CDs	AIE	Modulation of morphology and emission of CD intensity	NDI-i-CD-iii[b]	Bioimaging	580	Skin cancer (B16F10 cells) in vitro	Surface-functionalized CDs' emission intensity remarkably enhanced in B16F10 cells	200
Carbon	Fullerene	C60	ROS production (PDT), heat release (PTT), and improved biocompatibility	C60-IONP-PEG-FA[c]	Imaging, PDT, RTT, and magnetic targeting	532	MCF-7 cells/S180 tumor-bearing BALB/c mice	In vitro and in vivo ROS-triggered apoptosis and displayed potential as an MRI contrast agent	201
Inorganic	Quantum dots	Cu2(OH)PO4	Improved NIR photoabsorption and ROS production	Cu2(OH)PO4-@PAA[d]	PDT/PTT/PAT imaging	1,064	Cervical cancer (HeLa cells) in vitro, in vivo	Combinatorial PDT/PTT decreased cell viability by 85% and induced total remission of tumors by photoablation in 80% of mice with IR imaging to monitor therapy	202
	NRs	Metal (e.g., Au) NRs	Photothermal conversion material	Ce6-AuNR@SiO2-d-CPP[e]	PTT/PDT	650/808	Breast cancer (MCF-7) in vitro, in vivo	Prolonged-circulation; mitochondria targeting decreased cell viability and inhibited tumor growth	203
	NSs	Metal (e.g., Au) NSs	NIR light absorption to form localized heat and improved drug release	BGNSH-HSA-ICG-FA[f]	PTT/PDT/chemotherapy and imaging	420/808	Breast cancer (MDA-MB-231 cells) in vitro, in vivo	PDT/PTT decreased cell viability by 80% via apoptosis and high-efficiency in vivo fluorescence imaging	204
Hybrid	NPs	Lipid-encapsulated TPE-PTB	Improved biocompatibility and water dispersity	TPE-PTB	Two-photon imaging/PDT	800	Skin cancer (A375 cells) in vitro, in vivo	Inhibition of tumor growth with no side effects to main organs, potent ROS production (1O2 and ·OH); can image deep (up to 505 μm) tumor tissues	205

Table 1.3 The outcomes and parameters of nanostructured formulations used as theranostics and the potential applications to treat different types of cancer *in vitro* and *in vivo*.

Table 1.3 (cont'd)

	NSs	Au-NSs around PLGA	Combination of PTT and fluorescence imaging	Her2-GPH NPs	Imaging/PTT	808	Breast cancer (SKBR3 cells) in vitro	Decreased cell viability by 20% with anti-Her2 antibodies targeting and high-contrast in vitro imaging	206

[a]Experimental groups were exposed to different wavelengths to achieve the effects of the combined therapy (e.g., synergy of PDT/PTT). [b]Surface-functionalized CDs with l-tyrosine-tagged NDI derivative (NDI-i).[c]C_{60} loaded with IONPs and functionalized with PEG and FA.[d]PAA-coated $Cu_2(OH)PO_4$ quantum dots. [e]Au-NRs coated with the pegylated mesoporous SiO_2 to entrap the PS Ce6 and d-CPP. [f]PLGA biodegradable matrix loaded with the anticancer drug doxorubicin and covered with a porous Au-NS functionalized with HSA, dye ICG, and FA. Abbreviations: C_{60}, Buckminsterfullerene; CD, carbon dot; d-CPP, d-type cell-penetrating peptide; ECNT, Evan blue carbon nanotube; FA, folic acid; GPH, gold-nanoshell pegylated magnetic hybrid nanoparticle; GQD, graphene quantum dot; Her2, human epidermal growth factor receptor 2; HSA, human serum albumin; ICG, indocyanine green; IONP, iron oxide nanoparticle; MRI, magnetic resonance imaging; nanoGO, nanographene oxide; NDI, naphthalene diimide derivative; NIR, near-IR; NP, nanoparticle; NR, nanorod; NS, nanoshell; PAA, poly(acrylic acid); PAT, photoacoustic tomography; PDT, photodynamic therapy; PEG, polyethylene glycol; PLGA, poly(lactic-co-glycolic acid); PS, photosensitizer; PTT, photothermal therapy; ROS, reactive oxygen species; RTT, radiofrequency thermal therapy; SCC-7, squamous cell carcinoma-7; SWCNT, single-walled carbon nanotube; TPE-PTB, 4-(5-(1-(4-(*tert*-butyl)phenyl)-1H-phenanthro[9,10d]imidazol-2-yl)-thiophen-2-yl)-7-(4-(1,2,2-triphenylvinyl)phenyl)benzo[c][1,2,5]thiadiazole; TRITC, tetramethyl rhodamine isothiocyanate; UCNP, upconversion nanoparticle.

1.8 Mode of Action

PDT induces antitumor effects by three main mechanisms: (a) destruction of tumor cells by the generation of ROS, (b) collapse of the tumor vasculature and subsequent nutrient starvation of tumor cells, and (c) activation of the innate immune system against tumor antigens (**Figure 1.3**). Different PSs accomplish these mechanisms to varying degrees and being highly efficient at all three is not necessarily needed or desirable. Early destruction of tumor vasculature inhibits the systemic antitumor immune response and prevents additional drug and oxygen delivery, and highly concentrated ROS generation at the tumor site does not effectively stimulate the innate immune system.

The cell death mechanisms of PSs are influenced by their localization. This can be in the tumor bed, in the tumor vasculature, or directly within the tumor cells. Certain PSs, such as padeliporfin (TOOKAD), have been developed specifically to accumulate in the tumor vasculature and inhibit tumor progression by nutrient starvation (53). This is usually coupled to additional accumulation of PSs in tumor cells. Most second-generation PSs were designed to accumulate within tumor cell organelles to improve tumor destruction. Generation of ROS within mitochondria, Golgi apparatus, ER, and lysosomes can directly initiate apoptosis over a matter of hours. This cleaner form of cell death is thought to be ideal, as the programmed cell death routine releases toxic cellular components in a controlled manner and recognition of the apoptotic marker, phosphatidylserine, by phagocytes suppresses the expression of proinflammatory

cytokines (119). Higher doses of light and drug treatment lead to tumor cell necrosis,

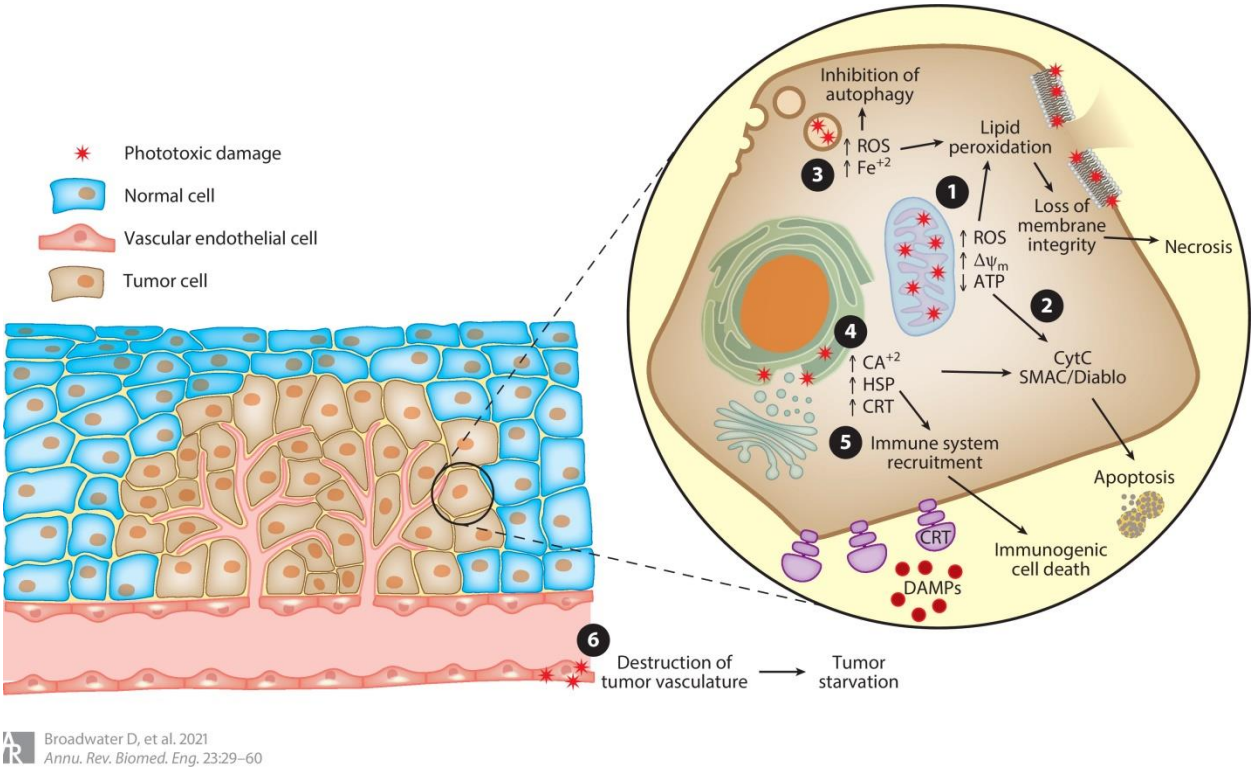

Figure 1.3 Photodynamic therapy (PDT) induces tumor cell death through various mechanisms depending on photosensitizer (PS) localization. PSs that cause direct tumor cell destruction localize in specific cellular organelles, leading to different cell death pathways. (1) PSs that localize in the mitochondria generate reactive oxygen species (ROS) and damage the mitochondria, causing a decrease in ATP levels and depolarization of the mitochondrial membrane potential (ψm). (2) This results in the release and recruitment of proapoptotic proteins [cytochrome C (CytC) and the SMAC/Diablo complex] that initiate apoptosis. (3) PSs that localize in lysosomes also induce ROS while additionally releasing labile iron, which increases cytosolic oxidative damage. Low levels of oxidative damage contribute to apoptosis, and high levels damage membranes to induce necrosis. Furthermore, destruction of lysosomes inhibits autophagy, a mechanism for tumor cell survival. (4) PSs that photodamage the endoplasmic reticulum release heat shock proteins (HSPs), calcium, and calreticulin (CRT). (5) High levels of cytosolic calcium trigger apoptosis. HSP release and CRT displays on the cell surface are important damage-associated molecular patterns (DAMPs) that stimulate the antitumor immune system. (6) PSs that localize within endothelial cells in the tumor vasculature ablate blood vessels and induce tumor starvation.

influenced by nonspecific PS accumulation in the plasma membrane, resulting in immediate catastrophic damage and loss of membrane integrity (38). These necrotic, proinflammatory modes of cell death accelerate tumor growth and metastasis by recruiting tumor-associated macrophages, which differentiate into growth-/repair-promoting macrophages in the presence of cytokines such as interleukin 6 (IL-6), leukemia inhibitory factor (LIF), tumor necrosis factor (TNF), C-C motif chemokine 22 (CCL-22), and stromal cell-derived factor-12 (CXCL-12) (120, 121). However, certain forms of PDT recruit natural killer and $CD8^+$ cytotoxic T cells to generate an antitumor immune response. Expression of heat shock proteins HSP70 and HSP90, calreticulin, and high mobility group protein B1 (HMBG1) in the presence of ROS-induced damage in the ER stimulates an immunogenic cell death. Expression of these damage-associated molecular patterns (DAMPs) stimulates local inflammatory cells, a necessary mechanism to achieve optimal PDT (122). PDT-stimulated immune response has the acute effect of locally controlling tumor growth and is also preventative against metastasis and tumor recurrence by activating systemic immunosurveillance against tumor cells.

Activation of the innate immune system requires adequate blood flow to allow for a systemic antitumor response; thus, PSs designed to ablate tumor vasculature are not ideal. To circumvent this problem, an alternative method combines different intensities of light irradiation, coupling low- and high-fluence-rate light delivery. Fluence rate is the measurement of incident light on a cross-sectional area over a period of time. Initial low-fluence-rate light delivery can induce disperse PDT effects to implement a systemic antitumor immune response, and subsequent high fluence-rate light delivery can

destroy tumor vasculature and lead to acute tumor destruction. The PDT-activated immunogenic cell death response, also called photoimmunotherapy (PIT), was originally observed by the Kobayashi group (123): Light activation of antibody-bound IR700CW leads to a conformational change that irreparably damages the plasma membrane when bound to tumor cell membrane receptors. This damage leads to the release of DAMPs to initiate an immune response. Initially, PIT was found to be independent of ROS generation, instead relying on conformational changes to the antibody structure. However, ICG antibody conjugates also induce a similar effect via direct cellular ROS damage, which has allowed further insight into the molecular mechanisms of antitumor immune system stimulation and into rational design of PSs to induce this effect (124).

1.9 Targeting

1.9.1 Passive targeting

PDT has traditionally relied on the accumulation of PSs in the tumor site by passive targeting; a phenomenon in which the inherent pathophysiology of tumors allows increased accumulation of macromolecules. This has been exploited primarily in nanomedicine to reduce the side effects associated with many chemotherapeutics by reaching cytotoxic levels of drugs only at the tumor site. Nanoparticles passively accumulate in tumors due to the leaky and malformed vasculature of tumors coupled with poor lymphatic drainage, known as the enhanced permeability and retention (EPR) effect (125). The EPR effect leads to increased accumulation of larger macromolecules and nanoparticles in the tumor bed. Unfortunately, there has been poor clinical translation in human studies due to the heterogeneity of the EPR effect across different

types of cancers, individuals, and even tumors and metastases within the same patient (126).

1.9.2 Active targeting

Due to the limitations of passive targeting, tumor-specific moieties for active targeting by PSs of tumor tissue have been developed. Tumor-targeting agents include small molecules and antibodies. Small molecules are ideal targeting agents because they are generally inexpensive and do not inhibit cellular uptake of PSs, as sometimes observed with antibodies targeted to membrane proteins. Conversely, antibodies have a higher degree of tumor selectivity and sensitivity. Simple sugars similar to glucose are popular targeting moieties that have been used for years, most commonly for positron emission tomography scans. Cancer cells overexpress glucose transporter 1 (GLUT-1), which can be manipulated to increase the uptake of conjugated PSs (127, 128). Similar results have been seen with folate, hyaluronic acid, and transferrin (129, 130).

Antibody targeting has the highest degree of specificity for tumor cells (131). Unfortunately, many cancers that require additional therapeutic options do not express easily targetable receptors. Further, large antibodies lead to poor tumor penetration and extended vascular circulation. Antibodies can also induce an immune response and are expensive to synthesize. Smaller antibody fragments can lead to reduced circulation and improved tissue distribution (132). However, smaller antibody fragments require higher-affinity binding to prevent diffusion from the tumor bed and clearance through the vascular system (133).

PDT also has the means to enhance tumor drug uptake and can act as an indirect tumor-targeting technique. Under proper conditions, PDT induces necrotic cell death of tumor cells adjacent to blood vasculature. This perivascular destruction dilates the blood vessel, increasing blood volume but decreasing tumor blood pressure. The combination leads to increased nanoparticle perfusion into the tumor bed (134). This has been studied predominantly with NIR-PIT (near-IR-photoimmunotherapy) using various IR700-antibody conjugations; the PS undergoes ligand dissociation from the antibody's light chain when photoactivated, leading to membrane destruction. However, similar effects in traditional ROS-inducing PSs and upconverting nanoparticles have been seen (135). Histopathology following NIR-PIT shows dilated tumor vasculature with a widened tumor interstitium, which has been confirmed by magnetic resonance imaging and fluorescent visualization of nanoagent accumulation in the tumor bed. This large increase in tumor permeability is known as the super-enhanced permeability and retention (SUPR) effect and has been used to increase tumor accumulation of nanodrug delivery 24-fold (123). The SUPR effect leads to increased targeted uptake of nanomaterials, which offers promising optical properties as well as an ideal platform for multidrug delivery, tumor targeting, and improved biostability.

1.10 Light Dosing Regimens

Fiber optics, light-emitting diodes, and microendoscopic delivery have advanced light delivery to the tumor environment. Clinical trials using interstitial, endoscopic, laparoscopic, and intraoperative light delivery following surgical resection have been performed. However, the inherent heterogeneity of tumors makes standardized regimens of light treatment and drug delivery challenging. Different PSs localize

differently within tumors, and tumors have highly varied microenvironments and drug uptake, making it difficult to anticipate the proper light dosimetry to induce a particular effect (136). Higher fluence rates (75 mW/cm^2) rapidly deplete intratumoral oxygen pressure (pO_2) and do not significantly decrease tumor growth as expected (137). Surprisingly, lower fluence rates are more effective for tumor control (137, 138). The rapid generation of ROS with high fluence rates can deplete the tumor oxygen too quickly, creating hypoxic conditions that inhibit PDT and promote tumor cell survival. Premature vascular collapse also inhibits local tumor phototoxicity, blocking the delivery of additional O_2 and PSs. Studies have found that an initial low-fluence-rate light delivery, followed by high-fluence-rate light delivery, improves the efficacy of PDT using the clinically approved PS agent temoporfin (139). Administering two independent light treatments with differing dosimetries improves antitumor efficacy in several models and across multiple PSs (140). Monitoring tumor oxygen levels during PDT may enable real-time adjustments to light distribution and intensity, as different PSs can consume oxygen at different rates (141, 142). Timing of light treatment is complicated by PS pharmacokinetics, which varies dramatically between PSs, and an optimal light treatment window can vary from hours to days after PS delivery. A major limitation to PDT is recurrence, which is thought to occur due to incomplete tumor response to therapy. Optimizing light treatment regimens based on the mode of action of a specific PS would reduce recurrence and improve outcomes.

1.11 Resistance Mechanisms

Autophagy, the degradation and recycling of cellular components, promotes cell survival under harsh conditions and is often upregulated in cancer cells that are

resistant to traditional radiotherapies and chemotherapies. Increased expression of autophagy markers in cancer stem cells and malignant precursor cells has been reported (143, 144). Autophagy can decrease the efficacy of mitochondria-targeted PDT, and incomplete tumor response following PDT increases expression of autophagy proteins in tumor cells (145, 146). To address this, researchers have used combinatorial therapy with autophagy-inhibiting agents to sensitize cells to PDT (147). PDT in combination with lysosome- and mitochondria-targeting PSs should also be considered to avoid autophagy induced resistance; lysosomal destruction halts the recycling of biomolecules that promote cancer cell survival via autophagy mechanisms. For example, the combination of two PSs, phenylbenzothiazole (EtNBS) and verteporfin, showed a 95% reduction in the weights of fibrosarcomas in BALB/c mice (148). This level of advanced photokilling could not be replicated with dramatically higher doses of either PS administered alone or with higher doses of light treatment. These two agents localize to different organelles within the cell: EtNBS localizes to the lysosomes, inhibiting apoptosis and releasing labile iron and Ca^{+2}; verteporfin localizes primarily to mitochondria and the ER to induce apoptosis. Although more preclinical data are needed, combining PDT with autophagy or lysosome inhibitors could increase efficacy for large tumor debulking or complete tumor response. Understanding the distinct mode of action of specific PSs is important for developing combinatorial treatments that inhibit cell survival programs induced by PDT.

The destructive effect of PDT relies primarily on the production of ROS, which causes irreversible oxidative damage to membranes and organelles. Unfortunately, cancer cells tend to have highly dynamic stress resistance mechanisms, including high

levels of superoxide dismutases (SODs), glutathione peroxidase, and thioredoxins (149). This promotes a highly oxidative environment, promoting genetic instability and increased resistance to cell death mechanisms. Following PDT, MDA-MB-231 breast cancer cell xenografts show an immediate increase in inducible nitric oxide synthase (iNOS) and nitric oxide, which leads to increased tumor growth and inhibition of ROS-induced apoptosis (150). Administration of NOS inhibitors improves PDT efficacy with Photofrin, likely by hindering the cytoprotective effects of iNOS (151, 152), though these benefits are observed only with high-fluence-rate PDT (153).

Resistance to apoptosis is a hallmark of cancer and has been well reported for PDT (145, 154). Overexpression of antiapoptotic *Bcl-2* and underexpression of proapoptotic *Bid* and *Bax* inhibit cell death programs to improve cell survival during PDT (155). Low-power PDT leads to increases in the survival and stress responses, as upregulation is seen in hypoxia inducible factor 1 (HIF-1) - and nuclear factor–κB (NF-κB)-induced genes (156). Because failure of PDT to fully eradicate tumors can lead to increased malignancy and tumor progression, treatment regimens must be appropriately designed to avoid inadvertently triggering protumor cell programs.

Increased expression of drug efflux pumps is a well-established mode of drug resistance. This remains true for PDT, though the efflux pumps expressed tend to correlate to the localization and mode of uptake of the PS. ATP-binding cassette super-family G member 2 (ABCG2) is an efflux pump commonly expressed in multidrug-resistant cancers, and several PSs are known substrates (157). Increased expression is seen after low-dose PDT, and upregulation in cell lines reduces the efficiency of PDT (155). Inhibition of efflux pumps has been successful in antibacterial PDT: Treatment

with methylene blue PDT is improved when it is combined with a microbial efflux pump inhibitor (158). Additionally, cell lines resistant to mitochondrial PDT show changes to mitochondrial structure and metabolism, though more research is needed to determine the exact molecular mechanisms (159, 160). Overall, this is an area where more research is needed in order to interpret potential resistances associated with therapy and improved indicators for cancers where PDT could be an ideal therapeutic option.

1.12 Combinatorial Therapy

Increased knowledge about the biochemical interactions driving tumor progression has led to combinatorial treatment, by which multiple pathways are targeted to improve response to therapy and mitigate drug resistance (161). PDT already has the benefit of targeting multiple cell death pathways by inducing direct damage to mitochondria, Golgi apparatus, ER, and lysosomes, creating widespread irreversible cell damage at proper dosages. As discussed above, combining PDT with autophagy or lysosome inhibitors may be effective against tumors with high levels of autophagy. The combinatorial therapies discussed below focus on targeting additional pathways to enhance PDT and subvert tumor survival responses.

1.12.1 Impairment of Cellular Redox

Many combinatorial treatments enhance the primary mechanism of PDT—generation of ROS. PDT can be augmented by increasing tumor oxygen saturation, interfering with cellular redox balance, or potentiating the effects of PDT-generated ROS. Antioxidant inhibitors have had poor effects independently but show promise for enhancing the effects of PDT (162, 163). Dysfunction to redox homeostasis via cellular

antioxidant inhibitors such as diethyldithiocarbamate (a Cu/Zn-SOD inhibitor), 2-methoxyestradiol (a Mn-SOD inhibitor), l-buthionine sulfoximine (a glutathione synthesis inhibitor), and 3-amino-1,2,4-triazole (a catalase inhibitor) has displayed increased cell death and ROS generation with traditional PDT agents in cell models but requires further study in animal models (163). Exogenous small-molecule antioxidants such as vitamins E (tocopherol) and C (ascorbate) have shown promise both as protective agents in normal cells and as selectively toxic agents against cancer cells at higher pro-oxidant concentrations (164). However, reaching clinically effective dosages of these agents has proved to be difficult, which has limited their use and study. Hollow MnO_2 nanoparticles have become a promising nanoplatform for PDT, as they provide delivery of PSs, which tend to be poorly soluble, and also stimulate oxygen levels. MnO_2 catalyzes the breakdown of H_2O_2 into water and oxygen, maintaining stable levels of oxygen for a prolonged PDT response (165, 166). MnO_2 nanosheets have also been implemented with PDT to oxidize intracellular glutathione, which impairs the antioxidant response to ROS generation (167). There have been many studies of the antineoplastic effects of cannabidiol, which increase ROS generation in mitochondria and ER of cancer cells (168). Although not efficacious on its own, cannabidiol showed dramatically increased potency when combined with PDT and radiotherapy (169). For ALA prodrugs, agents that alter heme and iron metabolism have led to increased accumulation of PpIX and subsequent improvements to PDT in preclinical models (170–172).

1.12.2 Ferroptosis

Ferroptosis is another form of regulated cell death that ties in closely with oxidative stress and cancer. This unique form of cell death is based on iron-dependent

lipid peroxidation. Cellular iron homeostasis is highly regulated due to the high reactivity of labile iron with oxygen to form ROS (173). Ferroptosis can be induced by perturbations to the glutathione antioxidant network and metabolism, inhibition of glutathione peroxidase 4 (GPX4), and increasing levels of intracellular iron. For example, although pancreatic cancer is highly resistant to cellular apoptotic mechanisms, ferroptosis can subvert typical apoptotic cell signaling to induce cell death in pancreatic ductal adenocarcinoma cell lines (174, 175). Iron chelators such as deferoxamine combined with prodrug ALA treatment have been investigated, as the sequestration of iron inhibits the final step of heme synthesis, increasing the generation of photoactive PpIX from ALA (176, 177). Conversely, iron chelation can also inhibit ferroptosis; iron complexed with deferoxamine lacks redox potency, reducing the efficacy of PDT-induced cell death (178). Potential PDT combinatorial methods could involve dual delivery of small-molecule ferroptosis inducers (e.g., erastin, sorafenib, and RSL3), iron doping via nanoparticle delivery, and iron-based nanoparticles. Not only has ferroptosis been shown to resensitize cancer cells to chemotherapy and promote PDT, but high levels of ROS combined with labile iron could produce O_2 via Fenton reactions. This would resupply the hypoxic tumor microenvironment with molecular oxygen, solving a key problem inherent to PDT. Finally, many ferroptosis inducers act by inhibiting the cellular redox balance, a mechanism that would also enhance PDT.

1.12.3 Tumor Sensitization

PDT has been shown to improve the outcome of traditional chemotherapy and radiotherapy. Although PDT itself primarily has a localized effect, resulting in minimal side effects, it can also heighten the effect of radiotherapies and chemotherapies.

Sensitization of the tumor to traditional therapies allows for lower effective doses, reducing side effects while improving therapeutic outcomes. This has been especially notable with platinum-based chemotherapeutics because of their induced expression of proapoptotic pathway proteins (179). In xenograft models of small-cell lung cancer, low-dose cisplatin combined with PDT displayed a synergistic effect on tumor size when compared with either treatment alone (180). However, reports regarding cisplatin in preclinical models have been contradictory; due to the reliance of PDT efficacy on the immune system, nude mouse models may not be appropriate for this type of therapy (181). PDT combined with radiotherapy led to similar results, although the interaction between the two treatments has proved difficult to study. The combination of verteporfin and radiation therapy showed a 60% reduction in tumor doubling time in patients with fibrosarcoma (182). Reduced side effects are common with this type of combinatorial therapy, but the mechanism for the unexpectedly low cross-interaction toxicity has yet to be determined (183).

1.12.4 Immunostimulators

Immune activation is a crucial part of the PDT mechanism. An increased immune response has been reported to promote PDT efficacy in human patients, provoking interest in enhancing this effect (184). Immune checkpoint therapy in T cells enhances antitumor therapy by preventing tumor proteins from inhibiting the activation response of T effector cells (185). Treatment of bilateral cancer in cholinergic mouse models with a pyrolipid PS and PD-1/PD-L1 (programmed cell death protein 1/programmed cell death ligand 1) axis inhibitor (oxaliplatin) improved regression of the primary-site, light-treated tumor as well as that of distant tumors. This abscopal effect was attributed to antitumor

immunity, evidenced by increased exposure to calreticulin by treated tumor cells followed by increased presence of $CD8^+$ and $CD4^+$ T cells at distant tumor sites (186). Similar synergistic effects have been observed with immunostimulators, such as glycated chitosan, CpG oligodeoxynucleotides, and cyclophosphamide, as well as other immune checkpoint inhibitors (187, 188).

1.13 Conclusions and Future Outlook

In this review, we have highlighted the scientific advances in photoactive theranostics that are expanding clinical PDT and photodynamic diagnostic applications. These advances have the potential to revolutionize modern treatments of cancer and other diseases. Breakthroughs in materials science, electronics, and imaging equipment have enabled exploration into NIR fluorophores/phosphors and have expanded the clinical applicability of PDT. This expansion has facilitated novel investigations into photosensitizing agents in order to meet the demand for optimized, accessible cancer treatments. We have summarized several innovative and promising preclinical works. Moving these multimodal PSs into clinical settings should be prioritized. However, several areas still need to be advanced in order to fully realize the tremendous potential of photoactive theranostics. The wide variety of PSs studied with different tumor and cellular models has made it difficult to develop optimized regimens for ideal patient outcomes. Further research into each potential theranostic agent is needed to determine proper dosing criteria, both for the photoactive agent and for the activating light. Improved PS agents need to be designed with minimal off-target effects, greater selectivity, enhanced phototoxicity, and enhanced penetrance. Additional standards, generally neglected in the literature, are required to establish proper dosing intervals for

different combinatorial therapies with PDT. Whether PDT is being used as a sensitizing agent, an immune activator, or the primary treatment, it will have different dosing windows depending on the combined therapy. Substandard clinical trial results may be due to variable pharmacokinetics, which is important for determining the timing of light treatment. Furthermore, PDT is an ideal complement for combinatorial therapies with great potential for enhancing tumor-killing efficacy beyond that of either approach alone and for enabling greater space for treatment development and exploration. Many of the chemotherapeutic agents discussed are well tolerated at low concentrations, and the combination of tumor targeting and broad effects of PDT promises a potent antitumor effect. Future work should aim to improve the efficacy of PDT through rationally designed treatment strategies, to explore novel photoactive materials, and to continue to expand applications in a broader range of cancer types.

1.14 Acknowledgments

The authors thank Matthew Bates, Elliot Ensink, and Shao Thing Teoh for helpful discussions and a critical reading of the manuscript. For image elements used in the figures, we acknowledge somersault18:24 (http://www.somersault1824.com/) (CC BY-NC-SA 4.0).

1.15 Dissertation Goals

Light-activated theranostics offer promising potential to enhance both early diagnostics and cancer therapy. Advances in optical technologies have allowed strides to be made in imaging techniques and light irradiation, but current photoactive agents have not met the necessary requirements to improve early cancer therapy and

diagnostics. At present, they are plagued by poor optical properties and undesirable toxicity in healthy tissue, which limits effective dosage and leads to poor clinical outcomes.

To address this need, I have adopted a counterion pairing platform originally developed for engineering solar cells. A photoactive cationic cyanine (Cy^+) is paired with a coordinating anion, which has been shown with ultraviolet photoelectron spectroscopy to shift the frontier molecular orbital levels (which dictate electronic properties), without changing the bandgap (which dictates optical properties). The counterion pairing approach allows independent optimization of optical parameters through a photoactive cation, which can then be adjusted with an anion to shift valence energy levels. This exciting new engineering paradigm has been capitalized on in photovoltaics, however, its biomedical application has yet to be determined. My guiding hypothesis is that *in vivo* toxicity of fluorescent organic salts can be modulated by counterion pairing to control the generation of resonant reactive oxygen species in biological environments. The primary goals of this dissertation are to 1) elucidate the effect of adjusting frontier molecular orbital energy levels of organic salts in the context of cellular environments and 2) ascertain the physiological relevance of counterion tuning in a translational cancer model.

To study this, I first characterized the chemical and photophysical properties of organic salts in solution. Small angle X-ray scattering revealed that in aqueous solution organic salts self-organize into 5-9 nm organic salts nanoparticles, capturing the composition of the photoactive cation and electronic modulating anion. Redox potential and zeta potential measurements confirm the electronic shifts observed in the physical

state are retained with organic salt nanoparticle formation. Upon confirmation that photophysical characteristics of organic salts are maintained in solution, cell viability screenings were done in human lung carcinoma (A549) and melanoma (WM1158) cell lines. Counterion pairing with standard small hard anions yields cytotoxic organic salts (toxic in the dark), while counterion pairing with soft weakly coordinating anions yields phototoxic (toxic with light) and nontoxic organic salts. Cellular ROS measurements demonstrate that counterion pairing leads to different levels of photoinduced mitochondrial ROS generation. These findings were further validated using mass spectrometry to quantitate cellular uptake of organic salts and toxicity assays, which demonstrated that phototoxicity trends are inversely correlated to uptake, and that anions are not independently toxic. The measured zeta potential of nanoparticles in aqueous solution correlates with phototoxicity trends, validating this energy modulation platform and its potential for generation of optimized organic salts as non-toxic for therapy or phototoxic for PDT.

I expanded on these promising *in vitro* findings by shifting to a clinically relevant mouse model of metastatic breast cancer. While initial studies were done in human cancer cell lines, the effect of the immune system on cancer is integral, especially when assessing therapeutic efficacy. Therefore, I utilized an orthotopic MMTV-Myc driven mammary cancer model to assess *in vivo* photodynamic therapy and off-site toxicity. Findings confirm *in vitro* results, utilizing our previously established counterion tuning strategy I developed a selectively phototoxic PS capable of deep tissue photoactivation and imaging. Counterion tuning enhances phototoxicity upon NIR irradiation to induce a robust antitumor response with minimal toxicity observed in normal tissue. Traditional

organic salts that do not maintain counterion contact in cellular milieu are nonspecifically cytotoxic, with an inadequate therapeutic margin for light induced phototoxic effects without nonspecific dark cytotoxicity.

My work validates the potential for counterion tuning to engineer optimized fluorescent agents for clinical cancer therapy. I have additionally contributed to the phototherapy field by demonstrating and characterizing potent PDT in a preclinical model. My findings within this work have translational potential and could revolutionize photoactive agent design.

REFERENCES

REFERENCES

1. Huang H, Song W, Rieffel J, Lovell JF. 2015. Emerging applications of porphyrins in photomedicine. *Front. Phys.* 3:

2. Cheng L, Wang C, Feng L, Yang K, Liu Z. 2014. Functional Nanomaterials for Phototherapies of Cancer. *Chem. Rev.* 114(21):10869–939

3. Li Y, Lin T, Luo Y, Liu Q, Xiao W, et al. 2014. A smart and versatile theranostic nanomedicine platform based on nanoporphyrin. *Nat Commun*. 5(1):4712

4. Patel SK, Janjic JM. 2015. Macrophage Targeted Theranostics as Personalized Nanomedicine Strategies for Inflammatory Diseases. *Theranostics*. 5(2):150–72

5. Pushpan S, Venkatraman S, Anand V, Sankar J, Parmeswaran D, et al. 2002. Porphyrins in Photodynamic Therapy - A Search for Ideal Photosensitizers. *CMCACA*. 2(2):187–207

6. Oniszczuk A, Wojtunik-Kulesza KA, Oniszczuk T, Kasprzak K. 2016. The potential of photodynamic therapy (PDT)—Experimental investigations and clinical use. *Biomedicine & Pharmacotherapy*. 83:912–29

7. Hönigsmann H. 2013. History of phototherapy in dermatology. *Photochem. Photobiol. Sci.* 12(1):16–21

8. Calixto G, Bernegossi J, de Freitas L, Fontana C, Chorilli M. 2016. Nanotechnology-Based Drug Delivery Systems for Photodynamic Therapy of Cancer: A Review. *Molecules*. 21(3):342

9. Liu Y, Bhattarai P, Dai Z, Chen X. 2019. Photothermal therapy and photoacoustic imaging *via* nanotheranostics in fighting cancer. *Chem. Soc. Rev.* 48(7):2053–2108

10. Foote CS. 1991. DEFINITION OF TYPE I and TYPE II PHOTOSENSITIZED OXIDATION. *Photochem Photobiol*. 54(5):659–659

11. Lan G, Ni K, Lin W. 2019. Nanoscale metal–organic frameworks for phototherapy of cancer. *Coordination Chemistry Reviews*. 379:65–81

12. Celli JP, Spring BQ, Rizvi I, Evans CL, Samkoe KS, et al. 2010. Imaging and Photodynamic Therapy: Mechanisms, Monitoring, and Optimization. *Chem. Rev.* 110(5):2795–2838

13. Morton CA, Szeimies R -M., Basset-Séguin N, Calzavara-Pinton PG, Gilaberte Y, et al. 2020. European Dermatology Forum guidelines on topical photodynamic therapy

2019 Part 2: emerging indications – field cancerization, photorejuvenation and inflammatory/infective dermatoses. *J Eur Acad Dermatol Venereol*. 34(1):17–29

14. Raab O. 1900. On the effect of fluorescent substances on infusoria. *Z Biol*. 39:524–26

15. Macmillan JD, Maxwell WA, Chichester CO. 1966. Lethal Photosensitization of Microorganisms with Light from a continuous-wave gas laser. *Photochemistry and Photobiology*. 5(7):555–65

16. Taub AF. 2007. Photodynamic Therapy: Other Uses. *Dermatologic Clinics*. 25(1):101–9

17. Hamblin MR, Hasan T. 2004. Photodynamic therapy: a new antimicrobial approach to infectious disease? *Photochem. Photobiol. Sci.* 3(5):436

18. Araújo NC, Fontana CR, Bagnato VS, Gerbi MEM. 2014. Photodynamic antimicrobial therapy of curcumin in biofilms and carious dentine. *Lasers Med Sci*. 29(2):629–35

19. Hu Z, Liu L, Zhang W, Liu H, Li J, et al. 2018. Dynamics of HPV viral loads reflect the treatment effect of photodynamic therapy in genital warts. *Photodiagnosis and Photodynamic Therapy*. 21:86–90

20. Wainwright M. 2004. Photoinactivation of viruses. *Photochem. Photobiol. Sci.* 3(5):406

21. van Straten D, Mashayekhi V, de Bruijn HS, Oliveira S, Robinson DJ. 2017. Oncologic Photodynamic Therapy: Basic Principles, Current Clinical Status and Future Directions. *Cancers (Basel)*. 9(2):

22. Mimura S, Ito Y, Nagayo T, Ichii M, Kato H, et al. 1996. Cooperative clinical trial of photodynamic therapy with photofrin II and excimer dye laser for early gastric cancer. *Lasers in Surgery and Medicine*. 19(2):168–72

23. Golusiński P, Szybiak B, Wegner A, Pazdrowski J, Pieńkowski P. 2015. Photodynamic therapy in palliative treatment of head and neck cancer. *Otolaryngol Pol*. 69(3):15–20

24. Hamblin MR. 2020. Photodynamic therapy for cancer: what's past is prologue. *Photochem Photobiol*. 96(3):506–16

25. Isakoff SJ, Rogers GS, Hill S, McMullan P, Habin KR, et al. 2017. An open label, phase II trial of continuous low-irradiance photodynamic therapy (CLIPT) using verteporfin for the treatment of cutaneous breast cancer metastases. *JCO*. 35(15_suppl):TPS1121–TPS1121

26. Mery E, Golzio M, Guillermet S, Lanore D, Le Naour A, et al. 2017. Fluorescence-guided surgery for cancer patients: a proof of concept study on human xenografts in mice and spontaneous tumors in pets. *Oncotarget*. 8(65):109559–74

27. Jewell EL, Huang JJ, Abu-Rustum NR, Gardner GJ, Brown CL, et al. 2014. Detection of sentinel lymph nodes in minimally invasive surgery using indocyanine green and near-infrared fluorescence imaging for uterine and cervical malignancies. *Gynecologic Oncology*. 133:274–77

28. Cho SS, Salinas R, Lee JYK. 2019. Indocyanine-Green for Fluorescence-Guided Surgery of Brain Tumors: Evidence, Techniques, and Practical Experience. *Front Surg*. 6:11

29. Kim SH, Rho SY, Kang and CM. 2018. Indocyanine Green-Fluorescent Pancreatic Perfusion-Guided Resection of Distal Pancreas in Solid Pseudopapillary Neoplasm: Usefulness and Feasibility During Pancreaticobiliary Surgery. *Journal of Minimally Invasive Surgery*. 21(1):43–45

30. Zhang C, Zhao Y, Zhang H, Chen X, Zhao N, et al. 2017. The Application of Heptamethine Cyanine Dye DZ-1 and Indocyanine Green for Imaging and Targeting in Xenograft Models of Hepatocellular Carcinoma. *International Journal of Molecular Sciences*. 18(6):1332

31. Stummer W, Pichlmeier U, Meinel T, Wiestler OD, Zanella F, et al. 2006. Fluorescence-guided surgery with 5-aminolevulinic acid for resection of malignant glioma: a randomised controlled multicentre phase III trial. *Lancet Oncol.* 7(5):392–401

32. Hadjipanayis CG, Stummer W. 2019. 5-ALA and FDA approval for glioma surgery. *J. Neurooncol.* 141(3):479–86

33. Lwin TM, Murakami T, Miyake K, Yazaki PJ, Shivley JE, et al. 2018. Tumor-Specific Labeling of Pancreatic Cancer Using a Humanized Anti-CEA Antibody Conjugated to a Near-Infrared Fluorophore. *Ann. Surg. Oncol.* 25(4):1079–85

34. Tummers WS, Miller SE, Teraphongphom NT, Gomez A, Steinberg I, et al. 2018. Intraoperative Pancreatic Cancer Detection using Tumor-Specific Multimodality Molecular Imaging. *Ann Surg Oncol*. 25(7):1880–88

35. Arsen'ev AI, Kanaev SV, Barchuk AS, Vedenin IO, Klitenko VN, et al. 2007. [Use of endotracheobronchial surgery in conjunction with radiochemotherapy for advanced non-small lung cancer]. *Vopr Onkol*. 53(4):461–67

36. CB II S, Ka C. 2014. Photodynamic therapy for lung cancer and malignant pleural mesothelioma. *Semin Oncol*. 41(6):820–30

37. Higa JT, Hwang JH. 2016. Chapter 10 - History of Ablative Therapies for Barrett's and Superficial Adenocarcinoma. In *Barrett's Esophagus*, ed DK Pleskow, T Erim, pp. 133–49. Boston: Academic Press

38. Hsieh Y-J, Wu C-C, Chang C-J, Yu J-S. 2003. Subcellular localization of Photofrin determines the death phenotype of human epidermoid carcinoma A431 cells triggered by photodynamic therapy: when plasma membranes are the main targets. *J. Cell. Physiol.* 194(3):363–75

39. Dougherty TJ, Cooper MT, Mang TS. 1990. Cutaneous phototoxic occurrences in patients receiving Photofrin®. *Lasers in Surgery and Medicine*. 10:485–88

40. Sachar M, Anderson KE, Ma X. 2016. Protoporphyrin IX: the Good, the Bad, and the Ugly. *J Pharmacol Exp Ther*. 356(2):267–75

41. Fukuda H, Paredes S, Batlle AM. 1989. Tumor-localizing properties of porphyrins. In vitro studies using the porphyrin precursor, aminolevulinic acid, in free and liposome encapsulated forms. *Drug Des. Deliv.* 5(2):133–39

42. Chen R, Huang Z, Chen G, Li Y, Chen X, et al. 2008. Kinetics and subcellular localization of 5-ALA-induced PpIX in DHL cells via two-photon excitation fluorescence microscopy. *Int. J. Oncol.* 32(4):861–67

43. de Oliveira ER, Inada NM, Blanco KC, Bagnato VS, Salvio AG. 2019. Cancerization Field Treatment using Topical Photodynamic Therapy: a comparison between two Aminolevulinate Derivatives. *Photodiagnosis Photodyn Ther*, p. 101603

44. Berger AP, Steiner H, Stenzl A, Akkad T, Bartsch G, Holtl L. 2003. Photodynamic therapy with intravesical instillation of 5-aminolevulinic acid for patients with recurrent superficial bladder cancer: a single-center study. *Urology*. 61(2):338–41

45. Inoue K. 2017. 5-Aminolevulinic acid-mediated photodynamic therapy for bladder cancer. *International Journal of Urology*. 24(2):97–101

46. Warren CB, Karai LJ, Vidimos A, Maytin EV. 2009. Pain Associated with Aminolevulinic Acid-Photodynamic Therapy of Skin Disease. *J Am Acad Dermatol*. 61(6):1033–43

47. Kang M-H, Jeong GS, Smoot DT, Ashktorab H, Hwang CM, et al. 2017. Verteporfin inhibits gastric cancer cell growth by suppressing adhesion molecule FAT1. *Oncotarget*. 8(58):98887–97

48. Aquaron R, Forzano O, Murati JL, Fayet G, Aquaron C, Ridings B. 2002. Simple, reliable and fast spectrofluorometric method for determination of plasma Verteporfin (Visudyne) levels during photodynamic therapy for choroidal neovascularization. *Cell. Mol. Biol. (Noisy-le-grand)*. 48(8):925–30

49. Scott LJ, Goa KL. 2000. Verteporfin. *Drugs & Aging*. 16(2):139–46

50. Gibault F, Corvaisier M, Bailly F, Huet G, Melnyk P, Cotelle P. 2016. Non-Photoinduced Biological Properties of Verteporfin. *Curr Med Chem*. 23(11):1171–84

51. Lui JW, Xiao S, Ogomori K, Hammarstedt JE, Little EC, Lang D. 2019. The Efficiency of Verteporfin as a Therapeutic Option in Pre-Clinical Models of Melanoma. *J Cancer*. 10(1):1–10

52. Wei H, Wang F, Wang Y, Li T, Xiu P, et al. 2017. Verteporfin suppresses cell survival, angiogenesis and vasculogenic mimicry of pancreatic ductal adenocarcinoma via disrupting the YAP-TEAD complex. *Cancer Sci*. 108(3):478–87

53. Mazor O, Brandis A, Plaks V, Neumark E, Rosenbach-Belkin V, et al. 2005. WST11, a novel water-soluble bacteriochlorophyll derivative; cellular uptake, pharmacokinetics, biodistribution and vascular-targeted photodynamic activity using melanoma tumors as a model. *Photochem. Photobiol.* 81(2):342–51

54. Azzouzi A-R, Vincendeau S, Barret E, Cicco A, Kleinclauss F, et al. 2017. Padeliporfin vascular-targeted photodynamic therapy versus active surveillance in men with low-risk prostate cancer (CLIN1001 PCM301): an open-label, phase 3, randomised controlled trial. *The Lancet Oncology*. 18(2):181–91

55. Michael-Titus AT, Whelpton R, Yaqub Z. 1995. Binding of temoporfin to the lipoprotein fractions of human serum. *Br J Clin Pharmacol*. 40(6):594–97

56. Teiten M-H, Marchal S, D'Hallewin MA, Guillemin F, Bezdetnaya L. 2003. Primary photodamage sites and mitochondrial events after Foscan photosensitization of MCF-7 human breast cancer cells. *Photochem. Photobiol.* 78(1):9–14

57. D'Cruz AK, Robinson MH, Biel MA. 2004. mTHPC-mediated photodynamic therapy in patients with advanced, incurable head and neck cancer: a multicenter study of 128 patients. *Head Neck*. 26(3):232–40

58. Senge MO, Brandt JC. 2011. Temoporfin (Foscan®, 5,10,15,20-Tetra(m-hydroxyphenyl)chlorin)—A Second-generation Photosensitizer†,‡. *Photochemistry and Photobiology*. 87(6):1240–96

59. Tsukagoshi S, Tokyo Cooperative Oncology Group. 2004. [Development of a novel photosensitizer, talaporfin sodium, for the photodynamic therapy (PDT)]. *Gan To Kagaku Ryoho*. 31(6):979–85

60. Kanda T, Sugihara T, Takata T, Mae Y, Kinoshita H, et al. 2019. Low-density lipoprotein receptor expression is involved in the beneficial effect of photodynamic therapy using talaporfin sodium on gastric cancer cells. *Oncology Letters*. 17(3):3261–66

61. Miki Y, Akimoto J, Yokoyama S, Homma T, Tsutsumi M, et al. 2013. Photodynamic therapy in combination with talaporfin sodium induces mitochondrial apoptotic cell death accompanied with necrosis in glioma cells. *Biol. Pharm. Bull.* 36(2):215–21

62. Ohashi S, Kikuchi O, Tsurumaki M, Nakai Y, Kasai H, et al. 2014. Preclinical Validation of Talaporfin Sodium-Mediated Photodynamic Therapy for Esophageal Squamous Cell Carcinoma. *PLOS ONE*. 9(8):e103126

63. Oliveira J, Monteiro E, Santos J, Silva JD, Almeida L, Santos LL. 2017. A first in human study using photodynamic therapy with Redaporfin in advanced head and neck cancer. *JCO*. 35(15_suppl):e14056–e14056

64. Nava HR, Allamaneni SS, Dougherty TJ, Cooper MT, Tan W, et al. 2011. Photodynamic therapy (PDT) using HPPH for the treatment of precancerous lesions associated with Barrett's esophagus. *Lasers Surg Med*. 43(7):705–12

65. Rigual NR, Shafirstein G, Frustino J, Seshadri M, Cooper M, et al. 2013. Adjuvant Intraoperative Photodynamic Therapy in Head and Neck Cancer. *JAMA Otolaryngol Head Neck Surg*. 139(7):706–11

66. Jones HJ, Vernon DI, Brown SB. 2003. Photodynamic therapy effect of m-THPC (Foscan®) in vivo: correlation with pharmacokinetics. *Br J Cancer*. 89(2):398–404

67. Li B, Lin L, Lin H, Wilson BC. 2016. Photosensitized singlet oxygen generation and detection: Recent advances and future perspectives in cancer photodynamic therapy. *J. Biophoton*. 9(11–12):1314–25

68. Kosaka N, Ogawa M, Choyke PL, Kobayashi H. 2009. Clinical implications of near-infrared fluorescence imaging in cancer. *Future Oncol*. 5(9):1501–11

69. Cao J, Zhu B, Zheng K, He S, Meng L, et al. 2020. Recent Progress in NIR-II Contrast Agent for Biological Imaging. *Front Bioeng Biotechnol*. 7:

70. Haque A, Faizi MSH, Rather JA, Khan MS. 2017. Next generation NIR fluorophores for tumor imaging and fluorescence-guided surgery: A review. *Bioorg. Med. Chem.* 25(7):2017–34

71. Hong G, Antaris AL, Dai H. 2017. Near-infrared fluorophores for biomedical imaging. *Nat Biomed Eng*. 1(1):1–22

72. Wang H, Li X, Tse BW-C, Yang H, Thorling CA, et al. 2018. Indocyanine green-incorporating nanoparticles for cancer theranostics. *Theranostics*. 8(5):1227–42

73. Usama SM, Thavornpradit S, Burgess K. 2018. Optimized Heptamethine Cyanines for Photodynamic Therapy. *ACS Appl. Bio Mater.* 1(4):1195–1205

74. Kilin V. 2014. Counterion-enhanced cyanine dye loading into lipid nano-droplets for single-particle tracking in zebrafish. *Biomaterials*. 35:7

75. Shulov I. 2016. Non-coordinating anions assemble cyanine amphiphiles into ultra-small fluorescent nanoparticles. *Chem. Commun.*, p. 4

76. Reisch A. 2014. Collective fluoresecense switching of counter-ion assumbled dyes in polymer nanoparticles. *Nature Communications*

77. Shulov I. 2015. Fluorinated counterion-enhanced emission of rhodamine aggregates: ultrabright nanoparticles for bioimaging and light-harvesting. *Nanoscale*

78. Magut PKS, Das S, Fernand VE, Losso J, McDonough K, et al. 2013. Tunable Cytotoxicity of Rhodamine 6G via Anion Variations. *J. Am. Chem. Soc.* 135(42):15873–79

79. Siraj N, Kolic PE, Regmi BP, Warner IM. 2015. Strategy for Tuning the Photophysical Properties of Photosensitizers for Use in Photodynamic Therapy. *Chem. Eur. J.* 21(41):14440–46

80. Broadwater D, Bates M, Jayaram M, Young M, He J, et al. 2019. Modulating cellular cytotoxicity and phototoxicity of fluorescent organic salts through counterion pairing. *Scientific Reports*. 9(1):15288

81. Zhang C, Zhao Y, Zhao N, Tan D, Zhang H, et al. 2018. NIRF Optical/PET Dual-Modal Imaging of Hepatocellular Carcinoma Using Heptamethine Carbocyanine Dye. *Contrast Media Mol Imaging*. 2018:4979746

82. Randall LM, Wenham RM, Low PS, Dowdy SC, Tanyi JL. 2019. A phase II, multicenter, open-label trial of OTL38 injection for the intra-operative imaging of folate receptor-alpha positive ovarian cancer. *Gynecol. Oncol.* 155(1):63–68

83. Lamberts LE, Koch M, de Jong JS, Adams ALL, Glatz J, et al. 2017. Tumor-Specific Uptake of Fluorescent Bevacizumab-IRDye800CW Microdosing in Patients with Primary Breast Cancer: A Phase I Feasibility Study. *Clin. Cancer Res.* 23(11):2730–41

84. Li D, Qu C, Liu Q, Wu Y, Hu X, et al. 2020. Monitoring the Real-Time Circulatory System-Related Physiological and Pathological Processes In Vivo Using a Multifunctional NIR-II Probe. *Advanced Functional Materials*. 30(6):1906343

85. Antaris AL, Chen H, Cheng K, Sun Y, Hong G, et al. 2016. A small-molecule dye for NIR-II imaging. *Nature Materials*. 15(2):235–42

86. Wang S, Fan Y, Li D, Sun C, Lei Z, et al. 2019. Anti-quenching NIR-II molecular fluorophores for in vivo high-contrast imaging and pH sensing. *Nat Commun*. 10(1):1–11

87. Zhu S, Yung BC, Chandra S, Niu G, Antaris AL, Chen X. 2018. Near-Infrared-II (NIR-II) Bioimaging via Off-Peak NIR-I Fluorescence Emission. *Theranostics*. 8(15):4141–51

88. Staggers N, McCasky T, Brazelton N, Kennedy R. 2008. Nanotechnology: The coming revolution and its implications for consumers, clinicians, and informatics. *Nursing Outlook*. 56(5):268–74

89. Babu A, Templeton AK, Munshi A, Ramesh R. 2013. Nanoparticle-Based Drug Delivery for Therapy of Lung Cancer: Progress and Challenges. *Journal of Nanomaterials*. 2013:1–11

90. Sudha PN, Sangeetha K, Vijayalakshmi K, Barhoum A. 2018. Nanomaterials history, classification, unique properties, production and market. In *Emerging Applications of Nanoparticles and Architecture Nanostructures*, pp. 341–84. Elsevier

91. Pokropivny VV, Skorokhod VV. 2007. Classification of nanostructures by dimensionality and concept of surface forms engineering in nanomaterial science. *Materials Science and Engineering: C*. 27(5–8):990–93

92. Teleanu DM, Chircov C, Grumezescu AM, Volceanov A, Teleanu RI. 2019. Contrast Agents Delivery: An Up-to-Date Review of Nanodiagnostics in Neuroimaging. *Nanomaterials*. 9(4):542

93. Yi G, Hong SH, Son J, Yoo J, Park C, et al. 2018. Recent advances in nanoparticle carriers for photodynamic therapy. *Quant. Imaging Med. Surg.* 8(4):433–43

94. Ananikov VP. 2019. Organic–Inorganic Hybrid Nanomaterials. *Nanomaterials*. 9(9):1197

95. Berry CC. 2012. Applications of Inorganic Nanoparticles for Biotechnology. In *Frontiers of Nanoscience*. 4:159–80. Elsevier

96. Casais-Molina ML, Cab C, Canto G, Medina J, Tapia A. 2018. Carbon Nanomaterials for Breast Cancer Treatment. *Journal of Nanomaterials*. 2018:1–9

97. Albert K, Hsu H-Y. 2016. Carbon-Based Materials for Photo-Triggered Theranostic Applications. *Molecules*. 21(11):1585

98. Pacurari M, Qian Y, Fu W, Schwegler-Berry D, Ding M, et al. 2012. Cell Permeability, Migration, and Reactive Oxygen Species Induced by Multiwalled Carbon Nanotubes in Human Microvascular Endothelial Cells. *Journal of Toxicology and Environmental Health, Part A*. 75(2):112–28

99. Crouzier D, Follot S, Gentilhomme E, Flahaut E, Arnaud R, et al. 2010. Carbon nanotubes induce inflammation but decrease the production of reactive oxygen species in lung. *Toxicology*. 272(1–3):39–45

100. de Melo C, Jullien M, Battie Y, En Naciri A, Ghanbaja J, et al. 2018. Tunable Localized Surface Plasmon Resonance and Broadband Visible Photoresponse of Cu Nanoparticles/ZnO Surfaces. *ACS Appl. Mater. Interfaces*. 10(47):40958–65

101. Attia MF, Anton N, Wallyn J, Omran Z, Vandamme TF. 2019. An overview of active and passive targeting strategies to improve the nanocarriers efficiency to tumour sites. *J Pharm Pharmacol*. 71(8):1185–98

102. Reimann SM, Manninen M. 2002. Electronic structure of quantum dots. *Rev. Mod. Phys.* 74(4):1283–1342

103. Li Y, Yang X-Y, Feng Y, Yuan Z-Y, Su B-L. 2012. One-Dimensional Metal Oxide Nanotubes, Nanowires, Nanoribbons, and Nanorods: Synthesis, Characterizations, Properties and Applications. *Critical Reviews in Solid State and Materials Sciences*. 37(1):1–74

104. Kim H, Lee D. 2018. Near-Infrared-Responsive Cancer Photothermal and Photodynamic Therapy Using Gold Nanoparticles. *Polymers*. 10(9):961

105. Chen W, Ayala-Orozco C, Biswal NC, Perez-Torres C, Bartels M, et al. 2014. Targeting pancreatic cancer with magneto-fluorescent theranostic gold nanoshells. *Nanomedicine*. 9(8):1209–22

106. Skrabalak SE, Chen J, Sun Y, Lu X, Au L, et al. 2008. Gold Nanocages: Synthesis, Properties, and Applications. *Acc. Chem. Res.* 41(12):1587–95

107. Ungureanu C, Kroes R, Petersen W, Groothuis TAM, Ungureanu F, et al. 2011. Light Interactions with Gold Nanorods and Cells: Implications for Photothermal Nanotherapeutics. *Nano Lett.* 11(5):1887–94

108. Zhang Z, Wang L, Wang J, Jiang X, Li X, et al. 2012. Mesoporous Silica-Coated Gold Nanorods as a Light-Mediated Multifunctional Theranostic Platform for Cancer Treatment. *Adv. Mater.* 24(11):1418–23

109. Phillips E, Penate-Medina O, Zanzonico PB, Carvajal RD, Mohan P, et al. 2014. Clinical translation of an ultrasmall inorganic optical-PET imaging nanoparticle probe. *Science Translational Medicine*. 6:260ra149-260ra149

110. Ge J, Jia Q, Liu W, Lan M, Zhou B, et al. 2016. Carbon Dots with Intrinsic Theranostic Properties for Bioimaging, Red-Light-Triggered Photodynamic/Photothermal Simultaneous Therapy In Vitro and In Vivo. *Advanced Healthcare Materials*. 5:665–75

111. Chen F, Madajewski B, Ma K, Zanoni DK, Stambuk H, et al. 2019. Molecular phenotyping and image-guided surgical treatment of melanoma using spectrally distinct ultrasmall core-shell silica nanoparticles. *Science Advances*. 5(12):eaax5208

112. Hong Y, Lam JWY, Tang BZ. 2011. Aggregation-induced emission. *Chem. Soc. Rev.* 40(11):5361

113. Luo J, Xie Z, Lam JWY, Cheng L, Tang BZ, et al. 2001. Aggregation-induced emission of 1-methyl-1,2,3,4,5-pentaphenylsilole. *Chem. Commun.*, pp. 1740–41

114. Tang BZ, Zhao Z, Zhang H, Lam JWY. 2020. Aggregation-Induced Emission: New Vistas at Aggregate Level. *Angew. Chem. Int. Ed.*

115. Yang H, Liu Y, Guo Z, Lei B, Zhuang J, et al. 2019. Hydrophobic carbon dots with blue dispersed emission and red aggregation-induced emission. *Nat Commun*. 10(1):1789

116. Feng G, Mao D, Liu J, Goh CC, Ng LG, et al. 2018. Polymeric nanorods with aggregation-induced emission characteristics for enhanced cancer targeting and imaging. *Nanoscale*. 10(13):5869–74

117. Dong J, Li X, Zhang K, Di Yuan Y, Wang Y, et al. 2018. Confinement of Aggregation-Induced Emission Molecular Rotors in Ultrathin Two-Dimensional Porous Organic Nanosheets for Enhanced Molecular Recognition. *J. Am. Chem. Soc.* 140(11):4035–46

118. Li D, Zhao X, Qin W, Zhang H, Fei Y, et al. 2016. Toxicity assessment and long-term three-photon fluorescence imaging of bright aggregation-induced emission nanodots in zebrafish. *Nano Res.* 9(7):1921–33

119. Henson PM, Hume DA. 2006. Apoptotic cell removal in development and tissue homeostasis. *Trends Immunol.* 27(5):244–50

120. Cheng H, Wang Z, Fu L, Xu T. 2019. Macrophage polarization in the development and progression of ovarian cancers: an overview. *Front Oncol*. 9:

121. Negus RP, Stamp GW, Relf MG, Burke F, Malik ST, et al. 1995. The detection and localization of monocyte chemoattractant protein-1 (MCP-1) in human ovarian cancer. *J. Clin. Invest.* 95(5):2391–96

122. Kousis PC, Henderson BW, Maier PG, Gollnick SO. 2007. Photodynamic therapy enhancement of antitumor immunity is regulated by neutrophils. *Cancer Res.* 67(21):10501–10

123. Sano K, Nakajima T, Choyke PL, Kobayashi H. 2014. The effect of photoimmunotherapy (PIT) followed by liposomal daunorubicin in a mixed tumor model:

A demonstration of the super enhanced permeability and retention (SUPR) effect after PIT. *Mol Cancer Ther*. 13(2):426–32

124. Li W, Yang J, Luo L, Jiang M, Qin B, et al. 2019. Targeting photodynamic and photothermal therapy to the endoplasmic reticulum enhances immunogenic cancer cell death. *Nat Commun*. 10:

125. Golombek SK, May J-N, Theek B, Appold L, Drude N, et al. 2018. Tumor Targeting via EPR: Strategies to Enhance Patient Responses. *Adv Drug Deliv Rev*. 130:17–38

126. Tanaka N, Kanatani S, Tomer R, Sahlgren C, Kronqvist P, et al. 2017. Whole-tissue biopsy phenotyping of three-dimensional tumours reveals patterns of cancer heterogeneity. *Nat Biomed Eng*. 1(10):796–806

127. Kato A, Kataoka H, Yano S, Hayashi K, Hayashi N, et al. 2017. Maltotriose Conjugation to a Chlorin Derivative Enhances the Antitumor Effects of Photodynamic Therapy in Peritoneal Dissemination of Pancreatic Cancer. *Mol Cancer Ther*. 16(6):1124–32

128. Tanaka M, Kataoka H, Yano S, Ohi H, Moriwaki K, et al. 2014. Antitumor Effects in Gastrointestinal Stromal Tumors Using Photodynamic Therapy with a Novel Glucose-Conjugated Chlorin. *Mol Cancer Ther*. 13(4):767–75

129. Yan S, Huang Q, Chen J, Song X, Chen Z, et al. 2019. *Tumor-targeting photodynamic therapy based on folate-modified polydopamine nanoparticles*. International Journal of Nanomedicine.

130. Yoon HY, Koo H, Choi KY, Lee SJ, Kim K, et al. 2012. Tumor-targeting hyaluronic acid nanoparticles for photodynamic imaging and therapy. *Biomaterials*. 33(15):3980–89

131. Aung W, Tsuji AB, Sugyo A, Takashima H, Yasunaga M, et al. 2018. Near-infrared photoimmunotherapy of pancreatic cancer using an indocyanine green-labeled anti-tissue factor antibody. *World J Gastroenterol*. 24(48):5491–5504

132. Debie P, Hernot S. 2019. Emerging Fluorescent Molecular Tracers to Guide Intra-Operative Surgical Decision-Making. *Front Pharmacol*. 10:

133. Schmidt MM, Wittrup KD. 2009. A modeling analysis of the effects of molecular size and binding affinity on tumor targeting. *Mol. Cancer Ther.* 8(10):2861–71

134. Sano K, Nakajima T, Choyke PL, Kobayashi H. 2013. Markedly enhanced permeability and retention effects induced by photo-immunotherapy of tumors. *ACS Nano*. 7(1):717–24

135. Gao W, Wang Z, Lv L, Yin D, Chen D, et al. 2016. Photodynamic Therapy Induced Enhancement of Tumor Vasculature Permeability Using an Upconversion Nanoconstruct for Improved Intratumoral Nanoparticle Delivery in Deep Tissues. *Theranostics*. 6(8):1131–44

136. Boni L, David G, Mangano A, Dionigi G, Rausei S, et al. 2015. Clinical applications of indocyanine green (ICG) enhanced fluorescence in laparoscopic surgery. *Surg Endosc*. 29(7):2046–55

137. Henderson BW, Busch TM, Snyder JW. 2006. Fluence rate as a modulator of PDT mechanisms. *Lasers Surg Med*. 38(5):489–93

138. Sitnik TM, Henderson BW. 1998. The effect of fluence rate on tumor and normal tissue responses to photodynamic therapy. *Photochem. Photobiol.* 67(4):462–66

139. Müller S, Walt H, Dobler-Girdziunaite D, Fiedler D, Haller U. 1998. Enhanced photodynamic effects using fractionated laser light. *Journal of Photochemistry and Photobiology B: Biology*. 42(1):67–70

140. de Bruijn HS, Brooks S, van der Ploeg-van den Heuvel A, ten Hagen TLM, de Haas ERM, Robinson DJ. 2016. Light Fractionation Significantly Increases the Efficacy of Photodynamic Therapy Using BF-200 ALA in Normal Mouse Skin. *PLoS One*. 11(2):

141. Weersink RA, Bogaards A, Gertner M, Davidson SRH, Zhang K, et al. 2005. Techniques for delivery and monitoring of TOOKAD (WST09)-mediated photodynamic therapy of the prostate: clinical experience and practicalities. *J. Photochem. Photobiol. B, Biol.* 79(3):211–22

142. Li J, Zhu TC. 2008. Determination of in vivo light fluence distribution in a heterogeneous prostate during photodynamic therapy. *Phys Med Biol*. 53(8):2103–14

143. Espina V, Mariani BD, Gallagher RI, Tran K, Banks S, et al. 2010. Malignant precursor cells pre-exist in human breast DCIS and require autophagy for survival. *PLoS ONE*. 5(4):e10240

144. Smith AG, Macleod KF. 2019. Autophagy, cancer stem cells and drug resistance. *J Pathol*. 247(5):708–18

145. Kim J, Lim W, Kim S, Jeon S, Hui Z, et al. 2014. Photodynamic therapy (PDT) resistance by PARP1 regulation on PDT-induced apoptosis with autophagy in head and neck cancer cells. *J. Oral Pathol. Med.* 43(9):675–84

146. Wei M-F, Chen M-W, Chen K-C, Lou P-J, Lin SY-F, et al. 2014. Autophagy promotes resistance to photodynamic therapy-induced apoptosis selectively in colorectal cancer stem-like cells. *Autophagy*. 10(7):1179–92

147. Domagala A, Stachura J, Gabrysiak M, Muchowicz A, Zagozdzon R, et al. 2018. Inhibition of autophagy sensitizes cancer cells to Photofrin-based photodynamic therapy. *BMC Cancer*. 18:

148. Cincotta L, Szeto D, Lampros E, Hasan T, Cincotta AH. 1996. Benzophenothiazine and benzoporphyrin derivative combination phototherapy effectively eradicates large murine sarcomas. *Photochem. Photobiol.* 63(2):229–37

149. Chen M, Xie S. 2018. Therapeutic targeting of cellular stress responses in cancer. *Thorac Cancer*. 9(12):1575–82

150. Fahey JM, Girotti AW. 2017. Nitric oxide-mediated resistance to photodynamic therapy in a human breast tumor xenograft model: Improved outcome with NOS2 inhibitors. *Nitric Oxide*. 62:52–61

151. Bhowmick R, Girotti AW. 2011. Rapid upregulation of cytoprotective nitric oxide in breast tumor cells subjected to a photodynamic therapy-like oxidative challenge. *Photochem Photobiol*. 87(2):378–86

152. Korbelik M, Parkins CS, Shibuya H, Cecic I, Stratford MRL, Chaplin DJ. 2000. Nitric oxide production by tumour tissue: impact on the response to photodynamic therapy. *Br J Cancer*. 82(11):1835–43

153. Henderson BW, Sitnik-Busch TM, Vaughan LA. 1999. Potentiation of photodynamic therapy antitumor activity in mice by nitric oxide synthase inhibition is fluence rate dependent. *Photochem. Photobiol.* 70(1):64–71

154. Hanahan D, Weinberg RA. 2000. The Hallmarks of Cancer. *Cell*. 100(1):57–70

155. Casas A, Di Venosa G, Hasan T, Batlle A. 2011. Mechanisms of Resistance to Photodynamic Therapy. *Curr Med Chem*. 18(16):2486–2515

156. Weijer R, Broekgaarden M, van Golen RF, Bulle E, Nieuwenhuis E, et al. 2015. Low-power photodynamic therapy induces survival signaling in perihilar cholangiocarcinoma cells. *BMC Cancer*. 15:1014

157. Morgan J, Jackson JD, Zheng X, Pandey SK, Pandey RK. 2010. Substrate affinity of photosensitizers derived from chlorophyll-a: the ABCG2 transporter affects the phototoxic response of side population stem cell-like cancer cells to photodynamic therapy. *Mol. Pharm.* 7(5):1789–1804

158. Kishen A, Upadya M, Tegos GP, Hamblin MR. 2010. Efflux pump inhibitor potentiates antimicrobial photodynamic inactivation of Enterococcus faecalis biofilm. *Photochem. Photobiol.* 86(6):1343–49

159. Sharkey SM, Wilson BC, Moorehead R, Singh G. 1993. Mitochondrial alterations in photodynamic therapy-resistant cells. *Cancer Res.* 53(20):4994–99

160. Shen XY, Zacal N, Singh G, Rainbow AJ. 2005. Alterations in Mitochondrial and Apoptosis-regulating Gene Expression in Photodynamic Therapy-resistant Variants of HT29 Colon Carcinoma Cells¶. *phot*. 81(2):306–13

161. Bayat Mokhtari R, Homayouni TS, Baluch N, Morgatskaya E, Kumar S, et al. 2017. Combination therapy in combating cancer. *Oncotarget*. 8(23):38022–43

162. Cuperus R, van Kuilenburg ABP, Leen R, Bras J, Caron HN, Tytgat GAM. 2011. Promising effects of the 4HPR-BSO combination in neuroblastoma monolayers and spheroids. *Free Radic. Biol. Med.* 51(6):1213–20

163. Kimani SG, Phillips JB, Bruce JI, MacRobert AJ, Golding JP. 2012. Antioxidant inhibitors potentiate the cytotoxicity of photodynamic therapy. *Photochem. Photobiol.* 88(1):175–87

164. Smith D, O'Leary VJ, Darley-Usmar VM. 1993. The role of α-tocopherol as a peroxyl radical scavenger in human low density lipoprotein. *Biochemical Pharmacology*. 45:2195–2201

165. Chen Q, Feng L, Liu J, Zhu W, Dong Z, et al. 2016. Intelligent Albumin-MnO2 Nanoparticles as pH-/H2 O2 -Responsive Dissociable Nanocarriers to Modulate Tumor Hypoxia for Effective Combination Therapy. *Adv. Mater. Weinheim*. 28(33):7129–36

166. Yang G, Xu L, Chao Y, Xu J, Sun X, et al. 2017. Hollow MnO 2 as a tumor-microenvironment-responsive biodegradable nano-platform for combination therapy favoring antitumor immune responses. *Nat Commun*. 8(1):1–13

167. Fan H, Yan G, Zhao Z, Hu X, Zhang W, et al. 2016. Inside Back Cover: A Smart Photosensitizer–Manganese Dioxide Nanosystem for Enhanced Photodynamic Therapy by Reducing Glutathione Levels in Cancer Cells (Angew. Chem. Int. Ed. 18/2016). *Angewandte Chemie International Edition*. 55(18):5611–5611

168. Singer E, Judkins J, Salomonis N, Matlaf L, Soteropoulos P, et al. 2015. Reactive oxygen species-mediated therapeutic response and resistance in glioblastoma. *Cell Death Dis*. 6(1):e1601

169. Ling X, Zhang S, Liu Y, Bai M. 2018. Light-activatable cannabinoid prodrug for combined and target-specific photodynamic and cannabinoid therapy. *J Biomed Opt*. 23(10):1–9

170. Anand S, Yasinchak A, Bullock T, Govande M, Maytin EV. 2019. A non-toxic approach for treatment of breast cancer and its metastases: capecitabine enhanced photodynamic therapy in a murine breast tumor model. *J Cancer Metastasis Treat*. 5:

171. Anand S, Rollakanti KR, Horst RL, Hasan T, Maytin EV. 2014. Combination of oral vitamin D3 with photodynamic therapy enhances tumor cell death in a murine model of cutaneous squamous cell carcinoma. *Photochem. Photobiol.* 90(5):1126–35

172. Fukuhara H, Inoue K, Kurabayashi A, Furihata M, Fujita H, et al. 2013. The inhibition of ferrochelatase enhances 5-aminolevulinic acid-based photodynamic action for prostate cancer. *Photodiagnosis Photodyn Ther*. 10(4):399–409

173. Xu T, Ding W, Ji X, Ao X, Liu Y, et al. 2019. Molecular mechanisms of ferroptosis and its role in cancer therapy. *J Cell Mol Med*. 23(8):4900–4912

174. Chen G, Guo G, Zhou X, Chen H. 2020. Potential mechanism of ferroptosis in pancreatic cancer. *Oncol Lett*. 19(1):579–87

175. Eling N, Reuter L, Hazin J, Hamacher-Brady A, Brady NR. 2015. Identification of artesunate as a specific activator of ferroptosis in pancreatic cancer cells. *Oncoscience*. 2(5):517–32

176. Anayo L, Magnussen A, Perry A, Wood M, Curnow A. 2018. An experimental investigation of a novel iron chelating protoporphyrin IX prodrug for the enhancement of photodynamic therapy. *Lasers Surg Med*. 50(5):552–65

177. Curnow A, Perry A, Wood M. 2019. Improving in vitro photodynamic therapy through the development of a novel iron chelating aminolaevulinic acid prodrug. *Photodiagnosis Photodyn Ther*. 25:157–65

178. Mrozek-Wilczkiewicz A, Malarz K, Rams-Baron M, Serda M, Bauer D, et al. 2017. Iron Chelators and Exogenic Photosensitizers. Synergy through Oxidative Stress Gene Expression. *J Cancer*. 8(11):1979–87

179. Biswas R, Chung P-S, Moon JH, Lee S-H, Ahn J-C. 2014. Carboplatin synergistically triggers the efficacy of photodynamic therapy via caspase 3-, 8-, and 12-dependent pathways in human anaplastic thyroid cancer cells. *Lasers Med Sci*. 29(3):995–1007

180. Cheng Y-S, Peng Y-B, Yao M, Teng J-P, Ni D, et al. 2017. Cisplatin and photodynamic therapy exert synergistic inhibitory effects on small-cell lung cancer cell viability and xenograft tumor growth. *Biochem. Biophys. Res. Commun.* 487(3):567–72

181. Ahn T-G, Jung JM, Lee E-J, Choi JH. 2019. Effects of cisplatin on photosensitizer-mediated photodynamic therapy in breast tumor-bearing nude mice. *Obstet Gynecol Sci*. 62(2):112–19

182. Pogue BW, O'Hara JA, Demidenko E, Wilmot CM, Goodwin IA, et al. 2003. Photodynamic therapy with verteporfin in the radiation-induced fibrosarcoma-1 tumor causes enhanced radiation sensitivity. *Cancer Res.* 63(5):1025–33

183. Xu J, Gao J, Wei Q. 2016. *Combination of Photodynamic Therapy with Radiotherapy for Cancer Treatment*. Journal of Nanomaterials.

184. Mroz P, Hashmi JT, Huang Y-Y, Lange N, Hamblin MR. 2011. Stimulation of anti-tumor immunity by photodynamic therapy. *Expert Rev Clin Immunol*. 7(1):75–91

185. Sharma P, Allison JP. 2015. The future of immune checkpoint therapy. *Science*. 348(6230):56–61

186. He C, Duan X, Guo N, Chan C, Poon C, et al. 2016. Core-shell nanoscale coordination polymers combine chemotherapy and photodynamic therapy to potentiate checkpoint blockade cancer immunotherapy. *Nat Commun*. 7:

187. Castano AP, Hamblin MR. 2006. Immune stimulation and photodynamic therapy to treat a metastatic model of breast cancer. *Cancer Res*. 66(8 Supplement):1122–23

188. Li X, Le H, Wolf RF, Chen VA, Sarkar A, et al. 2011. Long-term effect on EMT6 tumors in mice induced by combination of laser immunotherapy and surgery. *Integr Cancer Ther*. 10(4):368–73

189. Gayl Schweitzer V. 2001. Photofrin-Mediated Photodynamic Therapy for Treatment of Aggressive Head and Neck Nonmelanomatous Skin Tumors in Elderly Patients: *The Laryngoscope*. 111(6):1091–98

190. Shishkova N, Kuznetsova O, Berezov T. 2012. Photodynamic therapy for gynecological diseases and breast cancer. *Cancer Biol Med .* 9(1):9–17

191. Cramer SW, Chen CC. 2020. Photodynamic Therapy for the Treatment of Glioblastoma. *Front. Surg.* 6:81

192. Railkar R, Agarwal PK. 2018. Photodynamic Therapy in the Treatment of Bladder Cancer: Past Challenges and Current Innovations. *Eur Urol Focus*. 4(4):509–11

193. Ericson MB, Wennberg, AM, Larkö O. 2008. Review of photodynamic therapy in actinic keratosis and basal cell carcinoma. *Therapeutics and Clinical Risk Management*. 4(1):1–9

194. Geavlete B, Mulţescu R, Georgescu D, Geavlete P. 2008. Hexvix blue light fluorescence cystoscopy – a promising approach in superficial bladder tumors diagnosis. *Journal of Medicine and Life*. 1(3):355-362.

195. Huggett MT, Jermyn M, Gillams A, Illing R, Mosse S, et al. 2014. Phase I/II study of verteporfin photodynamic therapy in locally advanced pancreatic cancer. *Br J Cancer*. 110(7):1698–1704

196. Akimoto J. 2016. Photodynamic Therapy for Malignant Brain Tumors. *Neurol. Med. Chir.(Tokyo)*. 56(4):151–57

197. Ishida N, Osawa S, Miyazu T, Kaneko M, Tamura S, et al. 2020. Photodynamic Therapy Using Talaporfin Sodium for Local Failure after Chemoradiotherapy or Radiotherapy for Esophageal Cancer: A Single Center Experience. *JCM*. 9(5):1509

198. Sahu A, Choi WI, Lee JH, Tae G. 2013. Graphene oxide mediated delivery of methylene blue for combined photodynamic and photothermal therapy. *Biomaterials*. 34(26):6239–48

199. Xie L, Wang G, Zhou H, Zhang F, Guo Z, et al. 2016. Functional long circulating single walled carbon nanotubes for fluorescent/photoacoustic imaging-guided enhanced phototherapy. *Biomaterials*. 103:219–28

200. Choudhury P, Das PK. 2019. Carbon Dots-Stimulated Amplification of Aggregation-Induced Emission of Size-Tunable Organic Nanoparticles. *Langmuir*. 35(32):10582–95

201. Shi C, Wu JB, Chu GCY, Li Q, Wang R, et al. 2014. Heptamethine carbocyanine dye-mediated near-infrared imaging of canine and human cancers through the HIF-1α/OATPs signaling axis. *Oncotarget*. 5:10114–26

202. Guo W, Qiu Z, Guo C, Ding D, Li T, et al. 2017. Multifunctional Theranostic Agent of $Cu_2(OH)PO_4$ Quantum Dots for Photoacoustic Image-Guided Photothermal/Photodynamic Combination Cancer Therapy. *ACS Appl. Mater. Interfaces*. 9(11):9348–58

203. Liu X, Braun GB, Qin M, Ruoslahti E, Sugahara KN. 2017. In vivo cation exchange in quantum dots for tumor-specific imaging. *Nat Commun*. 8(1):343

204. Topete A, Alatorre-Meda M, Iglesias P, Villar-Alvarez EM, Barbosa S, et al. 2014. Fluorescent Drug-Loaded, Polymeric-Based, Branched Gold Nanoshells for Localized Multimodal Therapy and Imaging of Tumoral Cells. *ACS Nano*. 8(3):2725–38

205. Li Y, Tang R, Liu X, Gong J, Zhao Z, et al. 2020. Bright Aggregation-Induced Emission Nanoparticles for Two-Photon Imaging and Localized Compound Therapy of Cancers. *ACS Nano*

206. Dong Q, Yang H, Wan C, Zheng D, Zhou Z, et al. 2019. Her2-Functionalized Gold-Nanoshelled Magnetic Hybrid Nanoparticles: a Theranostic Agent for Dual-Modal Imaging and Photothermal Therapy of Breast Cancer. *Nanoscale Res Lett*. 14(1):235

CHAPTER 2.

MODULATING CELLULAR CYTOTOXICITY AND PHOTOTOXICITY OF FLUORESCENT ORGANIC SALTS THROUGH COUNTERION PAIRING

2.1 PREFACE

This chapter is a modified version of a previously published article:

> Broadwater D. M.*, Bates M. P.*, Jayaram M., Young M., Raithel A. L., Hamann T. W., Zhang W., Borhan B., Lunt R. R., Lunt S. Y. 2019. Modulating cellular cytotoxicity and phototoxicity of fluorescent organic salts through counterion pairing. *Scientific Reports*, *9*, 15288.
>
> *Co-first authors

2.2 Abstract

Light-activated theranostics offer promising opportunities for disease diagnosis, image-guided surgery, and site-specific personalized therapy. However, current fluorescent dyes are limited by low brightness, high cytotoxicity, poor tissue penetration, and unwanted side effects. To overcome these limitations, we demonstrate a platform for optoelectronic tuning, which allows independent control of the optical properties from the electronic properties of fluorescent organic salts. This is achieved through cation-anion pairing of organic salts that can modulate the frontier molecular orbital without impacting the bandgap. Optoelectronic tuning enables decoupled control over the cytotoxicity and phototoxicity of fluorescent organic salts by selective generation of mitochondrial reactive oxygen species that control cell viability. In this chapter, we show that through counterion pairing, organic salt nanoparticles can be tuned to be either nontoxic for enhanced imaging, or phototoxic for improved photodynamic therapy.

2.3 Introduction

Fluorescent dyes offer great potential as both diagnostic and therapeutic agents and the combined application has been termed “theranostics”. These compounds can be used to improve cancer diagnoses, assist with image-guided surgery, and treat tumors by photodynamic therapy (PDT). Theranostic agents localize in tumors and become activated by a specific wavelength of light to either emit a different wavelength of light that can be detected for imaging, or generate reactive species for PDT (1, 2). PDT provides double selectivity through the use of both the dye and light, with the goal of minimizing side effects from the dye or light alone (3). To realize the full potential of fluorescent dyes in biomedical applications, it is necessary to increase their brightness

and tissue penetration in order to detect and treat deeply embedded tumors, while also eliminating unwanted side effects.

Fluorescent dyes that absorb and emit in the near-infrared (NIR) range offer several advantages for both PDT and *in vivo* imaging applications. While visible light (400-650 nm) travels only millimeters in tissues, NIR light (650–1200 nm) can travel centimeters (4): 810 nm and 980 nm NIR light have been shown to penetrate 3 cm of skin, skull, and brain tissue (5). Additionally, visible light absorbance by endogenous biological fluorophores such as heme and flavin groups (6) causes autofluorescence and weak signal intensity. On the other hand, NIR light is minimally absorbed by biological material, drastically reducing background noise and increasing penetrance (7, 8). FDA-approved NIR-responsive fluorescent dyes including indocyanine green, 5-aminolevulinic acid, and methylene blue are available and used in medical diagnostics (9) but are limited due to their low level of brightness. Other commercially available NIR-responsive fluorescent dyes include heptamethine cyanine (Cy7), Alexa Fluor 750, and heptamethine dye IR-808 (10–12). However, these dyes display low brightness, high toxicity, and poor aqueous stability (13). Recent PDT-based nanocrystals show energy level tunability via surface ligand modification but have poor biocompatibility due to heavy elements and minute absorbance in the NIR range that stem from a lack of oscillator strength near their bandgap. For example, semiconductor nanocrystals have absorption coefficients of ~10^3/cm for PbS and PbSe compared to ~10^6/cm for cyanines with bandgaps around 850 nm – this translates to 1000 times less absorption per nanometer of material by nanocrystals (**Figure 2.1**).

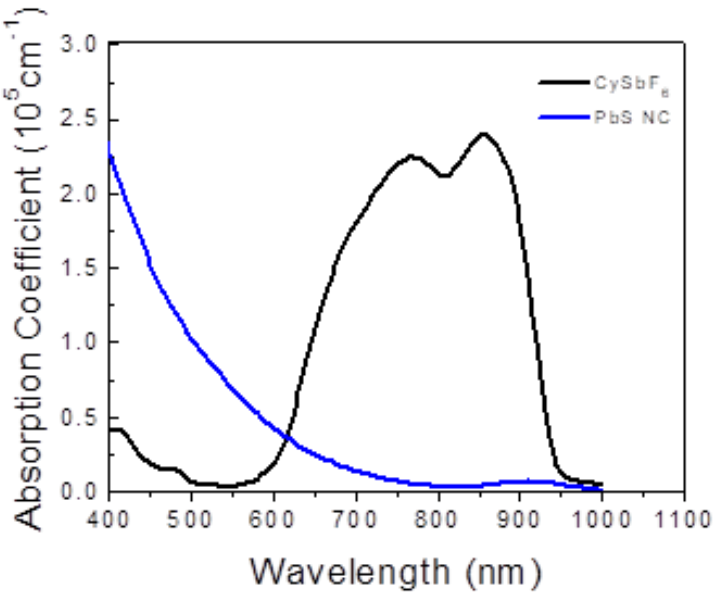

Figure 2.1 Solid state absorption coefficient versus wavelength comparison for an exemplary organic salt ($CySbF_6$) and nanocrystal (PbS), both with bandgap around 1.3 eV. The organic salt has an absorption coefficient that is orders of magnitude larger than that for the nanocrystal at wavelengths in the near-infrared around the bandgap (650-950 nm).

Fluorescent organic salts, composed of a fluorescent ion and a counterion, have been developed to increase aqueous solubility and photostability (14, 15). The counterion has largely been thought to have little impact on the properties of the fluorescent organic salts. Only a few reports have investigated the impact of the counterion but have been limited to encapsulated matrices for modestly increasing the quantum yield (16–19), or have shown no impact on toxicity (20, 21). The latter study investigated two anions with a visible rhodamine dye but showed no significant difference in cell viability between the two key anions in a range of cell lines (Hs578Bst, Hs578T, and MDA-MB-231) and did not investigate phototoxicity (20). Here, we focus on NIR-responsive polymethine cyanine dyes, which have been used as effective theranostic agents (10, 22). Heterocyclic polymethine cyanine dyes have been found to

preferentially accumulate in tumors and circulating cancer cells (23) even in the absence of bioconjugation to tumor-targeting molecules. This is hypothesized to occur through a mechanism mediated by increased expression of organic anion transporter polypeptides (OATPs) and hypoxia-inducible factor 1-alpha (HIF1α), both of which are upregulated in cancer cells (24). HIF1α promotes tumor angiogenesis and expression of OATPs, which facilitate the uptake of polymethine cyanine dyes (25), as shown by competitive inhibition of OATP1B3 (22). Lipophilic photosensitizers may also associate into circulating low-density lipoproteins (LDLs) and be imported by cells via ATP-mediated endocytosis (26). Charged molecules taken up by the cell accumulate in organelles such as mitochondria and lysosomes, where light irradiation can induce generation of reactive oxygen species (ROS) (27). While the exact mode of uptake and localization varies depending on the chemical characteristics of any given photosensitizer, these mechanisms are uniquely active in tumor cells, leading to tumor-specific accumulation and retention (28).

Cellular toxicity of fluorescent molecules is caused by the combination of 1) cytotoxicity – toxicity in the dark, independent of photoexcitation; and 2) phototoxicity – toxicity with light illumination, or photoexcitation. While the tumor-specific accumulation of polymethine cyanine dyes reduces their nonspecific toxicity, low levels of systemic toxicity remain due to the cytotoxicity of unexcited molecules (28). For applications in tumor imaging, both cytotoxicity and phototoxicity need to be reduced to minimize side effects. For applications in PDT, cytotoxicity must be eliminated, while phototoxicity should be enhanced to selectively kill cancer cells with targeted light therapy.

We recently reported that a range of weakly coordinating anions can modulate frontier molecular orbital levels of a photoactive heptamethine cyanine cation (Cy^+) in solar cells without changing the bandgap (29, 30). Thus, we are able to control the electronics (i.e. frontier molecular orbitals) of photoactive molecules independently from their optical properties (i.e. bandgaps). We have subsequently employed this electronic tunability to demonstrate cyanine-based organic salt photovoltaics with > 7 year lifetime under typical solar illumination (31).

Here, we demonstrate the impact of the counterion on independently controlling both cytotoxicity and phototoxicity of fluorescent organic salts in cancer cells for enhanced imaging and improved PDT (**Figure 2.2A**). We achieve this by pairing the NIR-absorbing Cy^+ with various dipole-modulating counterions and characterizing their effect on human lung carcinoma and metastatic human melanoma cell lines. We find that counterion pairings with small hard anions lead to high cytotoxicity even at low concentrations. In comparison, counterion pairings with bulkier, halogenated anions display low cytotoxicity even at 20x higher concentrations. We further report a distinct intermediate group of anion pairings that are highly phototoxic, but exhibit negligible cytotoxicity, making them ideal photosensitizers for PDT. This concept of tuning the cytotoxicity and phototoxicity of fluorescent organic salts is a new platform for controlling the photoexcited interactions at the cellular level. It opens new opportunities for greater tissue penetration and the potential for minimizing side effects. Moreover, this approach may be applied to both novel and existing luminophores, including assembled fluorescent probes, phosphors, nanocrystals, and other hybrid nanoparticles (32–36).

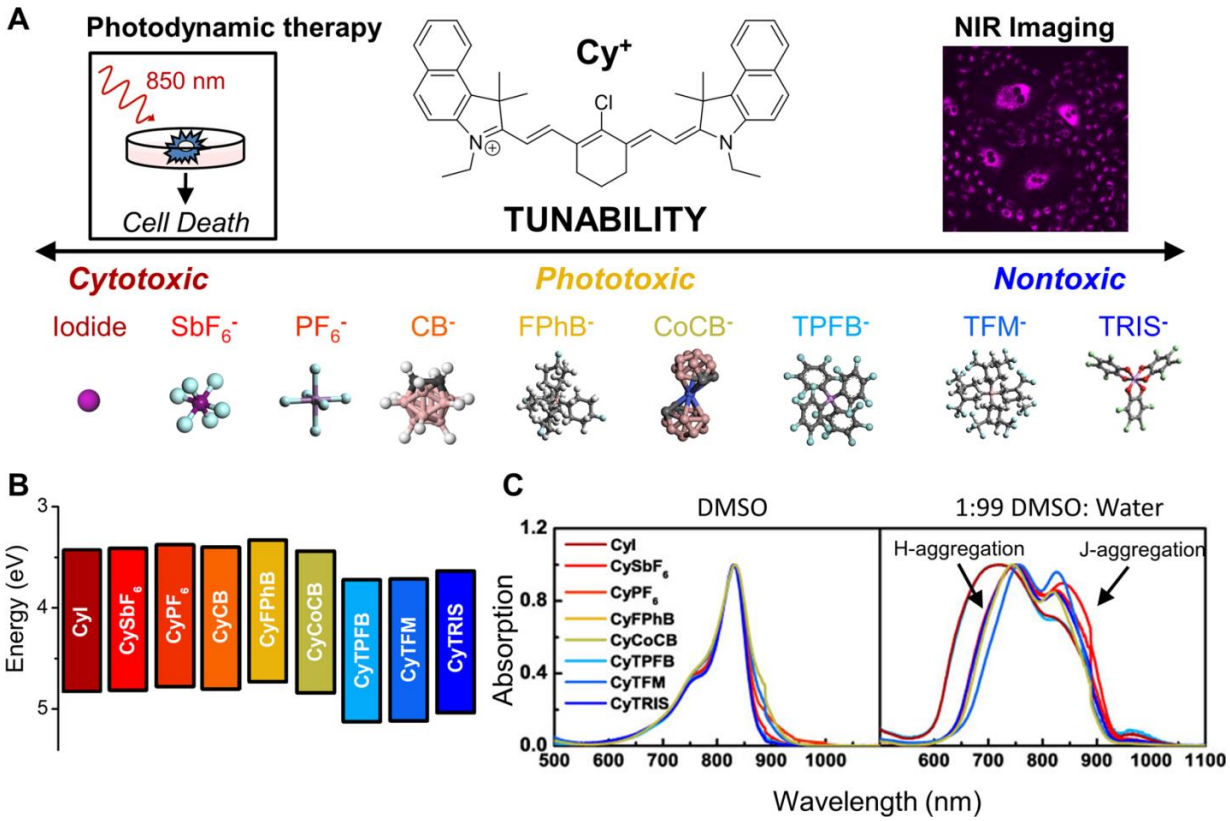

Figure 2.2 Pairing a fluorescent cation such as heptamethine cyanine (Cy^+) with varying counterions enables tunability in cellular toxicity through optoelectronic control to improve near-infrared (NIR) imaging and photodynamic therapy. (**A**) Anions on the left are generally cytotoxic, anions in the middle are selectively phototoxic and ideal for applications in photodynamic therapy, and anions on the right reduce toxicity for applications in fluorescence imaging. Anions: Iodide (I^-); hexafluoroantimonate (SbF_6^-); hexafluorophosphate (PF_6^-); o-carborane (CB^-); terraces(4-fluorophenyl)borate ($FPhB^-$); cobalticarborane ($CoCB^-$); tetrakis (pentafluorophenyl) borate ($TPFB^-$); tetrakis[3,5-bis(trifluoro methyl)phenyl]borate (TFM^-); Δ-tris(tetrachloro-1,2-benzene diolato) phosphate(V) ($TRIS^-$). (**B)** The counterion shifts the HOMO energy level while allowing the band gap to remain the same. Ultraviolet photoelectron spectroscopy (UPS) was used to measure the frontier energy levels of Cy^+ with indicated counterion pairings in the solid state. Data were extracted from Suddard *et al*. (29) and Traverse *et al*. (31). (**C**) Fluorescent organic salts aggregate in aqueous environments. Organic salts fully dissolved in DMSO have a clear maximum at 830 nm with a leading shoulder when characterized with UV-Vis spectroscopy. However, in aqueous solution combinations of H- and J-aggregation of organic salts can be seen by blue-shifted peaks (lower wavelength) and red-shifted peaks (higher wavelength), respectively.

2.4 Results

2.4.1. Characterization of fluorescent organic salts

Heptamethine cyanine cation (Cy^+; **Figure 2.2A**) is a photoactive cation that absorbs and emits in NIR wavelengths, with a bandgap of 1.3 eV (**Figure 2.2B**). A range of anions were tested with Cy^+ and $Cy7^+$ based on our previous studies that demonstrated a full range of valence energy levels tailored by over 1 eV (29, 31). These include: hard anions iodide (I^-), hexafluoroantimonate (SbF_6^-), and hexafluorophosphate (PF_6^-), o-carborane (CB^-); and bulkier soft anions tetrakis(4-fluorophenyl)borate ($FPhB^-$), cobalticarborane ($CoCB^-$), tetrakis (pentafluorophenyl) borate ($TPFB^-$), tetrakis[3,5-bis(trifluoro methyl)phenyl]borate (TFM^-), and Δ-tris(tetrachloro-1,2-benzene diolato) phosphate(V) (referred to as Δ-TRISPHAT$^-$, further abbreviated as TRIS$^-$) (**Figure 2.3**). The counterion causes distinct shifts in the highest occupied molecular orbital (HOMO)

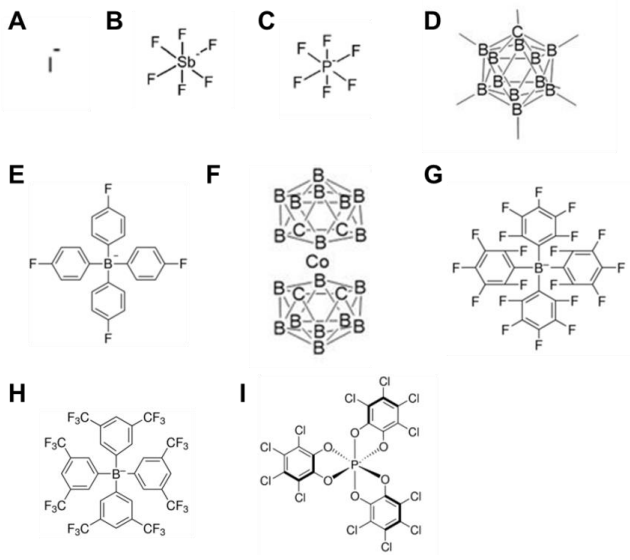

Figure 2.3 Molecular structures of anions investigated in the study. (**A**) Iodide (I^-) (**B**) Hexafluoroantimonate (SbF_6^-) (**C**) Hexafluorophosphate (PF_6^-) (**D**) O-carborane (CB^-) (**E**) Tetrakis(4-fluorophenyl)borate ($FPhB^-$) (**F**) Cobalticarborane ($CoCB^-$) (**G**) Tetrakis (pentafluorophenyl) borate ($TPFB^-$) (**H**) Tetrakis[3,5-bis(trifluoro methyl)phenyl]borate (TFM^-) (**I**) Δ-Tris(tetrachloro-1,2-benzene diolato) phosphate(V) ($TRIS^-$).

energy levels of heptamethine cyanine salts without changing the size of the bandgap in the solid state (**Figure 2.2B**). These changes to energy level are found to be consistent for salt nanoparticles in aqueous solution by measuring shifts to the redox potential and zeta potential (**Figure 2.4A-B, Table S2.1**), both of which have been correlated to

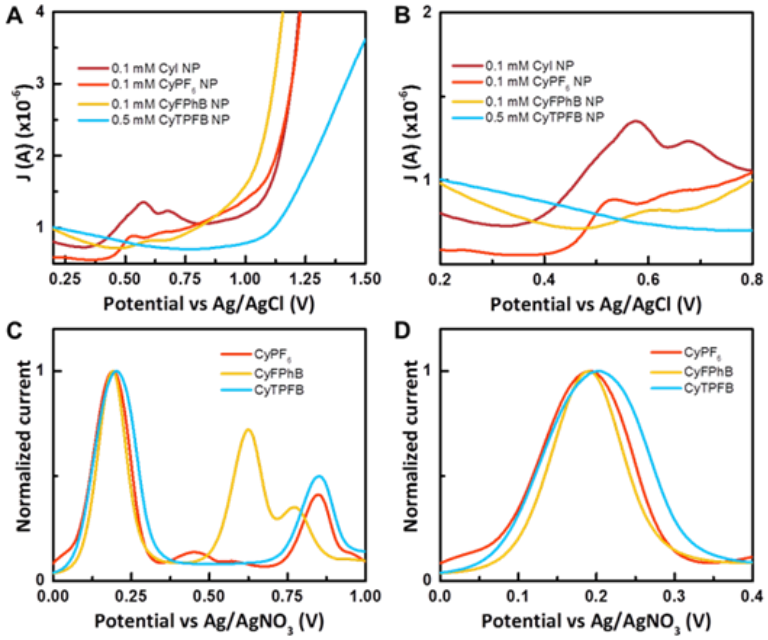

Figure 2.4 Differential pulse voltammetry measurements. (**A**, **B**) Nanoparticles (NPs) of the salts at 0.1 mM in 10% DMSO (CyI, $CyPF_6$) and 50% DMSO (CyFPhB) in water. CyTPFB NPs have greater solubility and were tested at 0.5 mM in 50% DMSO. (**C**, **D**) Monomer solutions of a representative cytotoxic, phototoxic, and nontoxic salt in acetonitrile. None of the differential pulse voltammetry measurements were performed in the presence of cells. Monomers demonstrate similar initial oxidation peaks, while nanoparticles have different peak locations. The CyTPFB nanoparticle oxidation peak is outside the redox window available for DMSO/H_2O mixtures. A lower peak potential for $CyPF_6$ compared to CyI and the shift out of the redox window for CyTPFB match anionic effects on the HOMO level shown in the solid state with UPS and correlated to redox levels. CyFPhB nanoparticles show a shift but do not fit the expected redox-HOMO trend. Monomers do not display this trend because their electronic environments are identical after dissociation due to the supporting electrolyte's higher concentration. DMSO/water solutions were measured with an Ag/AgCl reference electrode (-45 mV vs SCE), acetonitrile with a $Ag/AgNO_3$ electrode (0.36 V vs SCE).

HOMO (37, 38). The optical properties of the different ion-counterion pairings remain the same, with equivalent quantum yields and absorbance/emission spectra (**Figure 2.2C, Figure 2.5, Table S2.2)**. In DMSO, fully dissolved salt monomers display a major peak at 833 nm and a minor shoulder at 764 nm (and no observable shifts in redox potential between various salts as shown in **Figure 2.4C-D**). Organic salt nanoparticles

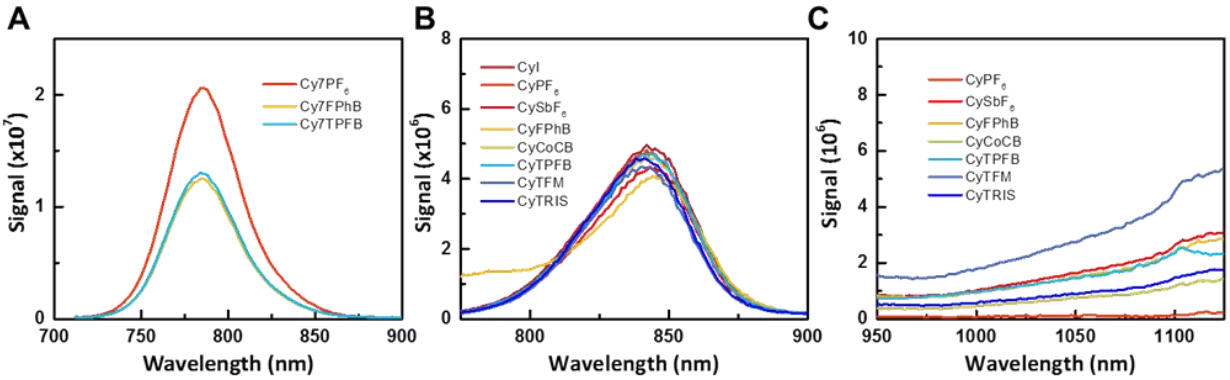

Figure 2.5 Photoluminescence measurements of Cy7X and CyX salts. Absolute scale, background corrected photoluminescence spectra for (**A**) 1 μM Cy7X monomers in DMSO, (**B**) 5 μM CyX monomers in DMSO, and (**C**) 2.5 μM CyX nanoparticles in 1:99 DMSO:H_2O. Due to the peak emission being past 950 nm, quantum yields of the nanoparticles are unmeasurable with our system, but we demonstrate here that the nanoparticles still fluoresce, albeit at different wavelengths than the monomer salts

were formed by diluting these solutions in mixtures of DMSO:H_2O. All of the organic salts formed soluble nanoparticles with this approach, which is expected due to their similar solubilities in water (**Figure 2.2C, Table S2.3**). In aqueous solution, the nanoparticles exhibit distinct peak broadening from the major peak and the minor shoulder. The hypsochromic shift of the 764 nm shoulder peak and a bathochromic shift of the 833 nm peak are indicative of both H- and J-aggregation during the nanoparticle formation process. Nanoparticle organization limits the availability for exchange of the ions and preserves salt composition. These peak shifts are also detectable in live cells,

demonstrating that nanoparticles are uptaken and stable in the cellular environment (**Fig 2.6**). Nanoparticle size of a typical bulky pairing (CyTPFB) was characterized by small-angle X-ray scattering (SAXS): the mean particle size is 4.1 ± 0.6 nm (**Figure 2.7A**), a size that is easily taken up by cells (39). This data was corroborated using scanning electron microscopy (SEM) (**Figure 2.7B**). Additional nanoparticle size

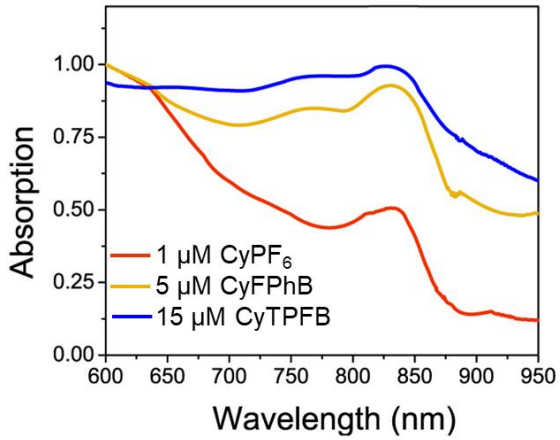

Figure 2.6 UV-vis absorption spectra of A549 cells treated with organic salts. A549 cells were incubated with 1 μM $CyPF_6$, 5 μM CyFPhB, or 15 μM CyTPFB over 24 hours. Following incubation cells were dissociated, washed, and resuspended for UV-Vis analysis. There is a high amount of background due to endogenous fluorophores, but CyFPhB and CyTPFB display peak broadening indicative of nanoparticle formation, having a peak at 830 nm and 764 nm.

distributions were measured using SEM, and all counterion pairings display similar nanoparticle sizes ranging from 5 to 9 nm (**Figures 2.7C-I**). Lifetime experiments confirmed that nanoparticle formation remains stable, with no sign of decomposition into monomers for at least 22 days. The nanoparticles also demonstrated colloidal stability, showing no signs of sedimentation or aggregation over the same period (**Figure 2.8**).

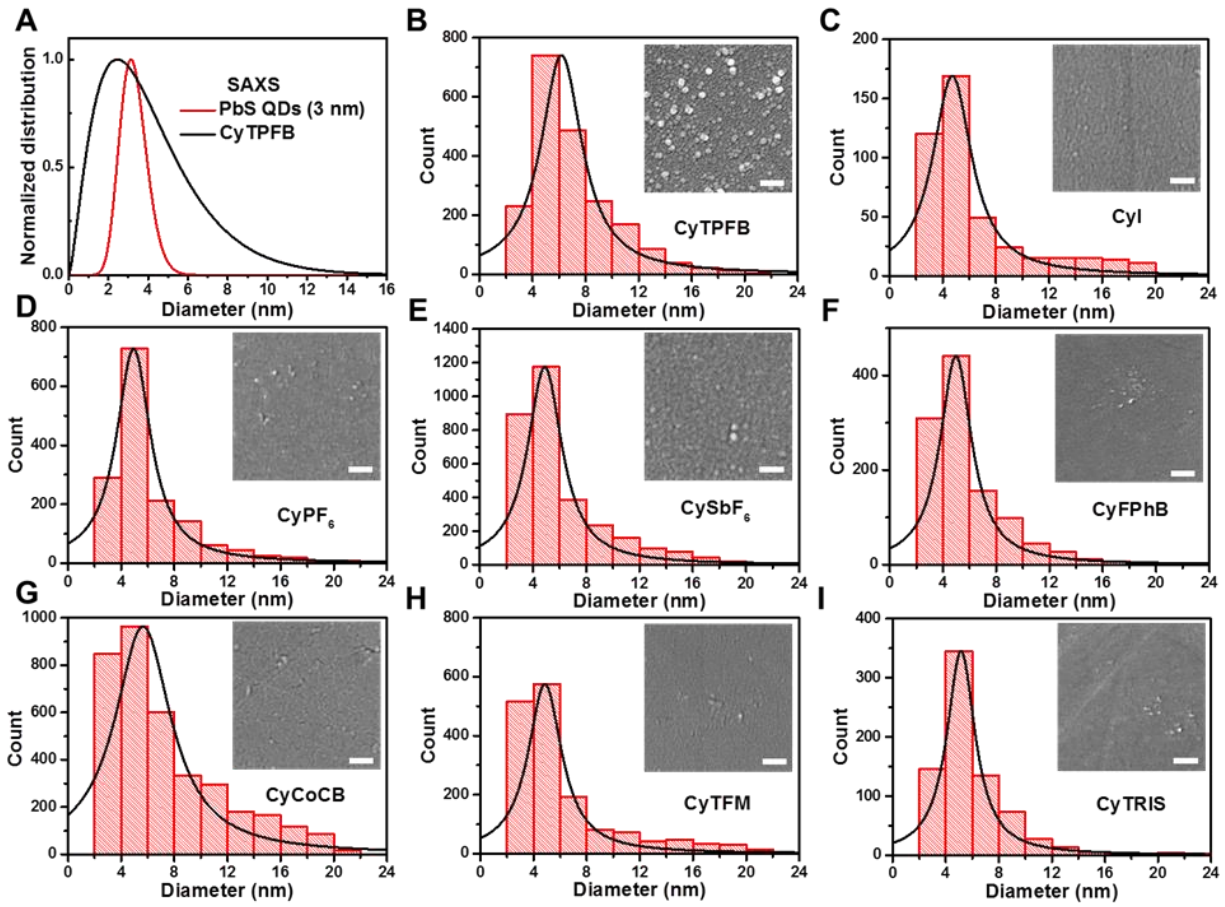

Figure 2.7 Nanoparticle size distribution is similar for all nanoparticles. (**A**) Nanoparticle aggregation size distribution measurements from SAXS measurements of CyTPFB. Mean particle size is 4.1 ± 0.6 nm. PbS quantum dot size distribution is shown as a control with a nominal size of 3 nm. (**B-I**) Nanoparticle size distribution measurements from SEM images (inset, scale bar = 100 nm) of CyX. Mean aggregate size ranges from 5 to 9 nm with no observable precipitation. Other salts were examined with SAXS but did not produce usable data because of solubility limitations. SAXS requires at least 1 mg/mL of the material of interest, and such concentrations are only obtainable with CyTPFB.

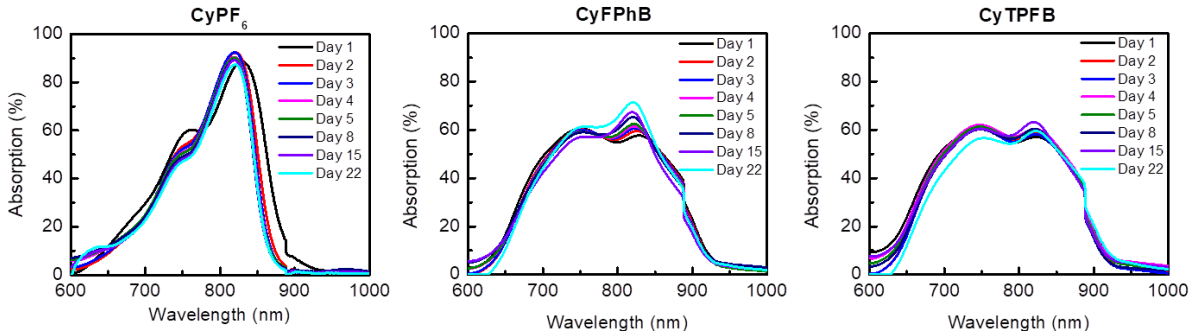

Figure 2.8 Nanoparticle lifetime and stability is demonstrated with CyFPhB and CyTPFB. $CyPF_6$ does not form nanoparticles in cell media but nonetheless demonstrates a stable chromophore. Lifetime absorption (100-%T) data collected with UV-Vis spectroscopy for 5 μM $CyPF_6$, CyFPhB, and CyTPFB in cell media. All three solutions were measured daily for 5 days and again at 8, 15, and 22 days.

2.4.2 Tunable cellular toxicity

Human lung carcinoma (A549) and metastatic human melanoma (WM1158) cell lines were used as representative models of two distinct cancer types with increased expression of OATP1B1 and OATP1B3 (40, 41) but have limited treatment options. Cells were treated with multiple Cy^+-anion pairings by diluting organic salts with cell media to generate self-forming nanoparticles. Cells were incubated with various concentrations of the salt nanoparticles with or without 850 nm light to assess cytotoxicity in the dark and phototoxicity with 850 nm irradiation. Cell viability assays show that Cy^+ is cytotoxic at 1 μM for A549 cells even without exposure to NIR light when paired with small hard anions such as I^-, SbF_6^-, or PF_6^-, and only slightly more phototoxic when exposed to light (**Figure 2.9A**). In contrast, pairings with anions such as $FPhB^-$ and $CoCB^-$ have little cytotoxicity for concentrations below 7.5 μM but are already highly phototoxic at 5.0 μM and 5.5 μM, respectively (**Figure 2.9B**). The combination of low cytotoxicity and high phototoxicity is ideal for photosensitizers in PDT. This starkly contrasts to reports that the anion has no impact on dark cytotoxicity

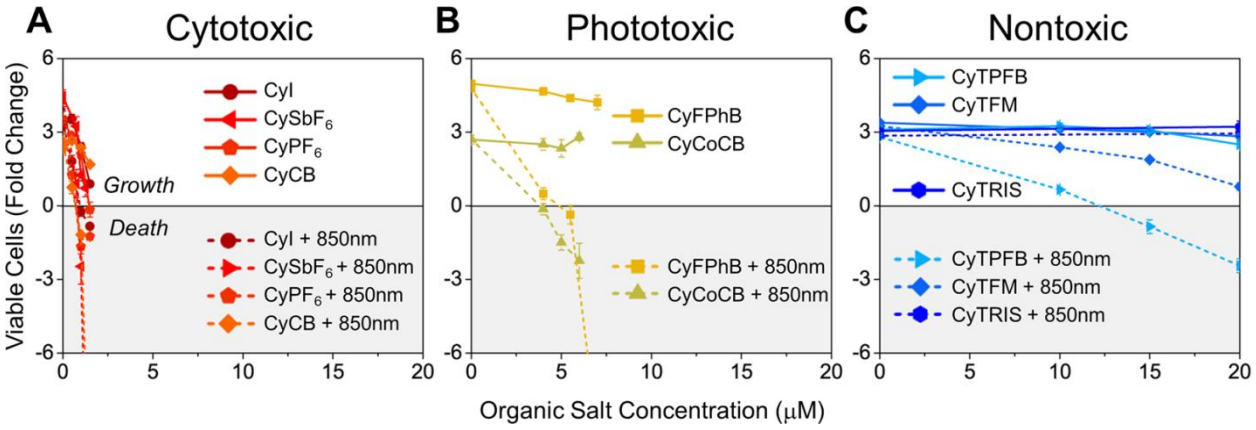

Figure 2.9 Organic salts with tunable toxicity can be used to target human cancer cells. Toxicity of photoactive cation heptamethine cyanine (Cy^+) is tuned with anion pairing. Human lung cancer A549 cells were incubated with various concentrations of Cy^+ with different anionic pairings with or without NIR (850 nm) excitation. Cell viability was determined on day 4 by trypan blue staining and cell counting. (**A**) In A549 cells, CyI, $CySbF_6$, $CyPF_6$, and CyCB (red/orange) are toxic at low concentrations (1 μM), and cell death occurs independent of light excitation (cytotoxic). (**B**) CyFPhB and CyCoCB (yellow/green) do not display significant toxicity without light activation, but when photoexcited they induce significant cell death (phototoxic). (**C**) CyTPFB, CyTFM, and CyTRIS (blue) display lower toxicity with and without light. Data are displayed as means ± S.E.M., $n = 3$.

in breast cancer cells when paired with a larger bandgap fluorophore (20). On the other hand, Cy^+ is found to have reduced cytotoxicity and phototoxicity when paired with $TPFB^-$, TFM^-, and $TRIS^-$. These pairings display negligible cytotoxicity and only modest phototoxicity at much higher concentrations of > 15 μM (TPFB), > 20 μM (TFM), and > 30 μM (TRIS), making them more ideal for *in vivo* imaging applications (**Fig 2.9C**). Both cytotoxicity and phototoxicity are shown to be dose-dependent for all ion pairings tested, with the exception of $TRIS^-$, which displayed no cytotoxicity in the concentrations tested up to 100 μM (**Figure 2.9C**; **Table S2.4**). The dose-dependent response observed in A549 cells is also consistent in WM1158 cells (**Figure 2.10).**

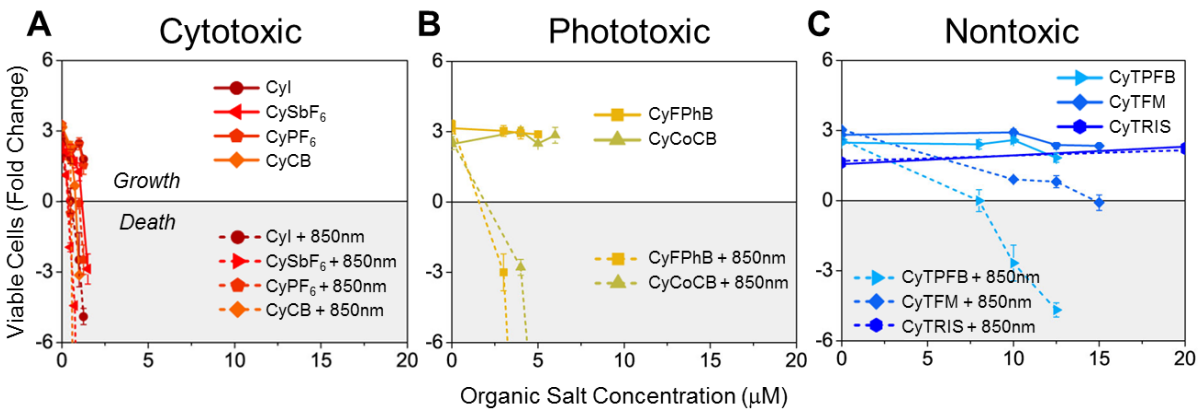

Figure 2.10 Organic salts with tunable toxicity can be used to target metastatic human melanoma cells. Metastatic human melanoma WM1158 cells were incubated with various concentrations of Cy^+ with different anionic pairings with or without NIR (850 nm) excitation for 4 days at which point cell viability was measured by cell count with trypan blue exclusion. (A) CyI, $CySbF_6$, $CyPF_6$, and CyCB (red/orange) are cytotoxic at low concentrations (1μM), with and without NIR excitation (cytotoxic). (B) CyFPhB and CyCoCB (yellow/green) do not display significant toxicity without light activation, but when photoexcited they induce significant cell death (phototoxic). (C) CyTPFB, CyTFM, and CyTRIS (blue) display low toxicity with and without light. This data agrees with the trend observed in A549 cell toxicity. Data are displayed as means ± S.E.M., *n* = 3.

2.4.3 Mechanism of toxicity

To determine the mechanism of the observed tunability in cytotoxicity and phototoxicity, we investigated salt localization within the cell, which can influence the types of ROS generated and their impact on the cell. Colocalization analysis was done in A549 cells incubated with $CyPF_6$ (**Figure 2.11A**) and stained with a DNA stain, Hoechst (Ho; **Figure 2.11B**), and a mitochondrial stain, Rhodamine 123 (Rho123; **Figure 2.11C**). Colocalization was observed for $CyPF_6$ and mitochondrial tracker Rho123, but not with DNA-specific Ho (**Figure 2.11D**). This indicates that the salts preferentially localize in the mitochondria, which is expected due to the charge and hydrophobicity of $CyPF_6$ nanoparticles. Some of the salts that do not colocalize with Rho123 can be observed as red dots on the periphery of the cell. This is likely

endosome accumulation and implicates another potential form of uptake for organic salt nanoparticles besides OATPs, such as endocytosis. Similar results were observed with CyFPhB and CyTPFB **(Figure 2.12**, **Table S2.5**). It should be noted that the limits of resolution with this colocalization method are unable to differentiate nanoparticle localization near the mitochondria, versus localization within the mitochondria, an important point which will be expanded on later in the text.

The mechanism of tunability was further studied by oxidative stress analysis using ROS sensitive probes. MitoSOX was used to measure mitochondrial superoxide

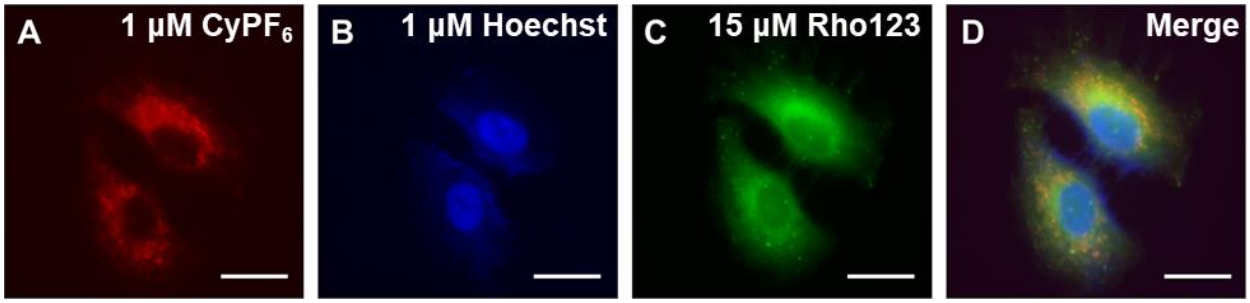

Figure 2.11 $CyPF_6$ preferentially accumulates in the mitochondria and lysosomes of cells. A549 cells were treated with 1 μM $CyPF_6$. (**A**) $CyPF_6$ staining. (**B**) DNA staining using 1 μM 2′-[4-ethoxyphenyl]−5-[4-methyl-1-piperazinyl]−2,5′-bi-1H-benzimidazole trihydrochloride trihydrate (Hoechst). (**C**) Mitochondrial staining using 15 μM Rhodamine 123 (Rho). (**D**) Superimposed $CyPF_6$ + Hoechst + Rho123 staining. Scale bar = 20 μm (100x).

and chloromethyl-2′, 7′-dichlorodihydrofluorescein diacetate (Cm-H_2DCFDA) was used to analyze general cytoplasmic ROS levels in cells treated with phototoxic levels of organic salts with similar levels of intracellular fluorescence (**Figure 2.13**). These organic salt concentrations are also where there are similar levels of fluorescent signal within the cells (**Figure 2.14**). We found that an increase in mitochondrial superoxide is

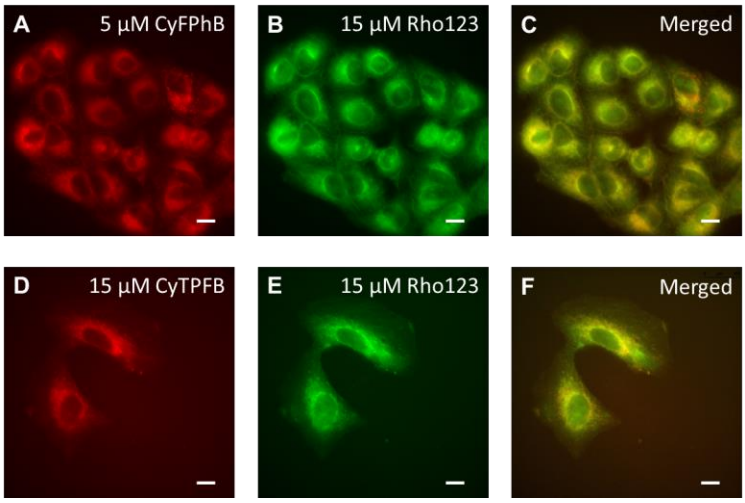

Figure 2.12 Fluorescent organic salts preferentially accumulate in the mitochondria and lysosomes of cells. A549 cells were treated with either 5 µM CyFPhB or 15 µM CyTPFB. (**A**) CyFPhB staining. (**B**) Mitochondrial staining using 15 µM Rhodamine 123 (Rho123). (**C**) Superimposed CyFPhB + Rho123 staining. (**D**) CyTPFB staining. (**E**) Mitochondrial staining using 15 µM Rho123. (**F**) Superimposed CyTPFB + Rho123 staining. Scale bar = 20 µm (40x).

directly correlated with both cytotoxicity and phototoxicity of organic salts. Cytotoxic $CyPF_6$ generates superoxide with or without light; phototoxic (but not cytotoxic) CyFPhB photo-generates superoxide only with illumination; and CyTPFB generates minimal superoxide even with illumination at high concentrations. No significant cytoplasmic ROS was detected using general cytoplasmic ROS probe Cm-H_2DCFDA (**Figure 2.13**).

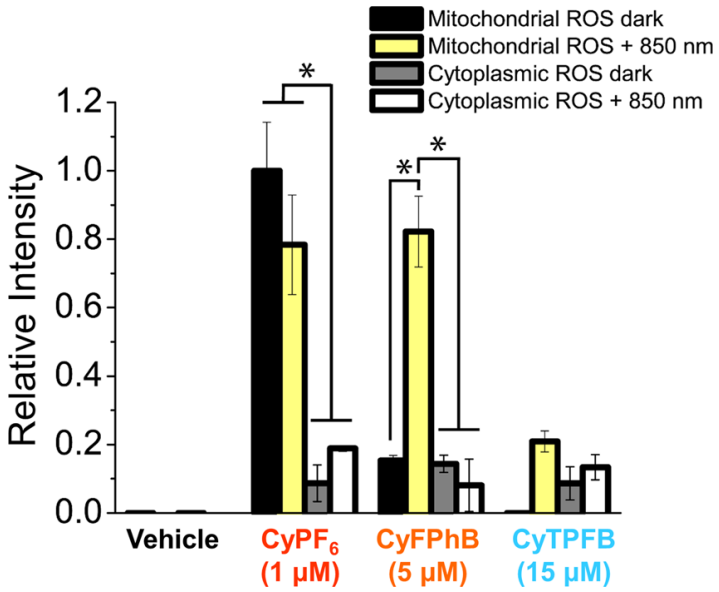

Figure 2.13 Fluorescent organic salts generate mitochondrial superoxide. MitoSOX was used to measure mitochondrial superoxide, and H_2DCFDA for general cytoplasmic ROS in A549 cells treated with organic salts at indicated phototoxic concentrations over 4 days. Phototoxic concentrations were determined from the data in **Figure 2.9**. This data confirms that $CyPF_6$ is cytotoxic, catalyzing superoxide with or without light; CyFPhB is phototoxic but not cytotoxic, photo-generating superoxide only with illumination; and CyTPFB is nontoxic, generating minimal superoxide even with light at high concentrations (*$P \leq 0.05$). Data are displayed as means ± S.D., $n = 3$.

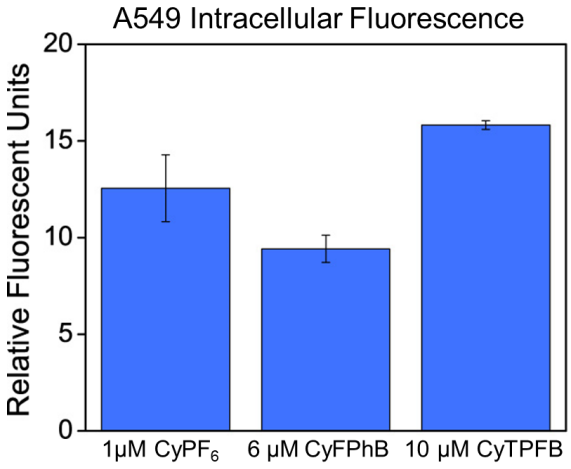

Figure 2.14 Levels of intracellular fluorescence in A549 cells at 24 hours. Concentrations of organic salts used for FCS-ROS studies display similar levels of intracellular fluorescence. Data are displayed as means ± S.D., $n = 3$.

This data demonstrates that the toxicity of organic salts is caused by localized generation of superoxide within the mitochondria. Mitochondrial superoxide is known to mediate apoptosis through oxidative damage of mitochondrial DNA, hyperpolarization of the mitochondrial membrane potential, and protein modifications leading to the opening of the mitochondrial permeability transition pore (42). A key difference in cells treated with $CyPF_6$ is the presence of mitochondrial ROS even without light excitation. This is likely due to the stability of nanoparticles: UV-Vis spectroscopy showed that while pairings with small, hard anions (CyI, $CySbF_6$, and $CyPF_6$,) can form nanoparticles in aqueous solution (**Figure 2.2C**), they do not form nanoparticles in cell media containing fetal bovine serum (**Figure 2.15).** Pairings with bulkier halogenated anion pairings formed stable and soluble nanoparticles even in cell media containing fetal bovine

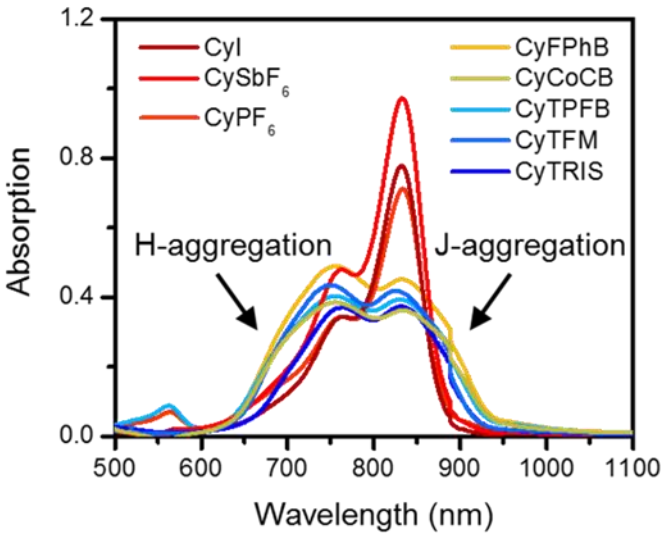

Figure 2.15 Different ion pairings display varying degrees of nanoparticle stability in cell media. Organic salts fully dissolved in DMSO have a clear maximum at 830 nm with a leading shoulder when characterized with UV-Vis spectroscopy. After nanoparticle formation and introduction into cell media, combinations of H- and J-aggregation of organic salts can still be seen by blue-shifted peaks (lower wavelength) and red-shifted peaks (higher wavelength), respectively. This is not observed in smaller anions (I^-, SBF_6^-, PF_6^-), indicating a lack of stability in maintaining nanoparticle formation.

serum. Lack of nanoparticle formation may lead to cytotoxic species, which are toxic even without light activation because they are more likely to interfere with mitochondrial electron transport chain complexes, a process known to generate ROS. In contrast, stable nanoparticles with average sizes of < 20 nm are still able to enter the cell (39), but size limitations likely restrict their ability to directly interact and inhibit protein complexes in the mitochondrial membrane. This difference in localization would not be detectable due to the limits of resolution with traditional colocalization methods.

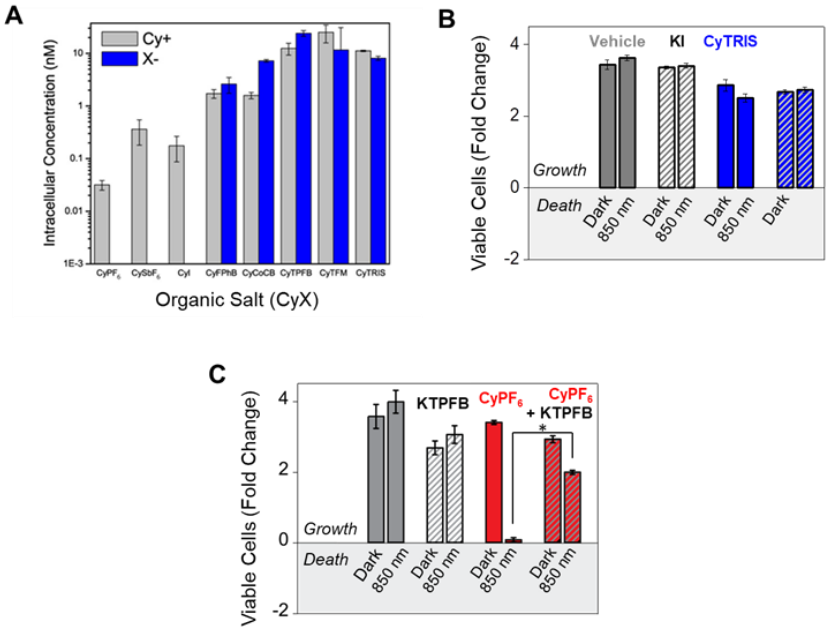

Figure 2.16 Tunability in phototoxicity is not due to cellular accumulation or counterion toxicity. (**A**) Intracellular organic salt accumulation by A549 cells was determined using high-performance liquid chromatography-mass spectrometry. In all cases, cells were incubated with 1 μM of indicated organic salt for 30 hours. Data are displayed as means ± S.D., *n* = 3. (**B**) Iodide (I^-) is not toxic when paired with potassium (K^+), and KI addition does not make CyTRIS toxic. A549 cells were incubated with vehicle, 1 μM KI, 30 μM CyTRIS, or 1 μM KI + 30 μM CyTRIS with or without NIR (850 nm) excitation. Cell viability determined by trypan blue staining and cell counting. (**C**) The phototoxicity and cytotoxicity of $CyPF_6$ can be mitigated by the addition of KTPFB, which is not found to be toxic. A549 cells were incubated with vehicle, 15 μM KTPFB, 1 μM $CyPF_6$, or 15 μM KTPFB + 0.5 μM $CyPF_6$ with or without NIR (850 nm) excitation. Data are displayed as means ± S.E.M., *n* = 3.

To determine whether the counterion affects cellular uptake of organic salts, intracellular levels of different Cy^+-anion pairings were measured by high performance liquid chromatography-mass spectrometry (HPLC-MS). No correlation was observed between toxicity and the intracellular concentration of organic salts (**Figure 2.16A**). This demonstrates that differential anion-mediated uptake is not the cause of the observed modulation in toxicity, even if it is possible that nanoparticle size may be altered upon cellular uptake. In fact, it appears that the opposite may be true: Cy^+ anion pairings with lower cytotoxicity generally had higher intracellular concentrations. However, it should be noted that toxic salts that induce cell death are more likely to rupture and release dyes, potentially decreasing the observed intracellular concentrations.

Furthermore, we find that the anions themselves are not toxic: addition of a phototoxic anion such as I^- paired with a non-fluorescent cation such as potassium (K^+) is neither cytotoxic nor phototoxic (**Figure 2.16B**). Non-cytotoxic anion-cation pairings cannot be made more toxic by addition of toxic anion salts; for example, a less toxic salt (CyTRIS) does not become cytotoxic or phototoxic by addition of a toxic precursor salt (KI; **Figure 2.16B**). However, when the reverse experiment was done and a toxic salt ($CyPF_6$) was supplemented with a nontoxic precursor salt (KTPFB), toxicity was mitigated (**Figure 2.16C**). This is likely due to variance in nanoparticle stability in cellular environments: in cell media, nanoparticles become less stable when Cy^+ is paired with small, hard anions (I^-, SbF_6^-, and PF_6^-), while nanoparticles remain stable when Cy^+ is paired with bulkier halogenated anions ($FPhB^-$, $CoCB^-$, $TPFB^-$, TFM^-, and $TRIS^-$; **Figure 2.15**). Thus, $CyPF_6$ may undergo an energetically favorable anion exchange with KTPFB to generate the less toxic CyTPFB species in cell media, leading to decreased

toxicity and increased cell viability. These data indicate that the toxicity of organic salts is not due to the toxicity of the anion itself, or cellular uptake.

2.4.4 Applications in imaging

We next demonstrated that the concept of counterion-mediated tunability can be used to improve *in vitro* imaging of live cells. Commercially available cyanine molecules used for NIR imaging are typically formulated with halide anions (e.g. chloride or iodide), including the Cy3, Cy5, and Cy7 analogs. We performed anion exchange reactions on Cy7Cl to replace the chloride with the range of anions described above. While Cy7Cl is highly cytotoxic, $Cy7^+$ can be tuned to become less toxic when paired with $TPFB^-$ and $TRIS^-$ (**Figure 2.17A**). This demonstrates that anionic modulation of toxicity is not limited to a specific fluorescent cation, and this effect can be replicated in alternative organic salt formulations. Reduced toxicity is desirable for live cell imaging, as brighter images can be captured with less cellular damage. We have improved live cell imaging using less toxic anion pairing in both Cy^+ and $Cy7^+$. In contrast to the images obtained using toxic $CyPF_6$ and Cy7Cl, brighter images can be captured using less toxic organic salts, such as CyTPFB and Cy7TPFB (**Figure 2.17B-E**). Due to their high toxicity, $CyPF_6$ and Cy7Cl must be used at low concentrations of 1.2 µM and 1.0 µM, respectively. Less toxic CyTPFB and Cy7TPFB can be used at higher doses of 95 µM and 6 µM, respectively, allowing for increased absorption and absolute brightness while preserving cell viability. Thus, enhanced brightness and lack of toxicity lead to improved images that capture representative cells under less cellular stress. Finally, an initial *in*

vivo demonstration of the tumor-targeting ability of fluorescent organic salts is provided:

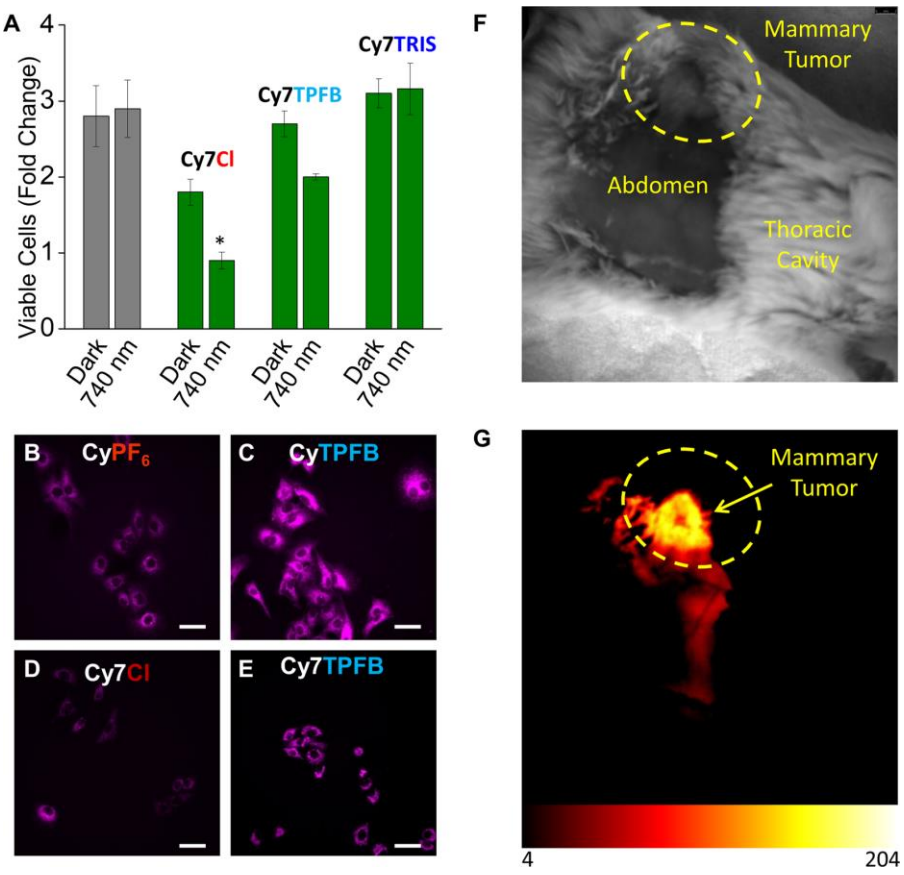

Figure 2.17 Novel and commercial fluorescent dyes can be tuned to be less toxic for brighter imaging. (**A**) Commercially available Cy7, sold as Cy7Cl, can be tuned for toxicity through counterion pairing. A549 cells were incubated with $Cy7^+$ paired with indicated anions at 1 μM. Commercial formulation of Cy7 with Cl^- is found to be cytotoxic; $TPFB^-$ pairing shows a dramatic decrease in cytotoxicity with a minor amount of phototoxicity; $TRIS^-$ pairing eliminates both cytotoxicity and phototoxicity ($^*P \leq 0.05$). Data are displayed as means ± S.E.M., $n = 3$. (**B**) Novel fluorescent cation Cy^+ paired with PF_6^- is cytotoxic at low concentrations (1.2 μM), leading to dim images. (**C**) However, Cy^+ paired with $TPFB^-$ is non-toxic even at increased concentrations (95 μM) and provides brighter images. (**D**) Commercially available Cy7Cl is cytotoxic at 1 μM and provides dim images. (**E**) When Cy7 is paired with counterion $TPFB^-$, it also becomes non-toxic at higher concentrations (6 μM) and provides brighter images. Scale bar = 100 μm (40x). (**F**) Anteroinferior image of supine FVB WT mouse with a MMTV myc-driven mammary tumor. Hair was removed from the abdomen for improved visualization. (**G**) $CyPF_6$ localizes to tumors to enable tumor detection and therapy. Fluorescent images were taken at 41 hours post intraperitoneal injection of 1 mg/kg $CyPF_6$ in PBS. Scale bar represents relative grey value.

intraperitoneally injected $CyPF_6$ preferentially localizes to the tumor in a mouse breast cancer model (**Figure 2.17F-G**).

2.5 Discussion

There is growing interest in developing noninvasive cancer theranostic agents that can detect and target a wide range of tumor types with minimal toxic side effects. This work develops a platform for tuning the toxicity of theranostic agents through counterion pairings for applications in both enhanced imaging and effective therapy. We have demonstrated the ability of weakly coordinating anions to tune cellular toxicity of multiple organic salts by influencing the energy level of the fluorescent cation to impact generation of mitochondrial superoxide. Nanoparticle formation is necessary for the observed modulation of cellular toxicity by the counterion, as it preserves salt composition and prevents ionic dissociation in aqueous solution. However, it should be noted this effect is only feasible due to the poor solubility of the organic salts, which could potentially lead to hurdles such as dosage limitations and poor biostability *in vivo*.

We have shown that the tunability in cellular toxicity is independent of intracellular concentration, anionic toxicity, and is not specific to a particular ionic fluorophore. We do report organic salt localization outside of the mitochondria that may indicate alternative mechanisms and rates of uptake. This could potentially lead to ROS generation at different organelles which would not be measured with MitoSOX, but we do not observe increases in cytoplasmic ROS. There are changes to intracellular fluorescence which could be attributed to changes in uptake, however, this does not explain or correlate to observed differences in the lack of cytotoxicity in the organic salt nanoparticles and why the nanoparticles possess different phototoxicities. There are

limitations to this study imposed by the chemical nature of the nanoparticles. Many assays rely on charged molecules, such as MitoSOX and Rhodamine 123, which can influence the properties of the charged nanoparticles during the assay. Additionally, the small hydrophobic size limits most traditional intracellular imaging techniques. We have attempted to account for this by including orthogonal assays such as mass spectrometry and UV-vis measurements. Additional methods that may allow for improved insight into nanoparticle localization is confocal NIR microscopy, which would allow for improved resolution of cellular organelles, and FRET colocalization.

We do find a correlation between the zeta potential of nanoparticles in aqueous solution and their cyto- and phototoxicity (**Figure 2.18**). Cytotoxic/phototoxic organic salt

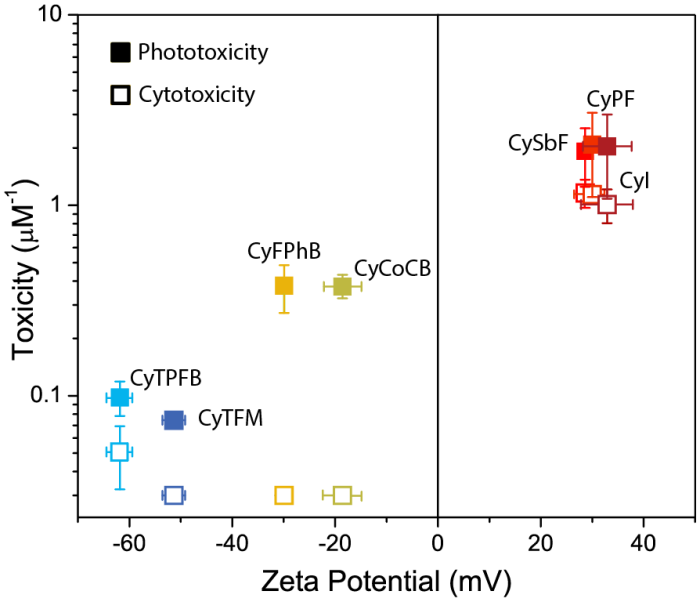

Figure 2.18 Toxicity of organic salts is directly related to changes in zeta potential. Toxicity of cyanine counterion-pairings can be correlated to changes in the electrostatic charge on the nanoparticles as measured by zeta potential. Cytotoxic anion pairings (red) are found to have positive zeta potentials, while non-cytotoxic pairings display negative zeta potentials. Zeta potentials were obtained from **Table S2.1** and toxicity values are the inverse of IC_{50} values obtained from **Table S2.4**. Error displayed as standard deviation.

nanoparticles have positive zeta potentials, while non-cytotoxic/phototoxic nanoparticles have negative zeta potentials, and non-cytotoxic/non-phototoxic nanoparticles have even lower negative zeta potentials (**Table S2.1**). Interestingly, nanoparticles with negative zeta potentials have distinct cyto- and phototoxicities, while nanoparticles with positive zeta potentials have overlapping cyto- and phototoxicities (**Figure 2.18**). Zeta potential has been correlated to HOMO level (38), and these shifts in HOMO are likely the driving force for dictating phototoxicity. While we have demonstrated the correlation between energy level modulation and phototoxicity, the exact mechanism by which valence energy levels effect cellular toxicity remains an open question for future studies. We speculate that the degree of phototoxicity may be dictated by energy level resonance with components in the mitochondria. For example, CyFPhB with a lower absolute HOMO is highly phototoxic, while CyTPFB with a higher absolute HOMO is not phototoxic even at orders of magnitude higher concentrations. This is potentially due to the ability of the photoactivated fluorophore to resonately perform electron transfer reactions within the mitochondria and therefore produce varying amounts and types of particular radical and reactive species. Energy level modulation is only achievable with nanoparticle formulation, as free salts show the same redox potential and therefore the same energy level (**Figure 2.4**) (29). Low toxicity pairings with anions such as $TPFB^-$ and TFM^- can be used to reduce cellular toxicity during diagnostic imaging. In contrast, we have selectively enhanced phototoxicity in response to NIR excitation while eliminating dark cytotoxicity of Cy^+ across a range of cell lines by pairings with anions such as $FPhB^-$ and $CoCB^-$. This approach has the potential to increase targeting efficacy in tumors while minimizing nonspecific toxicity in healthy tissue. While In

addition to having broad clinical applications, this work gives insight into a novel method for modulating the electronic characteristics of fluorescent cation-anion pairings and provides a rational strategy for enhancing existing photodynamic drugs and imagers.

2.6 Methods

2.6.1 Synthesis

Synthesis of $CyPF_6$, $CySbF_6$, CyFPhB, and CyTPFB: Precursor salts (CyI and $NaPF_6$, $NaSbF_6$, NaFPhB, or KTPFB) were dissolved in methanol:dichloromethane (MeOH:DCM) mixtures and stirred at room temperature under nitrogen. The counterion precursor was added in 100% molar excess to drive the exchange of ions. The product compounds were formed as solid precipitates after approximately 5 minutes. They were collected using vacuum filtration and rinsed with MeOH. The crude product was dissolved in minimal DCM and run through a silica gel plug with DCM as the eluent to remove unreacted precursors and other impurities. The product compound exiting the silica was recognized by its color and collected. Excess DCM was removed in a rotary evaporator. Reaction yield and purity were confirmed using a high mass accuracy time-of-flight mass spectrometer coupled to an ultra-high performance liquid chromatography (UPLC-MS) in positive mode to quantify cations, and in negative mode to quantify anions. For ion purity measurements, solutions of precursors and products were prepared in various known concentrations and analyzed by UPLC-MS. Typical reactions led to products yields of > 60% with purities > 95%. Reaction schemes and purification procedures described previously were used (30, 43).

Synthesis of CyTRIS and CyTFM: Precursor salts (CyI and TBA-TRIS or NaTFM) were dissolved in DCM in a 1:2 molar ratio and stirred at room temperature under nitrogen for 1 hour. The reaction contents were passed through a silica gel plug using DCM as the eluent, where the purified product was collected and quantified with UPLC-MS as described for the salts above. Similar yields and purities were achieved for CyTRIS and CyTFM as other salts.

Synthesis of CyCoCB: Precursor salts CyI and NaCoCB were dissolved in MeOH in a 1:2 molar ratio and stirred at room temperature under nitrogen. CyCoCB formed and precipitated out of solution after approximately 5 minutes. The crude product was collected using vacuum filtration and rinsed with MeOH. It was then purified with silica gel chromatography and the purity was quantified with UPLC-MS as detailed previously. Reaction yield and purity of CyCoCB was similar to that of the other salts discussed here (30, 31).

Synthesis of Cy7PF_6, Cy7FPhB, Cy7TPFB, and Cy7TRIS: Precursor salts (Cy7Cl and $NaPF_6$, NaFPhB, KTPFB, and TBA-TRIS) were dissolved in DCM in a 1:2 molar ratio and stirred at room temperature under nitrogen for 1 hour. Reaction contents were passed through a silica gel plug using DCM as the eluent, where the purified product was collected and quantified with UPLC-MS. Reaction yields were 45-50% with similar purity to other salts discussed here.

Cyanine7 NHS ester (Cy7) was utilized as received (Lumiprobe), as a commercial reference.

2.6.2 Cell culture

Human lung carcinoma (A549) and metastatic human melanoma (WM1158) cells were cultured in Dulbecco's Modified Eagle's Medium (DMEM) with 4.5 g/L glucose without sodium pyruvate with 10% heat inactivated fetal bovine serum supplemented with 1 mM glutamine and 1% penicillin and streptomycin. Cells were incubated in 37°C with 5% CO_2 without light exposure.

2.6.3 Viability studies

A549 and WM1158 cells were seeded at a density of 50,000 cells per well in 6-well tissue culture plates. After 24 hours of incubation, media was aspirated and replaced with media containing fluorescent dyes at indicated concentrations. Each well was irradiated with an 850 nm LED lamp with an illumination flux of 526 mW/cm^2 for an hour in the incubator, and control cells were left in a dark incubator without irradiation. For studies using Cy7, a custom made 740 nm LED lamp was used, but with the same illumination flux. Immediately after irradiation, the media was replenished with fresh dye-laced media and allowed to incubate for another 24 hours. The same procedure was done at 48 and 72 hours, but the cells received no further dye-laced media after 72 hours. Viable cell number was determined at 24 and 96 hours using 4% trypan blue and a Nexcelom Cellometer Auto T4 cell counter. All assays were done with 3 biological replicates. The fold change in cell proliferation over days of treatment was calculated using the following equation (44):

$$Fold\ change = \log_2 \frac{Day\ 4\ viable\ cell\ count}{Day\ 1\ viable\ cell\ count}$$

The half maximal inhibitory concentration (IC_{50}) was calculated by linear regression analysis of cell viability versus concentration data.

2.6.4 Fluorescent imaging

Images were obtained using a Leica DMi8 microscope with a PE4000 LED light source, DFC9000GT camera, and LAS X imaging software. A549 cells were seeded in 3 cm tissue culture plates at a density of 50,000 cells per well in DMEM containing fluorescent organic salts at indicated concentrations. The cells were incubated for 2 days at 37°C with 5% CO_2 until the day of imaging. For live cell imaging, the media was aspirated, and the cells were washed with phosphate buffered saline (PBS, Sigma-Aldrich) 5 times before being imaged in PBS.

For colocalization analysis, A549 cells were grown on 0.5 mm coverslips placed in 3 cm tissue culture plates containing media for 3 days. Cells were then fixed by aspirating media, washing with PBS 5 times, then submerging the coverslip in cold methanol and incubating on ice for 15 minutes. The fixed cells were stained with 1 µM 2'-[4-ethoxyphenyl]-5-[4-methyl-1-piperazinyl]-2,5'-bi-1H-benzimidazole trihydrochloride trihydrate (Hoechst 33342, Invitrogen) for 5 minutes, washed with PBS, and then incubated with 15 µM of 3,6-diamino-9-(2-(methoxycarbonyl)phenyl chloride (Rhodamine123) and 1 µM $CyPF_6$ for 15 minutes before being washed and mounted to slides with Fluoromount-G (Invitrogen). Cells were analyzed using a Leica DMi8 microscope with a PE4000 LED light source, DFC9000GT camera, and LAS X imaging software.

2.6.5 Flow cytometry

Cells were incubated with phototoxic concentrations of $CyPF_6$ (1 μM), CyFPhB (5 μM), or CyTPFB (15 μM) and exposed to NIR light for 4 days as described above. Each day, cells were collected for analysis by trypsinization from plates (prior to any illumination), spun down and resuspended in a staining buffer consisting of Hank's buffered salt solution (HBSS, Sigma-Aldrich) with 10 mM 4-(2-Hydroxyethyl)piperazine-1-ethanesulfonic acid (HEPES, Sigma-Aldrich) and 2% FBS. Cells were separated into 2 populations for staining with 15 μM of chloromethyl-2′, 7′-dichlorodihydrofluorescein diacetate (cm- H_2DCFDA, Invitrogen) for 60 minutes, or 2.25 μM of MitoSOX (Invitrogen) for 20 minutes. Hydrogen peroxide was used as a positive control for H_2DCFDA. Cells were analyzed on a BD LSR II using FITC and PE-A channels and 30,000 events counted. Fluorescence was normalized to the initial value.

2.6.6 Ultraviolet visible spectroscopy

Cyanine dyes were diluted to a concentration of 5 μM in cell media. All dyes were characterized using a Perkin-Elmer 25 UV-Vis spectrometer in the wavelength range from 500-1100 nm in normal incidence transmission mode with a resolution of 1 nm and a 1.27 cm path length. A pure solvent reference was utilized to remove reflections so that the absorption is calculated as 1-transmission. For intracellular characterization, A549 cells were incubated with DMSO, 1 μM $CyPF_6$, 5 μM CyFPhB, or 15 μM CyTPFB for 24 hours. Cells were dissociated from plates with 0.05% trypsin, washed with PBS, spun down, and resuspended in HBSS with 10 mM HEPES and 2% FBS. Cell suspensions gently mixed prior to characterized using the same parameters described above. DMSO treated cell samples were used as the solvent reference.

2.6.7 Zeta potential measurements of nanoparticles

A Zetasizer Nano Z (Malvern Instruments, UK) at 25°C with a 633 nm laser was used to calculate zeta-potential measurements (ζ) using laser Doppler micro-electrophoresis. Measured electrophoretic mobilities (μ_e) were converted to zeta potentials from the Henry equation:

$$\zeta = \frac{\mu_e 3\eta}{2\varepsilon_\tau \varepsilon_0 f(Ka)}$$

where ε_τ is the dielectric constant of the medium, ε_0 is the permittivity of the vacuum, $f(Ka)$ is Henry's function, and η is the viscosity of the colloid. Samples were run in triplicate at a concentration of 10 µM in 10% phosphate buffered saline and 1% DMSO.

2.6.8 Scanning electron microscopy

Polished glass substrates (Xin Yan Technology LTD) for SEM imaging were cleaned by sonicating in soap, deionized water, acetone, and by boiling in isopropanol for 6 minutes each, followed by oxygen plasma treatment for 3 minutes. Nanoparticles of CyX were spin-coated with 50 µL of 0.5 µM solutions on a glass substrate at 2000 rpm for 30 seconds. A thin film of platinum was deposited on the SEM samples to reduce charging. A Carl Zeiss EVO LS 25 Variable Pressure Scanning Electron Microscope and a Tescan Mira3 Scanning Electron Microscope were used to capture SEM images of organic salt nanoparticles. Size distributions were obtained using ImageJ software (45).

2.6.9 Small-angle x-ray scattering

Small-angle X-ray scattering (SAXS) was performed with a Rigaku Ultima IV X-ray Diffractometer in the Robert B. Mitchell Electron Microbeam Analysis Lab at the University of Michigan. Parallel beam and SAXS alignment procedures were performed to prepare the diffractometer for measurements. Boron-rich glass capillaries with 1.5 mm outside diameter were purchased from the Charles Supper Company for these measurements. A control sample of 2 mg/mL PbS quantum dots (Millipore Sigma, 3 nm nominal size) in toluene was run first to verify measurement accuracy, producing a mean particle size of 3.3 ± 0.2 nm after subtracting a toluene background scan. A sample of 2.6 mg/mL CyTPFB nanoparticles in 50% DMSO, 50% water was tested, along with a 50% DMSO, 50% water blank, and produced a size distribution curve shown in **Figure 2.7** with a mean particle size of 4.1 ± 0.6 nm. Solubility limits prevented collection of SAXS data for the other CyX nanoparticles, as high concentrations of > 1 mg/mL were necessary to obtain data above the background (see **Table S2.3**).

2.6.10 Differential pulse voltammetry

Differential pulse voltammetry measurements were made using a μAutoLabIII potentiostat to evaluate oxidation potentials for monomer and nanoparticle salts. For monomers, salts were dissolved at 1 mM in acetonitrile with 100 mM TBA-PF_6 as a supporting electrolyte. Glassy carbon, Ag/$AgNO_3$ (0.36 V vs SCE), and Pt mesh were used as the working, reference, and counter electrodes, respectively. Nanoparticles of the salts were made at 0.1 mM in 10% DMSO (CyI, $CyPF_6$) and 50% DMSO (CyFPhB) in H_2O with 100 mM NaCl as a supporting electrolyte. CyTPFB NPs have greater solubility and were tested at 0.5 mM in 50% DMSO. Ag/AgCl reference electrode (-45

mV vs SCE) was used for the nanoparticle measurements. Nanoparticle solubility limitations in acetonitrile limited collection of CV scans to CyI, $CyPF_6$, CyFPhB and CyTPFB, for which concentrations of at least 0.1 mM were achievable.

2.6.11 Photoluminescence

Photoluminescence (PL) spectra were collected using a PTI Spectrofluorometer for monomers of Cy7X and CyX salts, as well as nanoparticles of CyX salts. For Cy7X monomers, solutions at 1 µM salt in DMSO were used. Solutions of 5 µM CyX salts were prepared in DMSO for PL measurements. Nanoparticles of CyX salts were made at 2.5 µM in 1% DMSO, 99% water. A mounted Thorlabs 735 nm LED was used at approximately 5% power as the excitation source for the PL spectra of the CyX monomers and nanoparticles, while a monochromated Xenon lamp (700 nm) was used as the excitation source for Cy7X PL.

2.6.12 Quantum yield

Quantum yield (QY) data was gathered using a PTI Spectrofluorometer with an integrating sphere (350-900 nm) for monomers of Cy7X and CyX salts. A Thorlabs 735 nm LED was used at approximately 5% power as the excitation source for all quantum yield measurements. Cy7X solutions were made at 1 µM in DMSO, while CyX salts were prepared at 2.5 µM in DMSO.

2.6.13 Determination of intracellular organic salt concentrations

Cells were seeded at a density of 50,000 cells per well in 6-well plates in media containing 1 µM of indicated dye. Cells were allowed to incubate for 3 days at 37°C with 5% CO_2 with a media change to fresh dye-laced media on day 2. For extraction, media

was aspirated from each well, and cells were washed with PBS. The cells were removed from the plate using 0.05% trypsin/EDTA (Thermo Fisher) and centrifuged at 1,500 rpm for 6 minutes. The supernatant was aspirated, and the cell pellet was washed with saline. Saline was aspirated, and the pellets were resuspended with room temperature HPLC-grade 3:7 methanol:acetonitrile (Sigma Aldrich) and centrifuged at 13,000 rpm for 5 minutes. The supernatant was collected in a separate tube, and the pellet was again resuspended in HPLC grade 3:7 methanol:acetonitrile and centrifuged at 13,000 rpm for 10 minutes. The supernatant was combined with the first supernatant for analysis by liquid chromatography-mass spectrometry.

Cell extracts were analyzed the day of extraction using a Waters Xevo G2-XS QToF mass spectrometer coupled to a Waters Acquity UPLC system. The UPLC parameters were as follows: autosampler temperature, 10ºC; injection volume, 5 µl; column temperature, 50°C; and flow rate, 300 µl/min. The mobile solvents were Solvent A: 10mM ammonium formate (Sigma-Aldrich) and 0.1% formic acid (Sigma-Aldrich) in 60:40 acetonitrile:water; and Solvent B: 10mM ammonium formate and 0.1% formic acid in 90:10 isopropanol:acetonitrile. Elution from the column was performed over 5 minutes with the following gradient: t = 0 minutes, 5% B; t = 3 minutes, 95% B; t = 4 minutes, 95% B; t = 5 minutes, 5% B. ESI spray voltage was 3,000 V. Nitrogen was used as the sheath gas at 30 psi and as the auxiliary gas at 10 psi, and argon as the collision gas at 1.5 mTorr, with the capillary temperature at 325ºC. Data were acquired and analyzed using MassLynx 4.1 and QuanLynx software. Cy^+, which typically elutes at 2.5 minutes, was analyzed in positive mode. Standards of each anion-cation pair were run at

concentrations of 5, 10, 25, 50, and 100 nM to generate standard curves for quantitation. Blanks were run before each sample to minimize sample carryover.

2.6.14 *In vivo* imaging

All animal protocols were approved and performed in accordance with guidelines set by the Institute of Animal Care and Use Committee (IACUC) of Michigan State University. Primary MMTV-Myc papillary tumors were donated by Dr. Eran Andrechek and have been previously described (46). Viable frozen tumor chunks (1 mm^3) were implanted into the right fourth mammary fat pad of FVB/NJ female mice (purchased from Jackson Laboratories, Bar Harbor, ME, USA) at 6-8 weeks of age. Tumors were monitored with calipers twice a week. Once tumors reached 7.5 mm by the longest axis, mice were given a 1 mg/kg intraperitoneal injection of $CyPF_6$ in 200 µL of sterile PBS and 1% DMSO. Mice were anesthetized with 3% isoflurane and fluorescent images were taken at 41 hours post injection using a Leica M165FC stereoscope with a 740 nm PE4000 LED light source, DFC9000GT camera, and LAS X imaging software.

2.6.15 Statistical analysis

Statistical analysis was done using OriginPro 8 software. For analyses with more than two group comparisons, a one-way ANOVA analysis was performed with an ad hoc Bonferroni test. To assess the homogeneity of variance and suitability for ANOVA analysis, a Levene's test was performed. *P*-values < 0.05 are reported as statistically significant.

2.7 Acknowledgments

The authors thank Elliot Ensink, Martin Ogrodzinski, Shao Thing Teoh, and Lei Yu for helpful discussions and critical reading of this manuscript. The authors thank Eran Andrechek for the primary MMTV-Myc papillary tumors. The authors also thank the Michigan State University (MSU) Flow Cytometry Core and the MSU Mass Spectrometry and Metabolomics Core. The authors thank the University of Michigan Robert B. Mitchell Electron Microbeam Analysis Lab. Funding: This material is based upon work supported by the National Science Foundation under CAREER Grant No. (CBET 1845006) to S.Y.L. and a MSU Strategic Partnership Grant. M.B. and R.R.L. were supported by the National Science Foundation under Grant No. (CBET 1702591).

2.8 Author Contributions

S.Y.L. and R.R.L. conceived the project. D.B., M.B., M.Y, R.R.L, and S.Y.L. designed the experiments. D.B. performed all cell toxicity assays as well as mass spectrometry, cell imaging, and flow cytometry experiments. M.B. collected optical and characterization data of the nanoparticles. M.J. assisted with cell toxicity assays. M.B. and M.Y. synthesized the organic salts and nanoparticles. J.H. and W.Z. assisted with zeta potential measurements. A.R. and T.H. assisted with differential pulse voltammetry measurements. B.B. assisted with chemical synthesis. D.B., M.B., R.R.L, and S.Y.L. wrote the manuscript.

APPENDIX

Salt	Zeta potential (mV)
CyI	32.87 ± 5.03
$CyPF_6$	30.00 ± 2.13
$CySbF_6$	27.97 ± 0.55
CyFPhB	-29.93 ± 0.95
CyCoCB	-18.53 ± 3.63
CyTPFB	-61.87 ± 1.66
CyTFM	-51.37 ± 2.19
CyTRIS	-32.40 ± 1.93

Table S2.1 Zeta potential changes as a function of counterion pairing. Zeta potential of organic salt nanoparticles was calculated from electrophoretic mobility using a Malvern Zetasizer NS. The anion shifts the zeta potential, similar to what is observed in the solid-state using UPS (**Figure 2.1B**).

Salt	Quantum yield (%)
$Cy7PF_6$	26
Cy7FPhB	26
Cy7TPFB	23
Cy7TRIS	24
CyI	1.7
$CyPF_6$	2.7
$CySbF_6$	1.7
CyFPhB	1.9
CyCoCB	1.4
CyTPFB	2.5
CyTFM	1.4
CyTRIS	1.9

Table S2.2 Quantum yields for CyX and Cy7X salts. The quantum yields of the monomer salts do not change significantly with the counterion. Quantum yield data for the nanoparticles is unobtainable with our system due to the emission range of the nanoparticles and the detection limits of our system in the near-infrared region.

Salt	Solubility in Water (mg/mL)	Nanoparticle solubility in 50:50 DMSO:H_2O (mg/mL)
CyI	7 × 10-5	-
$CyPF_6$	5 × 10-5	-
CyFPhB	2 × 10-5	0.1
CyCoCB	2 × 10-5	0.05
CyTPFB	7 × 10-5	2.5
CyTFM	1 × 10-4	0.05

Table S2.3 CyX salts display similar solubilities in water. The water solubility of monomer cyanines is not significantly affected by counterion pairing. SAXS measurements have been limited to CyTPFB as the only nanoparticle with high enough solubility in 50:50 DMSO:Water. Small anions such as I^- and PF_6^- do not form nanoparticles at more than 25% DMSO.

Salt	IC_{50} Dark (μM)	95% CI	IC_{50} 850nm (μM)	95% CI
CyI	1	0.8-1.3	0.5	0.2-0.7
$CyPF_6$	0.9	0.8-1.0	0.5	0.2-0.7
$CySbF_6$	0.9	0.7-1.0	0.5	0.3-0.7
CyCB	1.8	1.4-2.6	0.5	0.2-0.7
CyFPhB	> 20[a]	NA	2.6	1.7-3.4
CyCoCB	> 20[a]	NA	2.7	2.2-3.0
CyTPFB	19.7	15.1-31.3	10.2	7.9-12.8
CyTFM	NA	NA	13.5	11.9-15.2
CyTRIS	NA	NA	NA	NA

Table S2.4 Toxicity of photoactive cation heptamethine cyanine (Cy^+) is determined by counterion pairing. The half maximal inhibitory concentration (IC_{50}) values were generated by linear regression analysis for A549 cells. The error is displayed as a 95% confidence interval. [a]CyCoCB and CyFPhB Dark IC_{50} values were extrapolated from observed values. NA - values could not be calculated from experimental trends.

	$CyPF_6$	CyFPhB	CyTPFB
Pearson's Coefficient	0.852	0.853	0.901
Mander's Coefficient 1	0.991	0.997	0.967
Mander's Coefficient 2	0.971	0.992	0.983

Table S2.5. Intracellular localization of the fluorescent ion in A549 cells does not change with the counterion. Variables of colocalization that measure the linear relationship between red (organic salt analog) and green (Rhodamine123) fluorescence (Pearson's coefficient), overlap of red to green area (Mander's coefficient 1), and overlap of green to red area (Mander's coefficient 2). All organic salts show a positive linear correlation with mitochondrial fluorescence, with similar degrees of colocalization in the mitochondria.

REFERENCES

REFERENCES

1. Dougherty TJ, Gomer CJ, Henderson BW, Jori G, Kessel D, et al. 1998. Photodynamic Therapy. *JNCI: Journal of the National Cancer Institute*. 90:889–905

2. Mojzisova H, Bonneau S, Brault D. 2007. Structural and physico-chemical determinants of the interactions of macrocyclic photosensitizers with cells. *European Biophysics Journal*. 36:943–53

3. Wilson BC. 2002. Photodynamic therapy for cancer: principles. *Can J Gastroenterol*. 16:393–96

4. Chance B. 1998. Near-Infrared Images Using Continuous, Phase-Modulated, and Pulsed Light with Quantitation of Blood and Blood Oxygenationa. *Annals of the New York Academy of Sciences*. 838:29–45

5. Henderson TA, Morries LD. 2015. Near-infrared photonic energy penetration: can infrared phototherapy effectively reach the human brain? *Neuropsychiatr Dis Treat*. 11:2191–2208

6. Kolenc OI, Quinn KP. 2018. Evaluating Cell Metabolism Through Autofluorescence Imaging of NAD(P)H and FAD. *Antioxid. Redox Signal.*

7. Patel NJ, Chen Y, Joshi P, Pera P, Baumann H, et al. 2016. Effect of Metalation on Porphyrin-Based Bifunctional Agents in Tumor Imaging and Photodynamic Therapy. *Bioconjugate Chemistry*. 27:667–80

8. Frangioni JV. 2003. In vivo near-infrared fluorescence imaging. *Current Opinion in Chemical Biology*. 7:626–34

9. Vahrmeijer AL, Hutteman M, van der Vorst JR, van de Velde CJH, Frangioni JV. 2013. Image-guided cancer surgery using near-infrared fluorescence. *Nat Rev Clin Oncol*. 10:507–18

10. Tan X, Luo S, Wang D, Su Y, Cheng T, Shi C. 2012. A NIR heptamethine dye with intrinsic cancer targeting, imaging and photosensitizing properties. *Biomaterials*. 33:2230–39

11. Shen T. 2016. Efficient Tumor Accumulation, Penetration and Tumor Growth Inhibition by Polymer Therapeutics: The Effect of Polymer Architectures. *Biomacromolecules*, p. 13

12. Sui B, Zhong G, Sun J. 2016. Drug-loadable Mesoporous Bioactive Glass Nanospheres: Biodistribution, Clearance, BRL Cellular Location and Systemic Risk Assessment via 45Ca Labelling and Histological Analysis. . 6:33443

13. Yuan L, Lin W, Zheng K, He L, Huang W. 2013. Far-red to near infrared analyte-responsive fluorescent probes based on organic fluorophore platforms for fluorescence imaging. *Chemical Society Reviews*. 42:622–61

14. Benov L. 2015. Photodynamic Therapy: Current Status and Future Directions. *Medical Principles and Practice*. 24(suppl 1):14–28

15. Wiedmann TS, Naqwi A. 2016. Pharmaceutical salts: Theory, use in solid dosage forms and in situ preparation in an aerosol. *Asian Journal of Pharmaceutical Sciences*. 11(6):722–34

16. Kilin V. 2014. Counterion-enhanced cyanine dye loading into lipid nano-droplets for single-particle tracking in zebrafish. *Biomaterials*. 35:7

17. Shulov I. 2016. Non-coordinating anions assemble cyanine amphiphiles into ultra-small fluorescent nanoparticles. *Chem. Commun.*, p. 4

18. Reisch A. 2014. Collective fluoresecense switching of counter-ion assumbled dyes in polymer nanoparticles. *Nature Communications*

19. Shulov I. 2015. Fluorinated counterion-enhanced emission of rhodamine aggregates: ultrabright nanoparticles for bioimaging and light-harvesting. *Nanoscale*

20. Magut PKS, Das S, Fernand VE, Losso J, McDonough K, et al. 2013. Tunable Cytotoxicity of Rhodamine 6G via Anion Variations. *J. Am. Chem. Soc.* 135(42):15873–79

21. Siraj N, Kolic PE, Regmi BP, Warner IM. Strategy for Tuning the Photophysical Properties of Photosensitizers for Use in Photodynamic Therapy. *Chemistry – A European Journal*. 21(41):14440–46

22. Yang X, Shi C, Tong R, Qian WP, Zhau HE, et al. 2010. Near Infrared Heptamethine Cyanine Dye-Mediated Cancer Imaging. *Clinical Cancer Research*

23. Wang Y, Liu T, Zhang E, Luo S, Tan X, Shi C. 2014. Preferential accumulation of the near infrared heptamethine dye IR-780 in the mitochondria of drug-resistant lung cancer cells. *Biomaterials*. 35:4116–24

24. Changhong Shi JBW. 2016. Review on near-infrared heptamethine cyanine dyes as theranostic agents for tumor imaging, targeting, and photodynamic therapy. *J. Biomed. Opt.* 21:

25. Wu JB, Shao C, Li X, Shi C, Li Q, et al. 2014. Near-infrared fluorescence imaging of cancer mediated by tumor hypoxia and HIF1α/OATPs signaling axis. *Biomaterials*. 35(28):8175–85

26. Wu SP, Lee I, Ghoroghchian PP, Frail PR, Zheng G, et al. 2005. Near-Infrared Optical Imaging of B16 Melanoma Cells via Low-Density Lipoprotein-Mediated Uptake and Delivery of High Emission Dipole Strength Tris[(porphinato)zinc(II)] Fluorophores. *Bioconjugate Chem.* 16(3):542–50

27. Garcia-Diaz M, Huang YY, Hamblin MR. 2016. Use of fluorescent probes for ROS to tease apart Type I and Type II photochemical pathways in photodynamic therapy. *Methods*. 109:158–66

28. Zhang C, Zhao Y, Zhang H, Chen X, Zhao N, et al. 2017. The Application of Heptamethine Cyanine Dye DZ-1 and Indocyanine Green for Imaging and Targeting in Xenograft Models of Hepatocellular Carcinoma. *International Journal of Molecular Sciences*. 18(6):1332

29. Suddard-Bangsund J, Traverse CJ, Young M, Patrick TJ, Zhao Y, Lunt RR. 2016. Organic Salts as a Route to Energy Level Control in Low Bandgap, High Open-Circuit Voltage Organic and Transparent Solar Cells that Approach the Excitonic Voltage Limit. *Advanced Energy Materials*. 6:1501659-n/a

30. Young M, Suddard-Bangsund J, Patrick TJ, Pajares N, Traverse CJ, et al. 2016. Organic Heptamethine Salts for Photovoltaics and Detectors with Near-Infrared Photoresponse up to 1600 nm. *Advanced Optical Materials*. 4:1028–33

31. Traverse CJ, Young M, Suddard-Bangsund J, Patrick T, Bates M, et al. 2017. Anions for Near-Infrared Selective Organic Salt Photovoltaics. *Scientific Reports*. 7(1):16399

32. Dang X, Gu L, Qi J, Correa S, Zhang G, et al. 2016. Layer-by-layer assembled fluorescent probes in the second near-infrared window for systemic delivery and detection of ovarian cancer. *Proceedings of the National Academy of Sciences*. 113:5179–84

33. Ge J, Jia Q, Liu W, Lan M, Zhou B, et al. 2016. Carbon Dots with Intrinsic Theranostic Properties for Bioimaging, Red-Light-Triggered Photodynamic/Photothermal Simultaneous Therapy In Vitro and In Vivo. *Advanced Healthcare Materials*. 5:665–75

34. Burns AA, Vider J, Ow H, Herz E, Penate-Medina O, et al. 2009. Fluorescent Silica Nanoparticles with Efficient Urinary Excretion for Nanomedicine. *Nano Letters*. 9:442–48

35. Phillips E, Penate-Medina O, Zanzonico PB, Carvajal RD, Mohan P, et al. 2014. Clinical translation of an ultrasmall inorganic optical-PET imaging nanoparticle probe. *Science Translational Medicine*. 6:260ra149-260ra149

36. Chen Q, Wang C, Cheng L, He W, Cheng Z, Liu Z. 2014. Protein modified upconversion nanoparticles for imaging-guided combined photothermal and photodynamic therapy. *Biomaterials*. 35:2915–23

37. D'Andrade BW, Datta S, Forrest SR, Djurovich P, Polikarpov E, Thompson ME. 2005. Relationship between the ionization and oxidation potentials of molecular organic semiconductors. *Organic Electronics*. 6(1):11–20

38. Mikolajczyk A, Gajewicz A, Rasulev B, Schaeublin N, Maurer-Gardner E, et al. 2015. Zeta Potential for Metal Oxide Nanoparticles: A Predictive Model Developed by a Nano-Quantitative Structure–Property Relationship Approach. *Chem. Mater.* 27(7):2400–2407

39. Zhang S, Li J, Lykotrafitis G, Bao G, Suresh S. 2009. Size-Dependent Endocytosis of Nanoparticles. *Adv Mater*. 21:419–24

40. Gao J, Aksoy BA, Dogrusoz U, Dresdner G, Gross B, et al. 2013. Integrative Analysis of Complex Cancer Genomics and Clinical Profiles Using the cBioPortal. *Science Signaling*. 6(269):pl1–pl1

41. Cerami E, Gao J, Dogrusoz U, Gross BE, Sumer SO, et al. 2012. The cBio Cancer Genomics Portal: An Open Platform for Exploring Multidimensional Cancer Genomics Data. *Cancer Discov*. 2(5):401–4

42. Redza-Dutordoir M, Averill-Bates DA. 2016. Activation of apoptosis signalling pathways by reactive oxygen species. *Biochimica et Biophysica Acta (BBA) - Molecular Cell Research*. 1863(12):2977–92

43. Traverse CJ, Chen P, Lunt RR. 2018. Lifetime of Organic Salt Photovoltaics. *Advanced Energy Materials*. 8(21):1703678

44. Gui DY, Sullivan LB, Luengo A, Hosios AM, Bush LN, et al. 2016. Environment Dictates Dependence on Mitochondrial Complex I for NAD+ and Aspartate Production and Determines Cancer Cell Sensitivity to Metformin. *Cell Metabolism*. 24(5):716–27

45. Schindelin J, Arganda-Carreras I, Frise E, Kaynig V, Longair M, et al. 2012. Fiji: an open-source platform for biological-image analysis. *Nature Methods*. 9(7):676–82

46. Andrechek ER, Cardiff RD, Chang JT, Gatza ML, Acharya CR, et al. 2009. Genetic heterogeneity of Myc-induced mammary tumors reflecting diverse phenotypes including metastatic potential. *PNAS*. 106(38):16387–92

CHAPTER 3.

COUNTERION TUNING OF NIR ORGANIC SALTS IMPROVES PHOTOTOXICITY TO INHIBIT TUMOR GROWTH IN A METASTATIC BREAST CANCER MOUSE MODEL

3.1 PREFACE

This chapter is a modified version of a primary research manuscript.

3.2 Abstract

Photodynamic therapy (PDT) has the potential to improve cancer treatment by providing dual selectivity through the use of both photoactive agent and light, with the goal of minimal harmful effects from either the agent or light alone. However, current PDT is limited by insufficient photosensitizers (PSs) that suffer from low tissue penetration, insufficient phototoxicity (toxicity with light irradiation), and undesirable cytotoxicity (toxicity without light irradiation). To overcome these limitations, we reported a novel platform for decoupling optical and electronic properties with counterions that modulate frontier molecular orbital levels of a photoactive ion in Chapter 2. Here, we demonstrate the utility of this platform *in vivo* by pairing near-infrared (NIR) photoactive heptamethine cyanine cation (Cy^+), which has enhanced optical properties for deep tissue penetration, with counterions that make it cytotoxic, phototoxic, or nontoxic. We find that pairing Cy^+ with weakly coordinating anion $FPhB^-$ results in a selectively phototoxic photosensitizer (CyFPhB) that abolishes tumor growth *in vivo* with minimal side effects in a mouse model of metastatic breast cancer. This work provides proof-of-concept that our counterion pairing platform can be used to generate improved cancer photosensitizers that are selectively phototoxic to tumors and nontoxic to normal healthy tissue.

3.3 Introduction

The lack of targeted therapy options remains a major problem for effective treatment of many cancer types, and non-specific chemotherapy leads to harsh side effects due to unintended toxicity in normal tissue (1). A promising solution is photodynamic therapy (PDT), which uses light-activated photosensitizers (PSs) to treat

cancerous tissue by the generation of toxic reactive oxygen species (ROS) upon photoexcitation (2, 3). PSs that absorb and emit in the near-infrared (NIR) range (650-1200 nm) display superior tissue penetration and reduced photodamage by avoiding visible light wavelengths (400-650 nm) absorbed by biological tissue components (4, 5). Cyanines are commonly used NIR scaffolds due to their ease of synthesis, structural tunability, and biocompatibility (6–8). For example, indocyanine green is an NIR heptamethine cyanine used in diagnostic clinical cancer studies for sentinel lymph node mapping to detect metastasis (9). However, it suffers from poor chemical stability, nonspecific binding, and off target toxicity, resulting in limited medical usage (10, 11). Indeed, this is a common problem in cancer therapy: even with tumor targeting approaches such as nanoparticle formulation or antibody-conjugation, chemotherapeutics can still accumulate in healthy tissue, notably the liver (12–14). PDT with PSs such as Photofrin (porfimer sodium) and Foscan (mTHPC, temoporfin) have displayed off-site cytotoxicity (toxicity without light irradiation), preventing their use in many cancers (15, 16). Therefore, despite advances in tumor targeting, there is a need for NIR-PSs with selective phototoxicity (toxicity with light irradiation) with minimal cytotoxicity in normal tissue.

We recently reported a platform to modulate the toxicity of NIR photoactive heptamethine cyanine cation (Cy^+) by counterion pairing with weakly coordinating anions (17). The dipole-modulating counterions modify the frontier molecular orbital energy without changing the bandgap, allowing for independent modification of electronic properties from optical properties. This allows us to adjust the toxicity of the organic salts without affecting the optical properties such as absorption, emission, and

Stokes shift. The composition of photoactive salts is locked in cellular environments by formation of nanoparticles that prevent cation-anion dissociation (**Figure 3.1**). Indeed, these results showed that pairing Cy^+ with small, hard anions produce organic salts that are cytotoxic, while pairing with bulky, halogenated anions produces organic salts that are either phototoxic and non-cytotoxic or non-phototoxic and non-cytotoxic in human lung carcinoma cells (17). This novel engineering platform through counterion pairing could be used to design PS agents that are specifically designed for PDT with low cytotoxicity and high phototoxicity.

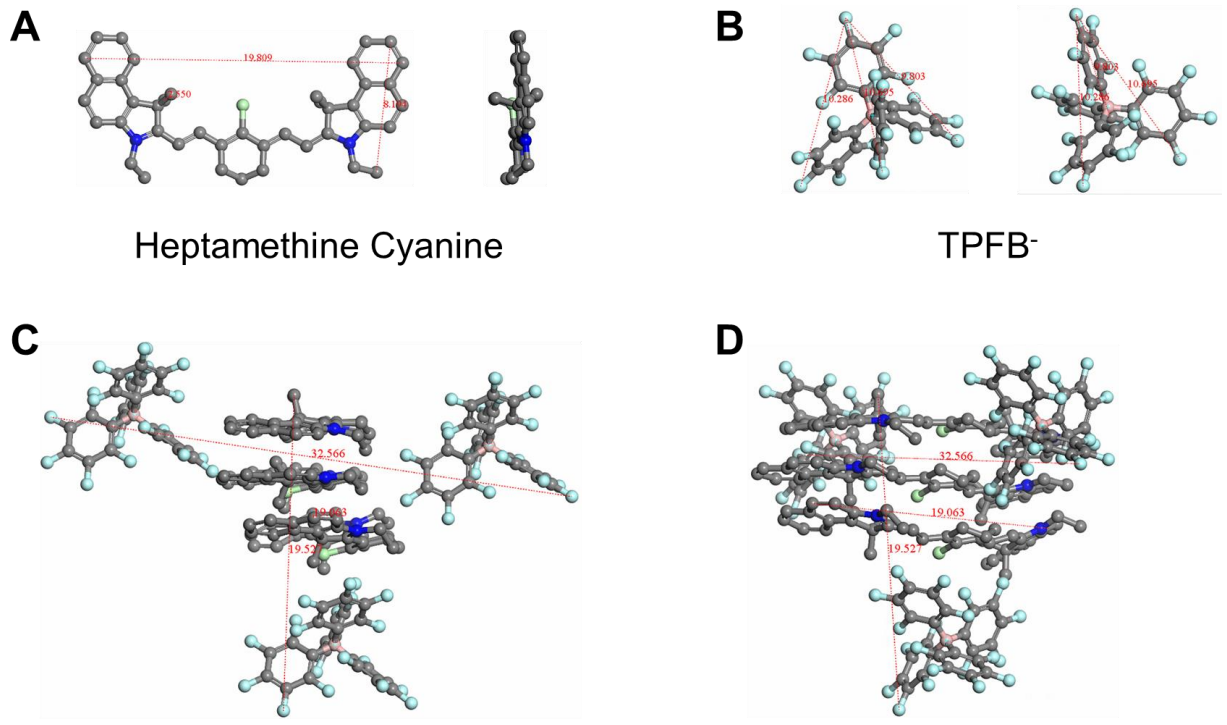

Figure 3.1 Schematic for a CyTPFB nanoparticle. (**A**) Dimensions of heptamethine cyanine cation and (**B**) $TPFB^-$ anion. (**C**) Potential model of an energetically feasible CyTPFB trimer nanoparticle within size constraints from SAXS (41 ± 6 angstrom) and SEM (70 ± 30 angstrom) diameter measurements (17). (**D**) Model rotated 90 degrees. Measured distances are in angstrom.

To test the hypothesis that our toxicity tuning platform can be used to design a PS with low cytotoxicity and high phototoxicity for PDT *in vivo*, we use a clinically relevant orthotopic mouse model of metastatic breast cancer: 6DT1 cells derived from an MMTV-Myc driven tumor inoculated into the fourth mammary fat pad of syngeneic FVB mice (18). This model allows us to assess our counterion-tuned PSs in a physiologically relevant tumor microenvironment in immunocompetent mice, which are both critical for metastasis and PDT pharmacodynamics studies (19–22). Furthermore, metastatic breast cancer has poor patient prognoses and no targeted therapies currently available, making it potential candidate for PDT (23).

In addition to their improved NIR optical properties, cyanine dyes have inherent tumor targeting capabilities, in large part due to their uptake by organic anion transporter polypeptides (OATPs, human; Oatps, rodent) (24, 25). OATPs are promiscuous cellular uptake mediators for numerous amphipathic endogenous and exogenous molecules; they are expressed throughout the body in a wide range of tissues and play a critical role in drug uptake and biodistribution (26). OATPA1/B1 and OATP2B1 transporters, which mediate uptake of cancer chemotherapeutics, are upregulated in a number of cancer cells, and are regulated by HIF-1α, a transcription factor commonly expressed in the hypoxic tumor environment (27, 28). PDT *in vitro* studies with cyanine dyes frequently assess cancer uptake specificity with inhibition assays of OATPA1/B1 and OATP2B1 transporters (29, 30). In addition to OATPs, recent studies suggest serum albumin may be an overlooked mediator of cyanine tumor targeting capabilities. Serum albumin is the predominant protein in the blood and is responsible for maintaining osmotic pressure and chaperoning endogenous molecules

through the vascular system (31). Albumin has been shown to have increased tumor accumulation due to upregulated albumin catabolism that fuels cancer growth (31). Recent studies report meso-chlorinated cyanines covalently bind to albumin, and these cyanine albumin adducts accumulate within the tumor interstitium (32, 33). Albumin is a commonly used targeting moiety for chemotherapeutics and nanomaterials; thus, albumin conjugation may contribute to the tumor targeting ability of cyanine dyes (34, 35). To assess the mechanisms of tumor targeting, biodistribution, and potential translatability of our findings to additional cancers and preclinical models, we characterize uptake mediated by mouse Oatps and albumin *in vitro*.

In this chapter, we use an orthotopic model of metastatic breast cancer to test PDT *in vivo* using Cy^+ paired with 3 different representative toxicity-tuning anions: hexafluorophosphate (PF_6^-), tetrakis (4-fluorophenyl) borate ($FPhB^-$), and tetrakis (pentafluorophenyl) borate ($TPFB^-$) (**Figure 3.2A**). We find that our previous *in vitro* results in human lung carcinoma and melanoma cell lines are reproducible both *in vitro* and *in vivo* in a metastatic breast cancer model, observing similar trends for the cytotoxic ($CyPF_6$), phototoxic (CyFPhB), and less toxic (CyTPFB) anion pairings. We further assess all three organic salts based on *in vivo* pharmacokinetics, antitumor efficacy with light irradiation, and offsite toxicity. Organic salts all display tumor specific accumulation *in vivo*, but we report differential influences of Oatps and albumin *in vitro.* Cellular uptake of $CyPF_6$ in culture is dependent on Oatps and shows increased liver uptake *in vivo*. We find CyFPhB is heavily reliant on albumin, and while the exact mechanism is not fully elucidated, we report increased tumor specific accumulation *in vivo*, providing a wide therapeutic window for NIR irradiation. We find that by using our

counterion tuning platform we can develop a potent PS agent, CyFPhB, which possesses enhanced phototoxicity that eliminates cancer growth upon NIR excitation with minimal side effects in a breast cancer mouse model. These *in vivo* results validate our counterion tuning strategy, which has potential to expand the clinical applications of cancer PDT agents.

3.4 Results

3.4.1 Counterion tuning of organic salts controls toxicity during photodynamic therapy of mouse metastatic mammary cancer cells *in vitro*

To confirm that our previous *in vitro* findings from A549 human lung cancer and WM1158 melanoma cell lines can be translated to our mouse model, we performed *in vitro* PDT on 6DT1 mouse mammary carcinoma cells following incubation with various concentrations of $CyPF_6$, CyFPhB, and CyTPFB with or without 850 nm light irradiation (17). We observe consistent results for 6DT1 cells as previously shown for A549 and WM1158 cells. $CyPF_6$ is cytotoxic in 6DT1 cells with similar half-maximal inhibitory concentration (IC_{50}) values of 1.0 µM and 0.7 µM without (dark IC_{50}) and with (NIR IC_{50}) light irradiation, respectively (**Figure 3.2B, Table S3.1**). CyFPhB is highly phototoxic with low cytotoxicity, with a dark IC_{50} of 9.3 µM and NIR IC_{50} of 3.4 µM (**Figure 3.2C, Table S3.1**). With a dark IC_{50} nearly 3x the concentration of the NIR IC_{50}, CyFPhB is a promising candidate for *in vivo* PDT applications. CyTPFB displays minimal cytotoxicity and minor phototoxicity with a dark IC_{50} of 45.2 µM and NIR IC_{50} of 21.6 µM (**Figure 3.2D, Table S3.1**). While there is a two-fold difference in dark and NIR IC_{50}, a NIR IC_{50} concentration of 21.6 µM is too high to achieve *in vivo* for PDT applications (36).

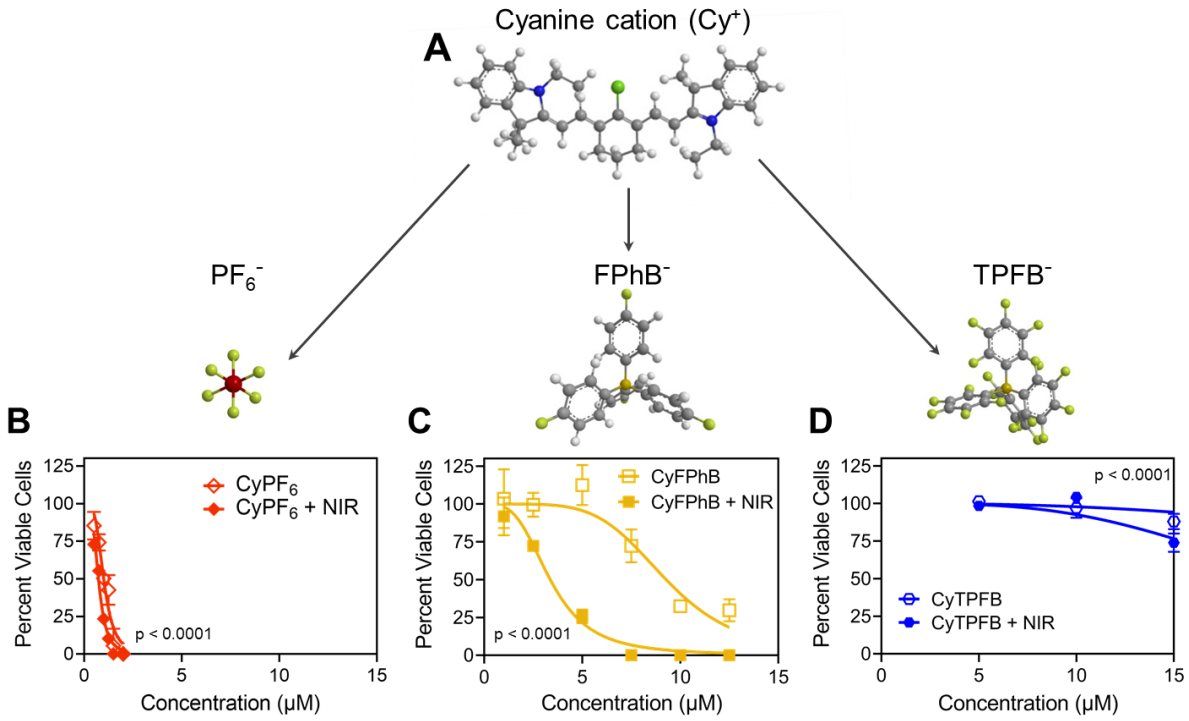

Figure 3.2 Fluorescent organic salts can be used as photosensitizing agents to treat breast cancer cells. Mouse mammary cancer cells (6DT1) were incubated with the indicated concentrations of organic salt pairings with or without near-infrared (NIR, 850 nm) irradiation to determine half maximal inhibitory concentrations (IC_{50}). (**A**) Photoactive heptamethine cyanine cation (Cy^+) is tuned with counterions to modulate toxicity. (**B**) $CyPF_6$ is toxic at low concentrations, and cell death occurs independent of NIR irradiation (Dark IC_{50} = 1.0 μM, NIR IC_{50} = 0.7 μM). (**B**) CyFPhB does not display significant toxicity without NIR activation (Dark IC_{50} = 9.3 μM), but when photoexcited induces significant cancer cell death (NIR IC_{50}= 3.4 μM). (**C**) CyTPFB displays low toxicity with and without NIR irradiation (Dark IC_{50} = 45.2 μM, NIR IC_{50} = 21.6 μM). Data are displayed as means ± S.E.M., n = 3. Statistical significance (p-values) of IC_{50} shifts (Dark IC_{50} vs NIR IC_{50}) are displayed on graphs.

3.4.2 Oatps and albumin mediate cellular uptake of fluorescent organic salts

Next, we investigated the roles of Oatps and albumin on mediating cancer cell uptake of fluorescent organic salts and verified their relevance in our model. As discussed above, OATPs and albumin have been shown to mediate uptake of cyanine dyes. Data from Gene Expression Omnibus (GEO) shows that 6DT1 tumors and cells in

culture express the gene product of mouse Oatp1b2 (slco1b2), which has 65% amino acid sequence homology with human OATP1B1 (**Table S3.2**) (37). In addition to expression of Oatp1b2, 6DT1 tumors and cells express higher levels of proteins that uptake albumin, including Secreted Protein Acidic and Rich in Cysteine than found in surrounding breast tissues (38, 39) (**Table S3.2**). These expression data show that our 6DT1 model reflects expression trends found in human breast cancer and is therefore appropriate and clinically relevant for investigating Oatp- and albumin-mediated cellular uptake of cyanine organic salts.

To assess the role of Oatps on organic salt uptake in our breast cancer model, 6DT1 cells were pre-incubated in cell media with 250 μM bromosulfophthalein (BSP), a competitive inhibitor of Oatps, or 1mM dimethyloxalylglycine (DMOG), a HIF-1α stabilizer to increase expression of Oatps (27, 32, 40, 41). Following drug pre-incubation, organic salts were added to cell media, and intracellular fluorescence was measured at various time points to determine cellular uptake. Fluorescence over time was plotted and fit with a sigmoidal curve to determine uptake kinetics. Nanoparticle absorption spectra were monitored using UV-vis to confirm that addition of chemical agents did not affect nanoparticle composition or stability (**Figure 3.3**). Cellular uptake of $CyPF_6$ increases rapidly upon addition to media, reaches maximal uptake at 4 hours, and stably plateaus after 6 hours. (**Figure 3.4A, Table S3.3**). $CyPF_6$ cellular uptake dynamics fit a standard sigmoidal curve, indicative of protein-mediated transport. Corroborating this result, BSP inhibition of Oatps eliminates $CyPF_6$ uptake, displaying

minor cellular uptake only after 8 hours and 84.2 ± 11.6% decrease from $CyPF_6$ at 25

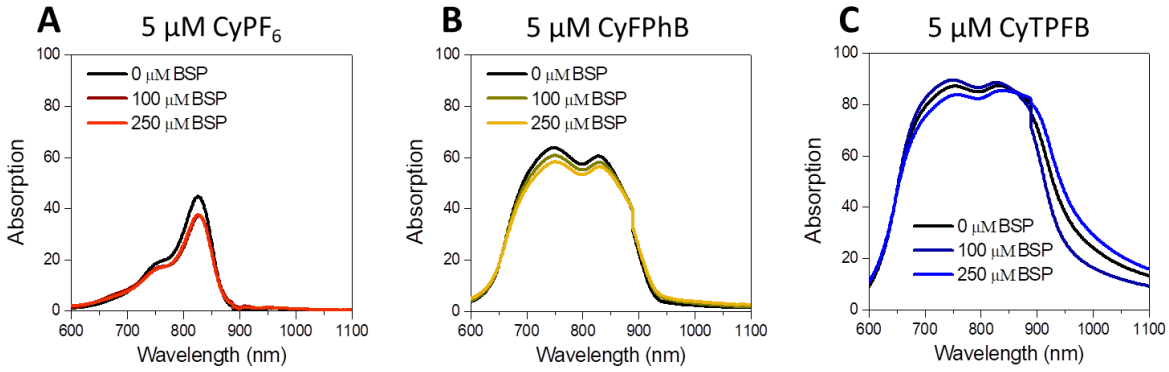

Figure 3.3 Addition of Oatps inhibitor bromosulfophthalein (BSP) does not affect organic salt nanoparticle composition or absorption in cell media. Absorption (100-%T) data collected with UV-Vis spectroscopy for 5 µM (**A**) $CyPF_6$, (**B**) CyFPhB, and (**C**) CyTPFB with increasing concentrations of BSP

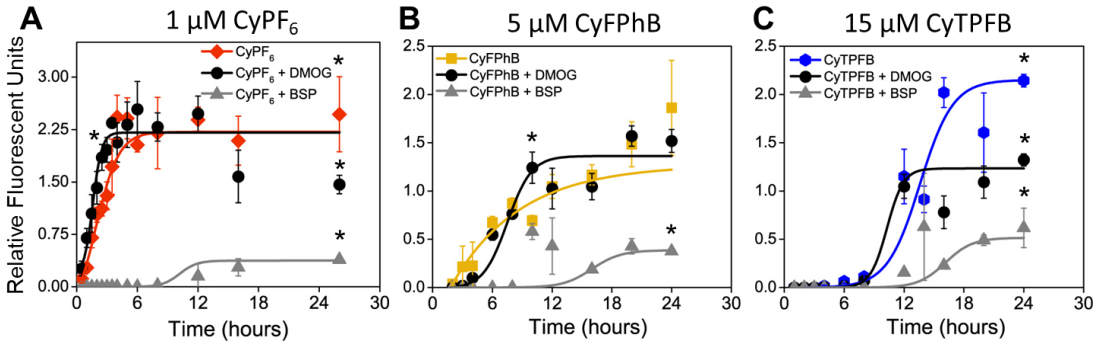

Figure 3.4 Organic anion transporter polypeptides (Oatps) mediate cellular uptake of $CyPF_6$, but only partially account for CyTPFB and CyFPhB uptake. 6DT1 cells were preincubated with 1 mM dimethyloxalylglycine (DMOG), a HIF-1α stabilizer, or 250 µM bromosulfophthalein (BSP), a competitive Oatps inhibitor. Following pre-incubation with Oatps modulating drugs, cells were incubated with the indicated organic salt over 25 hours. Curves were fit using a sigmoidal dose-response function using Origin Pro8. (**A**) 1 µM $CyPF_6$ quickly reaches saturated maximal uptake at 4 hours, following a standard sigmoidal curve fit. Addition of DMOG increases the initial rate of uptake, and BSP inhibits a significant 84% of uptake at 25 hours. (**B**) 5 µM CyFPhB has a slower rate of uptake relative to $CyPF_6$, linearly increasing to reach maximal uptake at 24 hours, but unlike $CyPF_6$ there is no uptake saturation. DMOG increases the initial rate of uptake and BSP inhibits 79% of uptake. (**C**) 15 µM CyTPFB follows a sigmoidal uptake trend, but similar to CyFPhB BSP inhibits only 71% of uptake. This data demonstrates that OATPs are important for cellular uptake, but they mediate the uptake of the organic salt pairings differently. Data are displayed as means ± S.D., $n = 3$. Statistically significant differences (p-value < 0.05) are marked with asterisks.

hours. As expected, DMOG modestly increases the rate of $CyPF_6$ uptake, with similar levels of saturation after 6 hours. CyFPhB displays substantially delayed cellular uptake, increasing steadily with incubation time until experimental end at 24 hours (**Figure 3.4B, Table S3.3**). CyFPhB cellular uptake over time follows a linear trend, poorly fitting a sigmoidal curve, and does not display saturable uptake. BSP inhibition inhibits 79.8 ± 14.0% percent of uptake at 24 hours. Addition of DMOG increases the initial rate of uptake and plateaus at 12 hours, fitting a sigmoidal curve. Similar to CyFPhB, CyTPFB has delayed uptake, reaching maximal uptake at 24 hours, and BSP only inhibits 71.1 ± 6.3% of cellular uptake. However, it also displays a high rate of uptake at 12 hours and saturates at 24 hours, fitting a sigmoidal curve similar to $CyPF_6$ (**Figure 3.4C, Table S3**). These results indicate that while Oatps mediate $CyPF_6$ cellular uptake in a 6DT1 cell model, they only partially account for CyFPhB and CyTPFB uptake and an additional cellular transport mechanism is likely present.

Noting the differences in Oatps uptake and kinetic trends, we examined alternative forms of cellular uptake. We previously reported that organic salt nanoparticles display different electronic zeta potentials, which could cause differences in protein affinity (17). Therefore, we investigated endocytotic mechanisms. We did not observe a difference in organic salt uptake upon incubation with various endocytotic inhibitors (dynasore, methyl-β-cyclodextrin, amiloride) (**Figure 3.5**). However, we observed notable differences in uptake in serum free media (Dulbecco's Modified Eagle Medium, DMEM): CyFPhB uptake decreased dramatically when cells were incubated in media without serum, while $CyPF_6$ and CyTPFB display similar levels of uptake (**Figure 3.6A**). To determine if this effect was mediated by changes to organic salt structure in

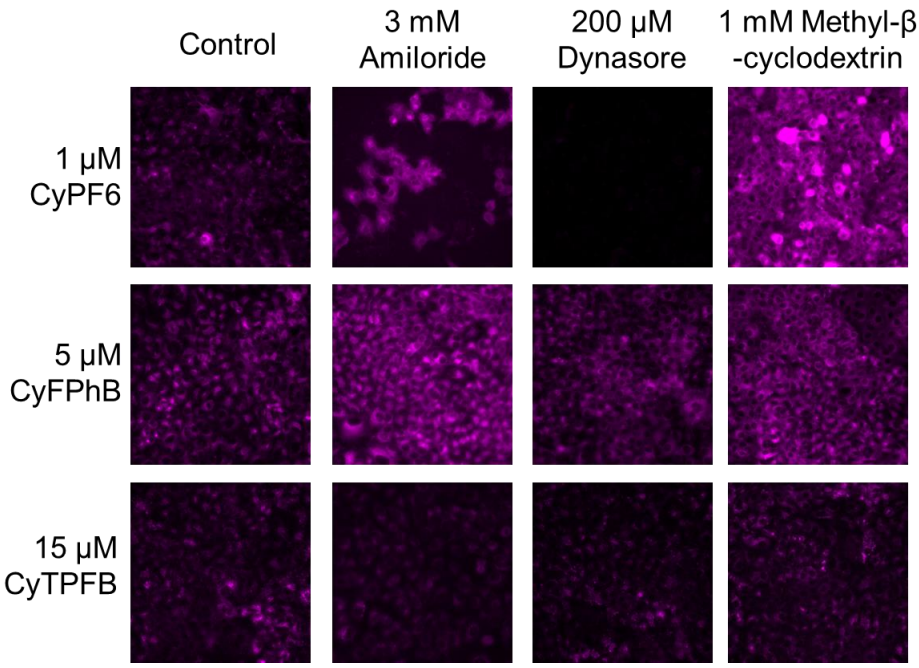

Figure 3.5 Endocytotic inhibition does not inhibit uptake of organic salts. 6DT1 cells were pretreated with amiloride, dynasore, or methyl-β-cyclodextrin. Control samples were treated with an equivalent volume of DMSO. Cells were then incubated with 1 µM $CyPF_6$, 5 µM CyFPhB, or 15 µM CyTPFB and fluorescence intensity was measured at 8 hours. While there is a decrease in fluorescence intensity for $CyPF_6$ + Dynasore, this has been found to be due to an interaction between the molecules themselves and not a decrease in cellular uptake.

different solutions and the serum component responsible, UV-vis spectroscopy was performed on organic salts in DMEM, DMEM + serum, and DMEM with increasing concentrations of bovine serum albumin, the most abundant protein in blood serum (42). We find that DMEM destabilizes CyFPhB and $CyPF_6$ nanoparticles, while CyTPFB remains stable (**Figure 3.6B-D, Figure 3.7**). Albumin stabilizes the entire CyFPhB nanoparticle, but only the Cy^+ monomer from the $CyPF_6$ organic salt (**Figure 3.6B-C**). To determine the effect this may have on cellular uptake, 6DT1 cells were incubated in serial dilutions of purified bovine serum albumin in DMEM with the indicated organic

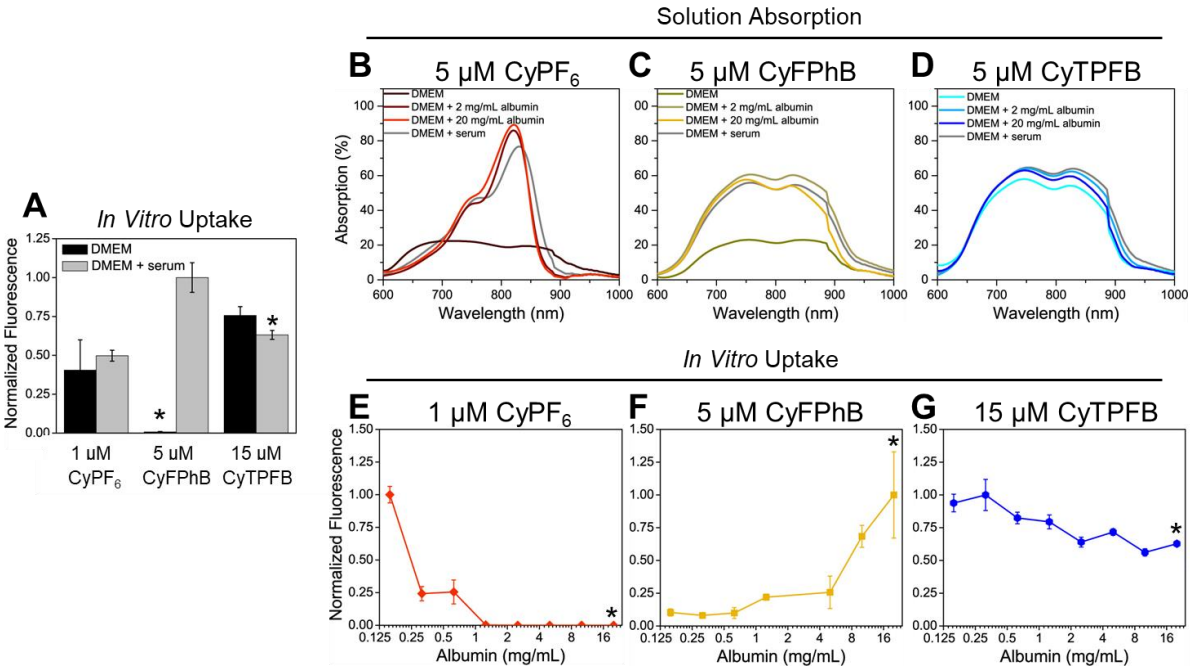

Figure 3.6 Albumin plays a critical role in organic salt stability and uptake. (**A**) 6DT1 cells were incubated in serum-free media (DMEM) and complete media (DMEM + serum) over 24 hours with organic salts. In the absence of serum, only negligible amounts of intracellular fluorescence were measured with 5 μM CyFPhB. 15 μM CyTPFB and 1 μM $CyPF_6$ only display minor changes in the presence of serum. (**B**) To determine the serum component responsible, UV-vis spectroscopy was used to characterize 5 μM organic salts in DMEM with increasing amounts of bovine serum albumin. (**B**) DMEM destabilizes the $CyPF_6$ nanoparticle, as can be seen by reduction in the absorbance peak height. Addition of albumin stabilizes only the Cy^+ monomer from $CyPF_6$, not the complete nanoparticle. (**C**) DMEM destabilizes the CyFPhB nanoparticle; however, the addition of albumin stabilizes the entire nanoparticle. (**D**) CyTPFB maintains a stable nanoparticle formation in all solutions. These trends are also observed in complete cell media, indicating that albumin interaction has a significant impact in biological systems. Complete spectra can be found in **Figure 3.7**. To determine the influence of albumin on cellular uptake, cells were incubated with serial dilutions of albumin in DMEM with the indicated organic salt. Intracellular fluorescence was normalized to maximal fluorescence intensity. (**D**) Addition of albumin inhibits cellular uptake of 1 μM $CyPF_6$, displaying higher maximal uptake in the presence of lower amounts of albumin, and uptake is entirely abolished at higher concentrations. (**F**) 5 μM CyFPhB cellular uptake increases correlatively with albumin concentration. (**G**) 15 μM CyTPFB displays a moderate decrease in cellular uptake at higher concentrations of albumin. Data are displayed as means ± S.D., $n = 3$. Statistically significant differences (p-value < 0.05) between initial albumin concentration and final albumin concentration are marked with asterisks.

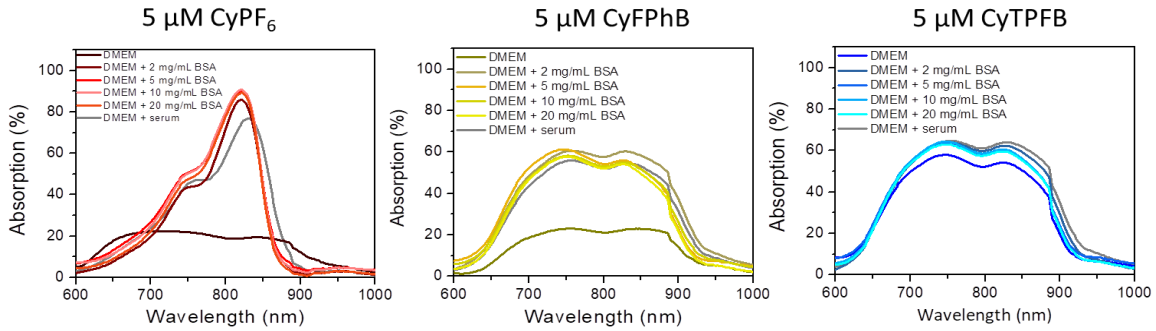

Figure 3.7 Absorption (100-%T) data collected with UV-Vis spectroscopy for 5 µM $CyPF_6$, CyFPhB, and CyTPFB with increasing concentrations of bovine serum albumin (BSA) in serum free DMEM, and complete cell media (DMEM + serum). DMEM destabilizes $CyPF_6$ and CyFPhB nanoparticles. BSA stabilizes the CyFPhB nanoparticle, but only the Cy^+ monomer from $CyPF_6$.

salts. Surprisingly, intracellular fluorescence from $CyPF_6$ decreased with increasing albumin concentration (**Figure 3.6E**). CyFPhB has negligible uptake in DMEM and requires albumin for cellular uptake, increasing correlatively with the concentration of albumin (**Figure 3.6F**). CyTPFB is not as inhibited to the same degree as $CyPF_6$ but is still negatively correlated with increasing concentrations of albumin (**Figure 3.6G**). While albumin may stabilize the Cy^+ monomer from $CyPF_6$, increasing albumin concentration has a negative correlation with cellular uptake. We verified that this trend is not due to changes in $CyPF_6$ fluorescent quantum yields when associated with albumin (**Figure 3.8**). This data shows that while Oatps are predominately responsible for $CyPF_6$ uptake, CyFPhB is reliant on albumin to enter the cell.

3.4.3 Organic salts display differential *in vivo* biodistribution

In vivo experiments were performed to verify trends observed *in vitro* and potential clinical application. FVB mice received an orthotopic injection of 10,000 syngeneic 6DT1 mammary cancer cells into the 4^{th} mammary fat pad. At 9 days post-injection, a

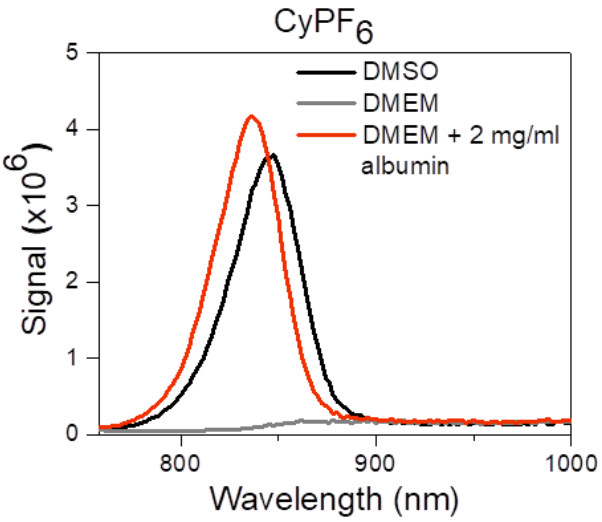

Figure 3.8 Photoluminescence spectra of $CyPF_6$ monomers. Absolute scale, background corrected photoluminescence spectra for 1 μM $CyPF_6$ monomers in DMSO, DMEM, and DMEM + 2mg/ml bovine serum albumin demonstrates that albumin association does not significantly influence fluorescent quantum yields.

palpable tumor formed, and mice received an intravenous injection of $CyPF_6$, CyFPhB, or CyTPFB through the tail vein. Biodistribution of organic salts was tracked using a fluorescent stereo microscope, which allowed monitoring of tumor localization and PS clearance from normal tissue. To assess *in vivo* biodistribution, fluorescent intensity was measured over 5 days from the liver, the tumor located on the right mammary fat pad, and the non-tumor bearing left mammary fat pad (**Figure 3.9A**). Tumor uptake trends are consistent with those observed *in vitro* (**Figure 3.4**). $CyPF_6$ is rapidly uptaken and dispersed into all measured tissue, but initially at 1.5-6 hours is predominately localized within the liver. Maximal tumor fluorescence is at 24 hours but only displays a modest increase from liver fluorescence. Observed tumor clearance is slower than from normal tissue, allowing a minor difference in fluorescence at 48 hours of 24.5% ± 4.9; however, tumor fluorescence is then cleared rapidly, displaying poor overall retention (**Figure 3.9B**). We have shown $CyPF_6$ is strongly dependent on Oatps for uptake (**Figure 3.4**),

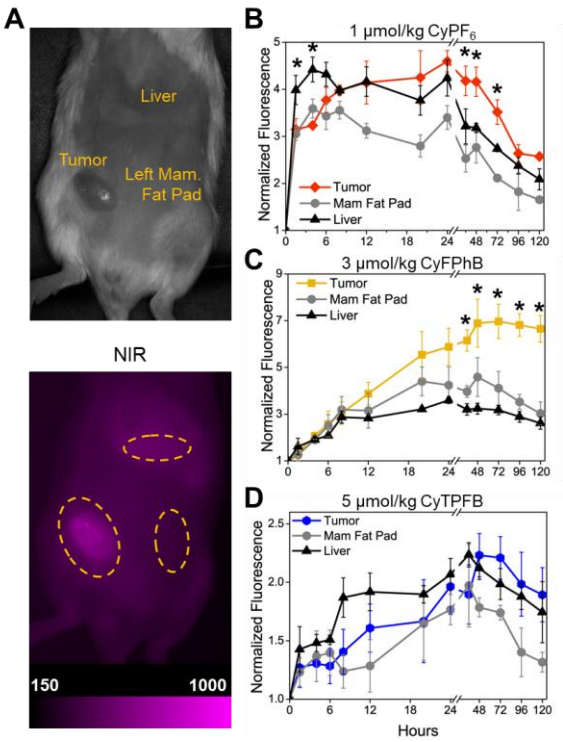

Figure 3.9 *In vivo* biodistribution data shows organic salts preferentially accumulate and are retained within 6DT1 tumors. Following 6DT1 tumor formation mice received a tail vein injection of 1 μmol/kg $CyPF_6$, 3 μmol/kg CyFPhB, or 5 μmol/kg CyTPFB. (**A**) NIR fluorescence from the tumor-bearing 4th right mammary fat pad, liver, and left 4th mammary fat pad was measured to determine biodistribution of organic salts. Pictured is a mouse dosed with 1 μmol/kg $CyPF_6$ at 48 hours. Fluorescence intensity was normalized to a vehicle control. (**B**) $CyPF_6$ displays rapid tissue uptake in the first 12 hours, predominately to the liver which reaches maximal uptake at 6 hours. Maximal tumor uptake is at 24 hours and displays modest retention over 48 hours before gradually diminishing after 72 hours. There is an effective therapeutic window between 36 and 48 hours, when there is a statistically significant 24% increase in tumor fluorescence compared to the liver. (**C**) CyFPhB displays slower tumor uptake, reaching maximal fluorescence intensity at 48 hours, however, it stably remains within the tumor environment, while clearing from normal tissue. There is no liver specific accumulation as observed with $CyPF_6$, and after 24 hours the tumor fluorescence intensity continues to rise while fluorescence in the liver and mammary fat pad plateaus and then decreases. At 72 hours CyFPhB displays a 45% tumor fluorescence increase from normal tissue and is stably retained up to 120 hours as fluorescence persists within the tumor. The observed broad therapeutic window from 36-120 hours is both longer and possesses a greater magnitude of tumor specific retention than $CyPF_6$. (**D**) CyTPFB displays a similar biodistribution as observed with $CyPF_6$, displaying initial liver specific uptake, but also the prolonged tissue uptake as observed with CyFPhB. Data are displayed as means ± S.D., $n = 3$. Statistically significant differences (p-value < 0.05) between tissue samples are marked with asterisks.

but this effect could also lead to increased hepatic uptake and faster clearance as observed here, as these transporters are also present in hepatocytes and responsible for drug uptake (43). We again observe delayed uptake with CyFPhB, reaching maximal uptake at 48 hours, but do not observe the same degree of liver uptake compared to $CyPF_6$ (**Figure 3.9C**). CyFPhB liver fluorescence is similar to background tissue, as quantitated by the fluorescence of the non-tumor bearing right mammary fat pad. Indeed, CyFPhB displays exceptional tumor specific uptake, reaching over 45.2 ± 10.2% fluorescent signal increase from surrounding tissues over 48-72 hours, giving it an ideal therapeutic window for PDT. CyTPFB displays prolonged fluorescent uptake similar to CyFPhB, but also displays liver uptake similar to $CyPF_6$ (**Figure 3.9D**).

3.4.4 CyFPhB is a selectively phototoxic antitumor agent when combined with NIR irradiation

For PDT experiments (**Figure 3.10A**), tumor-bearing mice were dosed with 1-5 µmol/kg of the indicated organic salt or vehicle control (Veh) and irradiated with 150 J/cm^2 of 810 nm light (Veh + NIR, CyX + NIR) at 48 and 96 hours following organic salt administration (**Figure 3.10B**). Dark control group mice did not undergo light irradiation (Veh, CyX). This protocol was repeated a week later. Tumor volume was monitored with caliper measurements and mice were euthanized on day 28 due to tumor burden in control groups. Mouse health was monitored throughout the experiment by weight and visual inspection of light irradiation site every other day, and with blood chemistry assays at endpoint. In the 5 µmol/kg $CyPF_6$ + NIR treatment group all mice expired within 24 hours post-injection (**Figure 3.10C**). The 3 µmol/kg $CyPF_6$ + NIR group exhibited severe tail swelling and could only undergo one course of the PDT protocol

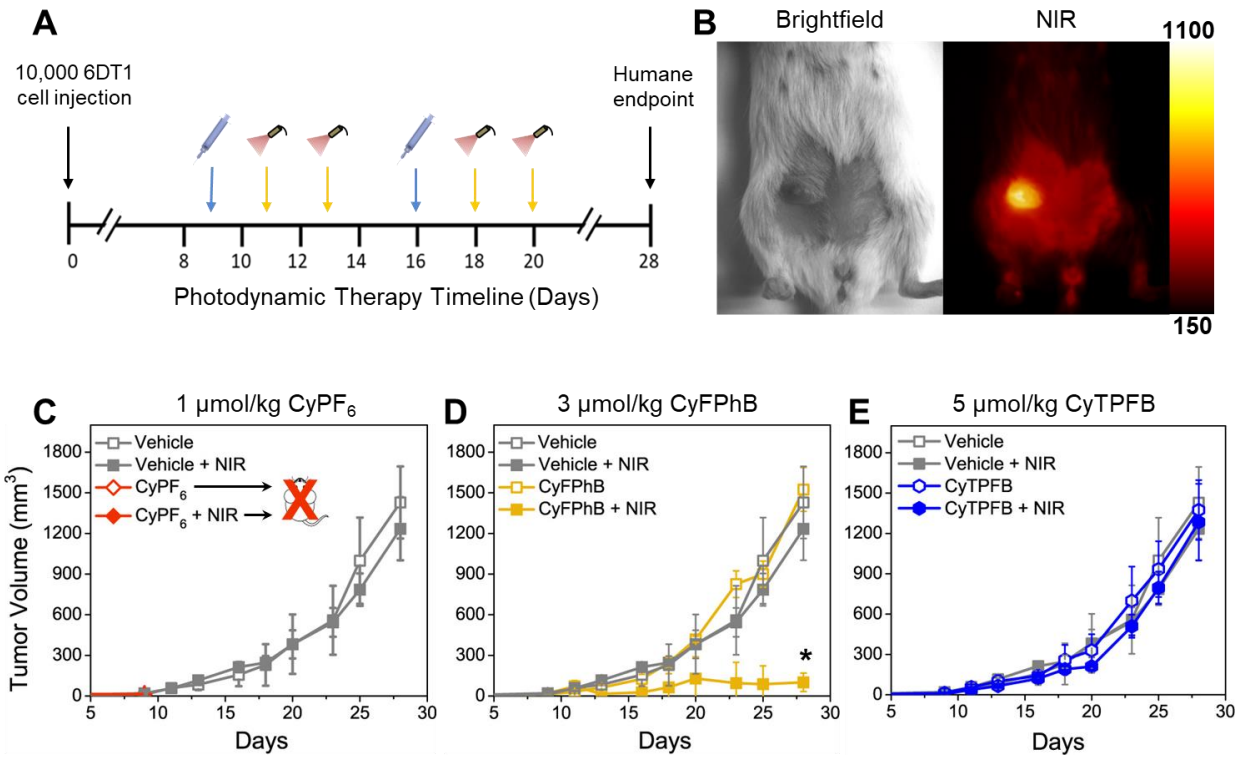

Figure 3.10 Counterion tuning of organic salts produces a potent photosensitizer (PS) for photodynamic therapy (PDT) in a metastatic breast cancer mouse model. (**A**) Experimental overview of photodynamic therapy experimental timeline. FVB mice were injected with 10,000 6DT1 cells into the fourth right mammary fat pad. After 9 days, when a palpable tumor is present, mice were dosed with an organic salt via intravenous tail vein injection. After 2 days the organic salt has localized within the tumor and cleared from the surrounding offsite tissue. Mice are then irradiated with 150 J/cm^2 of 810 nm near-infrared light (NIR) at 48 and 96 hours following organic salt administration. This PDT regimen is then repeated one week after the first organic salt injection. Tumor growth is monitored throughout the course of the experiment with manual caliper measurement until 28 days when mice are euthanized due to tumor burden. (**B**) Representative image of tumor specific localization of organic salts prior to NIR light irradiation. Pictured is an FVB mouse 44 hours post IV injection of 5 µmol/kg CyFPhB. (**C**) 5 µmol/kg $CyPF_6$ is too toxic for PDT. Even without NIR irradiation mice succumb to the non-specific cytotoxicity of the treatment and die within 48 hours of organic salt administration. The experiment was repeated at 1 µmol/kg $CyPF_6$, but there was no discernable difference between $CyPF_6$ treatment groups from the vehicle control groups (**Figure 3.12**). $CyPF_6$ does not have an adequate dosage margin between non-specific cytotoxic effects, and light activated phototoxicity, making it unsuitable for PDT. (**D**) 3 µmol/kg CyFPhB did not show any acute off target cytotoxic effects independent of NIR treatment (CyFPhB) and upon NIR irradiation eliminates tumor growth (CyFPhB + NIR). At the end of the experiment, the CyFPhB + NIR treatment group showed 93% reduction in tumor volume compared to controls. (**E**) 5 µmol/kg CyTPFB did not display

Figure. 3.10 (cont'd)

any cytotoxicity or phototoxicity. Data are displayed as means ± S.D., $n = 4$. Error bars represent SD. Statistically significant differences (p-value < 0.05) in CyFPHB + NIR tumor volumes from control groups at endpoint are marked with asterisks (*).

(**Figure 3.11**). There was no observable change to tumor growth or appearance following light irradiation. 1 µmol/kg $CyPF_6$ with or without NIR light irradiation did not display any discernable effect on tumor growth compared to control groups (**Figure 3.12**). Similar trends were also observed with CyI, demonstrating that PF_6^- is not independently toxic *in vivo*, which has also been shown *in vitro* in previous works (**Figure 3.13**) (17).

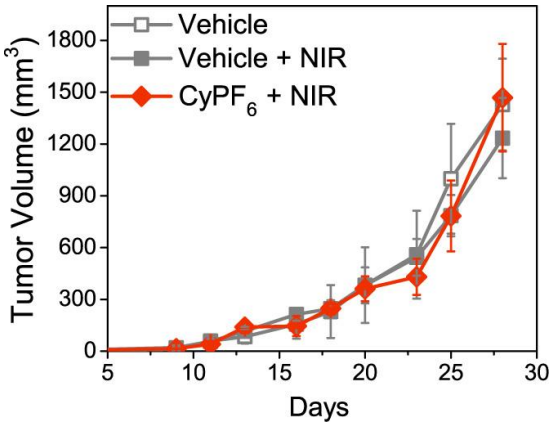

Figure 3.11 Tumor growth with 3 µmol/kg $CyPF_6$. No difference observed in tumor growth with 3 µmol/kg $CyPF_6$ with NIR light (150 J/cm^2) from vehicle controls. Severe tail swelling after the first injection of 3 µmol/kg $CyPF_6$ limited the treatment protocol to one organic salt injection and 2 light treatments. Data are displayed as means ± S.D., n = 3, Error bars represent SD.

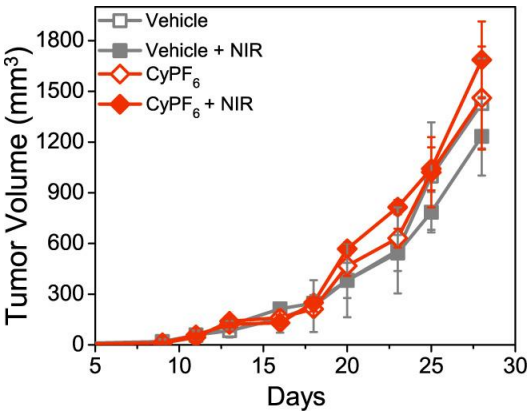

Figure 3.12 Tumor growth with 1 µmol/kg $CyPF_6$. No difference observed in tumor growth with 1 µmol/kg $CyPF_6$ with or without NIR light (150 J/cm^2), consistent with data in **Figure 3.10C** that there is not an adequate margin between cytotoxic and phototoxic dosages for effective *in vivo* PDT. At higher dosages there is significant tissue damage (3 µmol/kg $CyPF_6$) and mice do not survive treatment (5 µmol/kg $CyPF_6$). Data are displayed as means ± S.D., $n = 4$. Error bars represent SD.

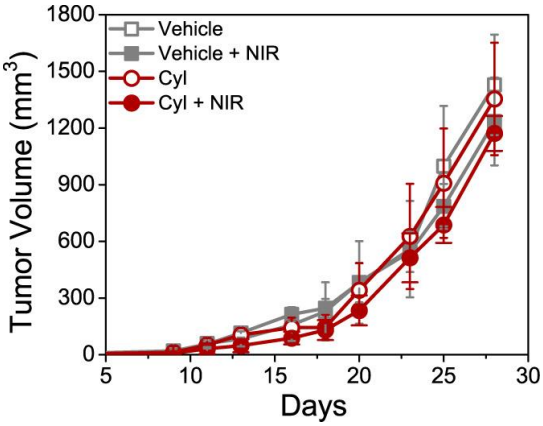

Figure 3.13 Tumor growth with 1 µmol/kg Cyl. No difference observed in tumor growth with 1 µmol/kg Cyl with or without NIR light (150 J/cm^2), following the same trend observed with $CyPF_6$ (**Figure 3.10C**, **Figure 3.12**). Data are displayed as means ± S.D., $n = 4$. Error bars represent SD.

CyFPhB + NIR treatment is found to have a potent antitumor effect at a 3 µmol/kg dosage. After the first light treatment on day 11, a bruise formed around the tumor, which then formed a black eschar. This is indicative of vascular specific-PDT, a combination of direct photodamage to the cancer cells and ablation of the tumor vascular, which starves the tumor of nutrients (44). There was a 93% reduction in tumor

volume from control groups in the 3 μmol/kg CyFPhB + NIR treatment group at experimental endpoint (**Figure 3.10D**). CyFPhB, Veh, and Veh + NIR control groups all displayed severe labored breathing and decreased activity by day 28, while the CyFPhB + NIR group are still visually healthy. CyFPhB is also found to be non-toxic at 5 μmol/kg, however, there is not an appropriate level of dye clearance at 48 hours from normal tissue and CyFPhB + NIR treatment groups display health issues with only moderate tumor remission (**Figure 3.14**). 5 μmol/kg CyTPFB with or without NIR light did not exhibit any antitumor effect (**Figure 3.10E**). This cannot be directly attributed to counterion tuning due to the poor tumor accumulation of CyTPFB (**Figure 3.9D**).

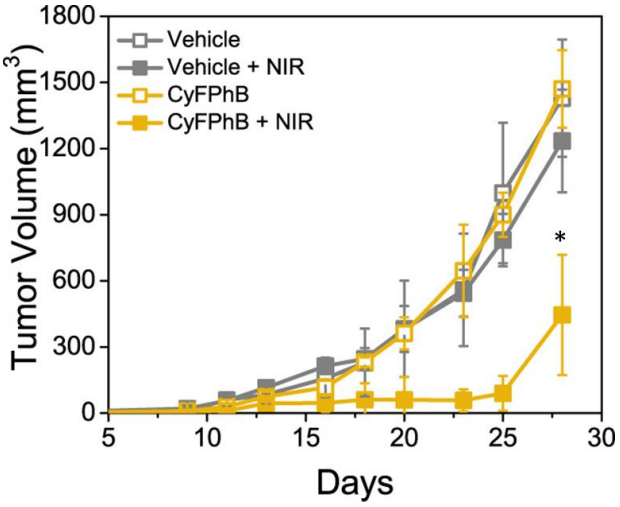

Figure 3.14 Tumor growth with 5 μmol/kg CyFPhB. *In vivo* PDT with 5 μmol/kg CyFPhB and NIR light (120 J/cm^2) can effectively inhibit tumor growth. Excessive dosages of CyFPhB (5 μmol/kg CyFPhB) than required for efficacious therapy (3 μmol/kg CyFPhB) still does not display cytotoxic effects as observed with $CyPF_6$. Data are displayed as means ± S.D., $n = 4$. Error bars represent SD. Statistically significant differences (p-value < 0.05) in CyFPHB + NIR values from control groups are marked with asterisks (*).

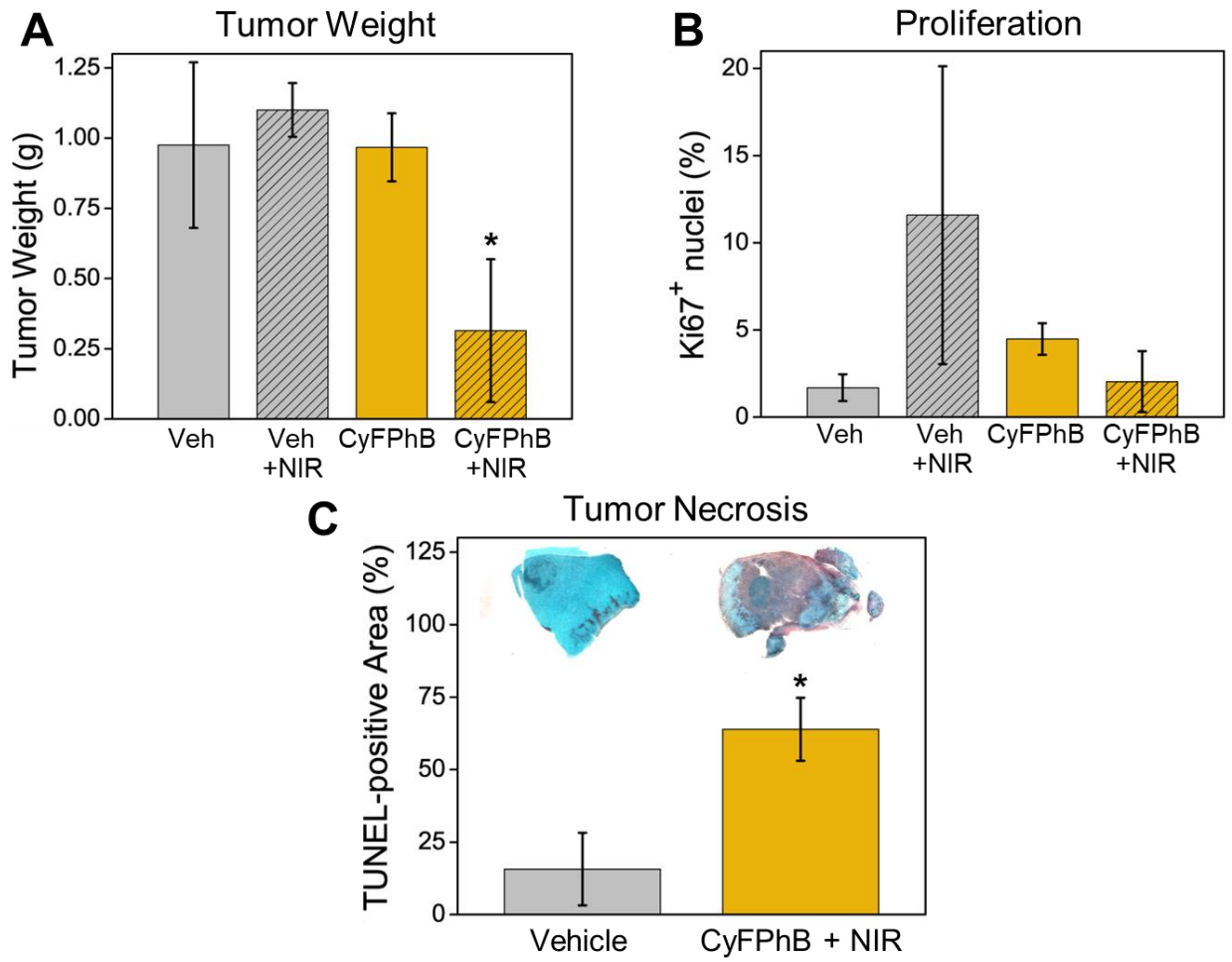

Figure 3.15 CyFPhB irradiated with NIR light induces an antitumor effect via tumor necrosis and impedes cancer progression in a metastatic breast cancer mouse model. At the end of the PDT experiment, tumor tissue from the 3 µmol/kg CyFPhB treatment groups was collected for further analysis of disease progression. (**A**) Tumor weight confirms trends observed in tumor volume throughout the course of the experiment. CyFPhB + NIR treated tumors show a significant 69% decrease in weight from control tumors at 28 days. (**B**) Tumor cross sections were stained for Ki67, a proliferation biomarker. There were no statistically different differences across groups, showing that CyFPhB + NIR treatment does not drive aggressive tumor growth. One of the CyFPhB + NIR tumors was completely eradicated, and therefore was not available for analysis (CyFPhB + NIR, n=3) (**C**) 3 days following NIR irradiation, PDT-treated tumors display increased terminal deoxynucleotidyl transferase dUTP nick end labeling (TUNEL), a marker of apoptotic and necrotic regions (Vehicle, n = 3, CyFPhB + NIR, n =3). Values are the average of four samples unless otherwise indicated. Error bars represent SD. Statistically significant differences (*p*-value < 0.05) in CyFPHB + NIR values from control groups are marked with asterisks (*).

At the experimental endpoint mice were sacrificed, and tumors were collected, weighed, and underwent histological analysis to further analyze treatment response. The CyFPhB + NIR group displays 69% decrease from control tumor weights, confirming volume calculations from caliper measurements (**Figure 3.15A**). A concern with many cancer treatments is that the treatment may drive selection to induce increased tumor malignancy, leading to recurrence and drug resistance (45, 46). To assess this, healthy margins of tumors were stained for Ki67, a proliferation biomarker which is commonly used to prognose tumor aggressiveness (47, 48). There was no increase in $Ki67^+$ nuclei in the FPhB + NIR group compared to control groups, and by percent-positive nuclei, all tumors would be considered $Ki67^+$-low (**Figure 3.15B**) (49).

Terminal deoxynucleotidyl transferase dUTP nick end labeling (TUNEL) assays determined apoptotic and necrotic regions within the CyFPhB-NIR treated tumor (50). TUNEL-stained cells are identified by brown staining within tumor cross-sections. Samples taken at the end of the experiment no longer had any relevant necrotic regions (**Figure 3.16**), however samples taken 72 hours after PDT treatment display extensive TUNEL-staining indicative of tumor necrosis and apoptosis (**Figure 3.15C, Figure 3.17**).

3.4.5 CyFPhB + NIR antitumor treatment has minimal side effects to normal tissue

Mouse weight and skin irritation at the site of light irradiation were recorded throughout the course of the experiment to monitor acute toxic side effects. Due to the aggressiveness of the 6DT1 breast cancer model, control tumors did display minor ulceration prior to experimental endpoint. This was not observed in the CyFPhB + NIR

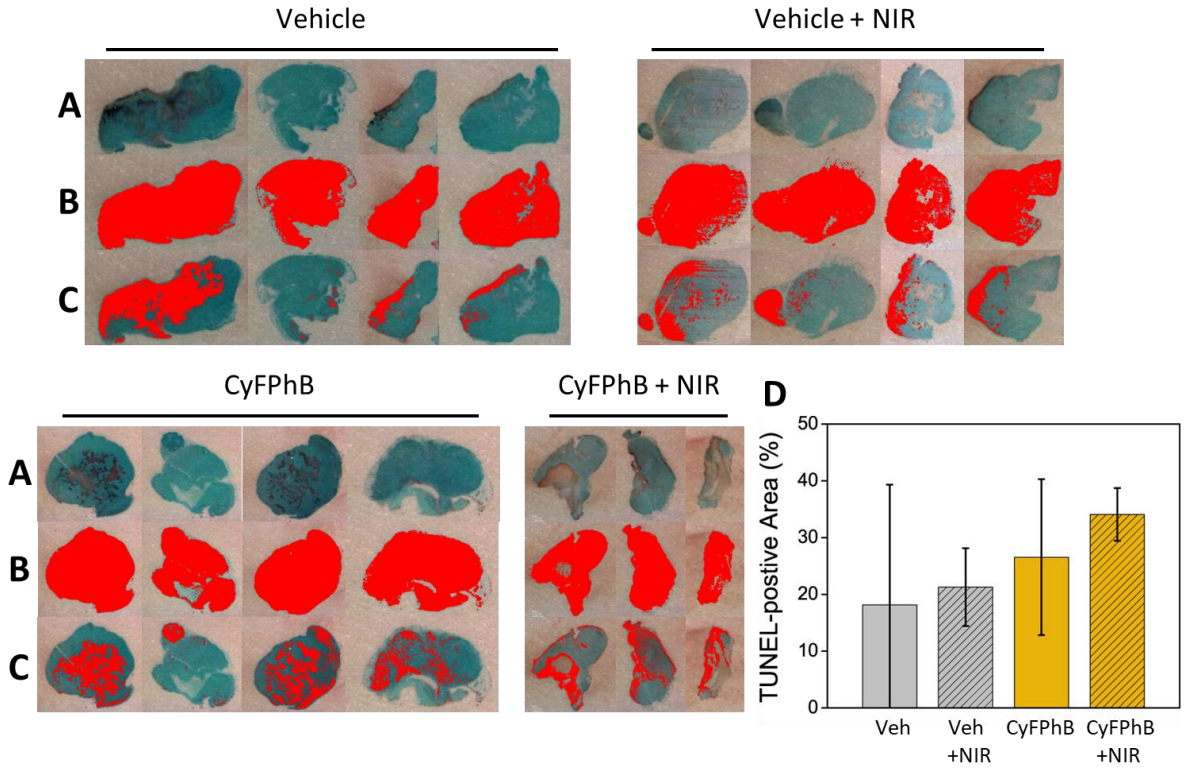

Figure 3.16 TUNEL assay color thresholds for treatment groups at experimental endpoint (28 days). (**A**) Cross-sections of tumors after TUNEL staining. Images with (**B**) TUNEL$^+$ area highlighted, and (**C**) full tumor area highlighted were used to calculate the percent area of TUNEL$^+$ staining shown in **Figure 3.16D**.

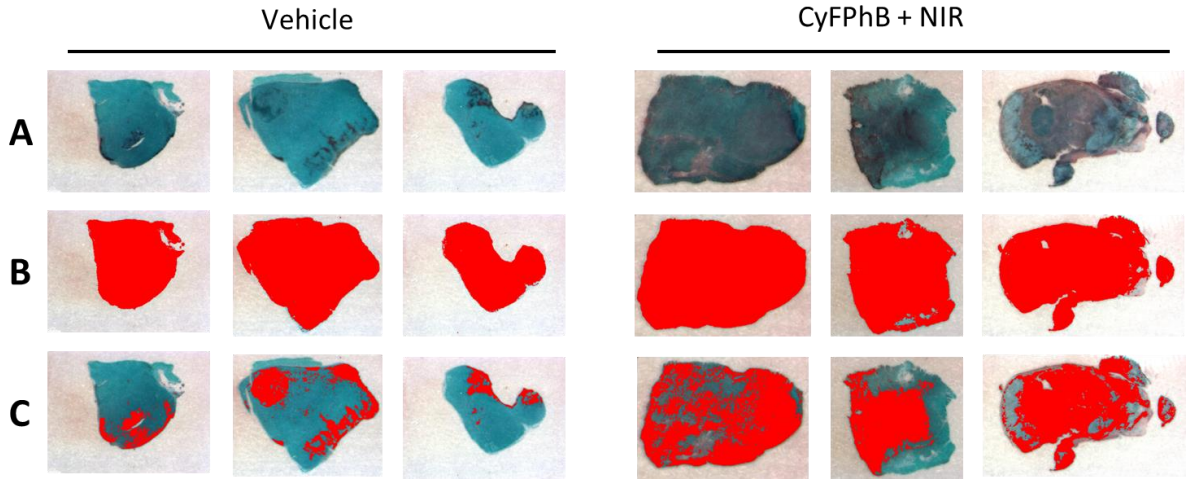

Figure 3.17 TUNEL assay color thresholds for Vehicle and CyFPhB + NIR treatment groups 3 days after PDT. (**A**) Cross-sections of tumors after TUNEL staining. (**B**) TUNEL$^+$ area highlighted, and (**C**) full tumor area highlighted were used to calculate the percent area of TUNEL$^+$ staining shown in **Figure 3.15C**.

group as a result of reduced tumor growth, and the black eschar formed during the ablation of the tumor was healing at experimental end. Body weights were measured every other day and urine assessed weekly for proteinuria using clinical dipsticks. There were no detectable levels of protein in found in urine samples (**Table S3.4**). There was a minor decrease in mouse weight after PDT, however the mice recovered, and weight loss is primarily attributed to dehydration as the weight rebounds rapidly (**Figure 3.18A**). There is a minor difference in final weight at the end of the experiment, though this is not statistically significant and can also be accounted for by the lack of a large tumor in CyFPhB + NIR mice. Liver health was assessed at the end of the experiment by measuring blood serum levels of aspartate aminotransferase (AST) and alanine aminotransferase (ALT), biochemical markers of liver damage. All CyFPhB + NIR treatment mice displayed serum values within normal ranges and did not increase from control treatment mice serum values (51) (**Figure 3.18B, Figure 3.19**).

While CyFPhB + NIR mice were visibly in good condition upon experimental endpoint, potential offsite toxicity was assessed from tissue where residual fluorescence was noted upon *ex vivo* organ extraction, notably the spleen, kidneys, duodenum, and liver (**Figure 3.18C**). These tissues were fixed in formalin and underwent H&E staining. The CyFPhB + NIR group did not display any morphological alterations or increased inflammatory exudation (**Figure 3.18D**). Collectively, this data demonstrates that CyFPhB is a promising photosensitizing anticancer agent with minimal side effects.

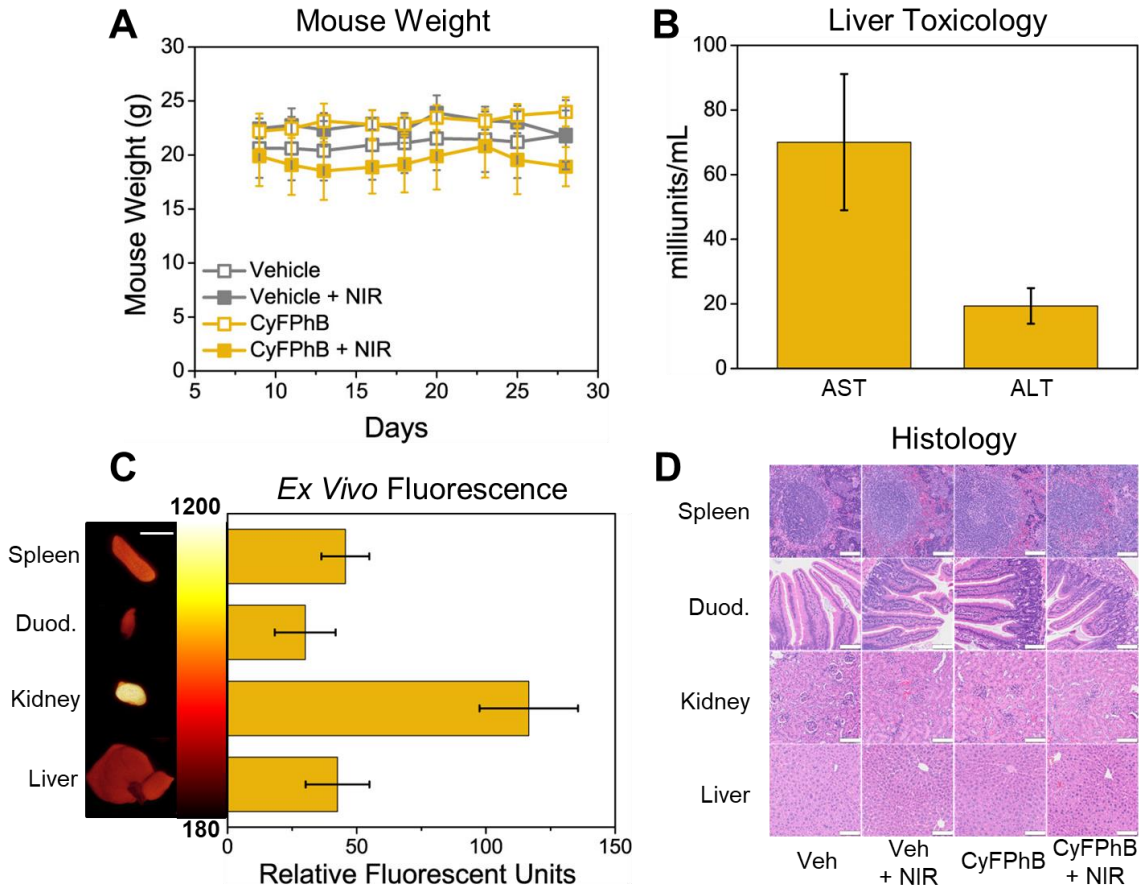

Figure 3. 18 Minimal systemic toxicity is observed with CyFPhB + NIR treatment. (**A**) There is minor decrease in mouse weight following CyFPhB + NIR treatment, but there no statistical difference due to a wide degree of variance in mouse size and no mouse lost more than 10% of body weight throughout the course of the experiment. (**B**) At experimental endpoint aspartate aminotransferase (AST) and alanine aminotransferase (ALT) serum levels were measured to assess liver damage. CyFPhB + NIR treatment groups fall within normal serum levels. (**C**) Residual fluorescence of normal biological tissue (spleen, duodenum, kidney, liver) from CyFPhB + NIR treatment mice. Representative images of each group are shown with fluorescence intensity. Inset bar = 10 mm. (**D**) No morphological alterations or increased immune invasion were found within tissues that retain CyFPhB organic salts, as measured by fluorescence in panel C. Representative histological images from each treatment group are shown. Inset bar = 100 μM. Data are displayed as means ± S.D., $n = 4$. Error bars represent SD.

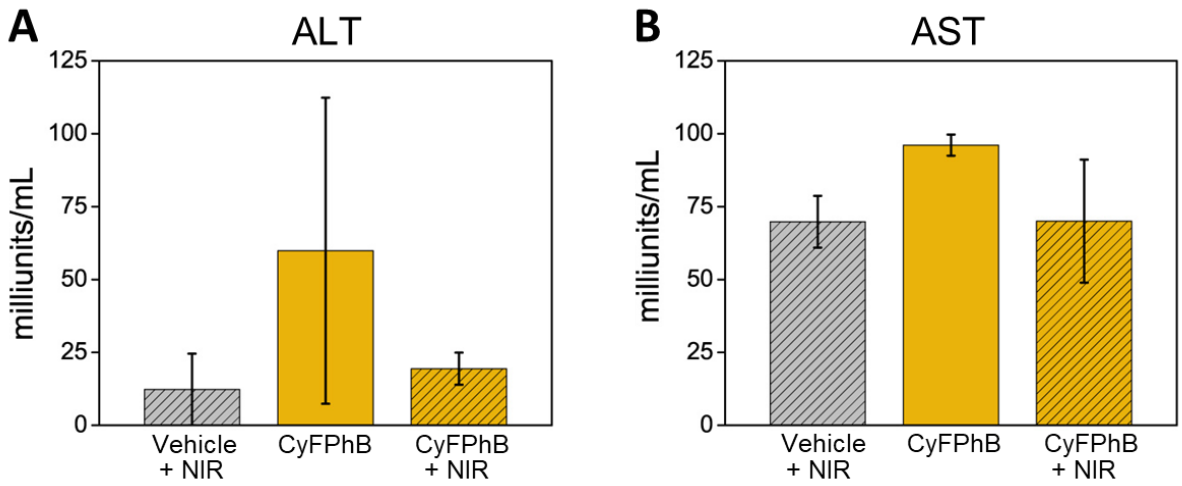

Figure 3. 19 Serum levels of liver enzymes AST and ALT. At experimental endpoint, (**A**) alanine aminotransferase (ALT) and (**B**) aspartate aminotransferase (AST) serum levels were measured to assess liver damage. All 3 µmol/kg CyFPhB treatment groups fall within normal serum levels.

3.5 Discussion

In this study, we explore the utility of counterion tuned organic salts for *in vivo* PDT in a metastatic breast cancer model. To do so, we developed a thorough *in vivo* PDT regimen for assessment of counterion tuned organic salts' antitumor efficacy, biodistribution, and off-site toxicity to normal tissue. We find that without counterion modulation, organic salt cytotoxicity independent of NIR irradiation is too severe for efficacious therapeutic concentrations. Reflecting trends reported *in vitro*, the margin between dark cytotoxicity and light-induced phototoxicity is too small in CyI or $CyPF_6$ for effective therapy. Mice die or cannot complete the full PDT regimen due to passive cytotoxicity in normal tissue, but at lower concentrations there is not an adequately potent phototoxic effect to suppress tumor growth. By using a weakly coordinating counterion to modulate toxicity ($FPhB^-$), we have reduced off target cytotoxicity and

improved phototoxicity to inhibit tumor growth in an aggressive breast cancer model. We report CyFPhB has improved characteristics for a therapeutic PS, including NIR-absorption, prolonged tumor retention, and high phototoxicity relative to cytotoxicity, reducing tumor growth by 93% with no toxicity to normal tissue.

Following CyFPhB + NIR treatment we observe bruising and formation of an eschar within 24 hours, which is then followed by shrinking of the tumor and formation of necrotic and apoptotic regions, determined by TUNEL-staining. Due to the combination of the observed tumor necrosis and the appearance of a bruise at the irradiation site, this antitumor effect is likely due to destruction of the tumor vasculature. While there is a probable combination of PDT induced photodamage directly to tumor and indirectly to the vasculature, in many preclinical studies the primary antitumor effect is due to PDT ablation of the tumor vasculature, leading to tumor starvation and necrosis (51). This strategy of vasculature-PDT is reported in clinically approved PS talaporfin sodium and is characterized by bruising at the irradiation site (53).

We also assessed potential uptake mechanisms *in vitro* to elucidate the cause of tumor specific accumulation and determine translatability to alternative cancer models and human disease. We find that through a combination of serum albumin interaction and Oatp uptake our organic salt particles preferentially concentrate within tumors over time. We report a higher degree of liver accumulation in $CyPF_6$ and CyTPFB *in vivo*, which may be due to their reliance on cellular uptake by Oatps, which are also highly expressed in the liver. The effect of Oatps on the uptake of fluorescent molecules is well documented in the literature, however, it has been reported recently that assays commonly used to assess the effect of Oatps by BSP inhibition have several

confounding variables (29, 32). BSP interacts with a wide range of compounds besides Oatps and is fluorescent (54). We have attempted to account for this by including an orthogonal approach by increasing Oatp expression with DMOG, which corroborates the BSP inhibition results. Collectively, these results indicate that Oatps play a role in the cancer cell uptake of organic salts but should not be overinterpreted. For example, in this study CyTPFB demonstrates a reliance on Oatps for uptake *in vitro*, however, *in vivo* uptake was extremely poor. This could be due to other factors, but the magnitude of Oatp influence on organic salt uptake merits further investigation, particularly if Oatps affects *in vivo* tumor uptake and accumulation of organic salts. BSP also interferes with albumin binding, and tumor specific uptake historically attributed to Oatps may be in part due to albumin (55). We report an importance on albumin for organic salts *in vitro*, $CyPF_6$ displays albumin-induced monomeric stabilization; however, increasing concentrations of albumin lead to decreased uptake. Conversely, CyFPhB is stabilized as a nanoparticle, yet dependent on albumin for cellular uptake. While the influence of albumin is apparent, attempts to elucidate the entire mode of uptake have eluded current efforts. We do report lower levels of CyFPhB liver accumulation *in vivo*, and significantly higher levels of tumor retention over time.

Our findings constitute that our novel counterion tuning strategy has clinical potential and could revolutionize PS engineering. We have demonstrated efficacious PDT in an immunocompetent murine model of metastatic breast cancer, which holds promise for translating to human cancer after further validation in patient-derived xenografts. We do observe differences in cellular and tumor uptake, and the targeting methods relied in our mouse model may not translate to human cancer. However,

modern cancer treatment focuses on combinatorial, personalized therapy. Full realization of our counterion toxicity tuning method will likely involve direct tumor targeting, by stable incorporation into larger nanomaterials or antibody conjugation, common engineering platforms for multi-agent tumor delivery. Indeed, NIR-PSs are promising components for multimodal synergistic cancer therapy as they have deep tissue imaging capabilities, and their therapeutic mechanism strongly benefits from combinatorial therapy (56, 57). Reducing the nonspecific cytotoxicity and improving phototoxic yields with counterion tuning is an efficient engineering strategy to advance tumor-specific PDT and cancer medicine.

3.6 Methods

3.6.1 Synthesis and purification of organic salts

Precursor salts (CyI and $NaPF_6$, NaFPhB, or KTPFB) were dissolved in 5:1 methanol:dichloromethane (MeOH:DCM) mixtures and stirred at room temperature under inert nitrogen gas. The counterion precursor was added in 100% molar excess to drive the exchange of ions, and the product compounds precipitate out of solution after 5 minutes. Product was collected using vacuum filtration and rinsed with MeOH. Crude product was dissolved in minimal DCM and run through a silica gel plug with a DCM wash to remove unreacted precursors, side products, and other impurities. The product compound exiting the silica was identified by its color and elution time and collected. Excess DCM was removed in a rotary evaporator. Reaction yield and purity were confirmed using a high mass accuracy time-of-flight mass spectrometer coupled to an ultra-high performance liquid chromatography (UPLC-MS) in positive mode to quantify cations, and in negative mode to quantify anions. Typical reactions led to products

yields of >60% with purities >95%. Reaction schemes and purification procedures described previously were used (58, 59).

3.6.2 Cell culture conditions

Mouse mammary carcinoma cells (6DT1) were cultured in Dulbecco's Modified Eagle's Medium (DMEM, Corning) with 4.5 g/L glucose without sodium pyruvate with 10% heat inactivated fetal bovine serum supplemented with 2 mM glutamine and 1% penicillin and streptomycin. Cells were incubated in 37 °C with 5% CO_2 without light exposure. Fluorescent organic salts were dissolved to 5.6 mM in dimethyl sulfoxide (DMSO, Millipore Sigma, D4540), and then further diluted in aqueous solution to form nanoparticles for various experiments.

3.6.3 Cell viability studies

6DT1 cells were seeded at a density of 40,000 cells per well in 6-well tissue culture plates, in dye-laced or vehicle (DMSO) media. After 24 hours of incubation, media was aspirated and replaced with untreated media. Each well was irradiated with an 850 nm LED lamp with an irradiation flux of 425 mW/cm^2 for 30 minutes in the incubator, and control cells were left in a dark incubator without irradiation. Following irradiation treatment, the media was replenished with fresh dye-laced media and allowed to incubate for another 24 hours. The same procedure was done at 48 and 72 hours, but the cells received no further dye-laced media after 72 hours. Viable cell number was determined at 96 hours using 4% trypan blue and a Nexcelom Cellometer Auto T4 cell counter. All assays were done with 3 biological replicates. The half maximal

inhibitory concentration (IC_{50}) was determined by plotting percent inhibition versus concentration and fitting using a nonlinear regression with Graphpad Prism.

3.6.4 Kinetic inhibition studies

6DT1 cells were seeded at a density of 25,000 cells per well in 24-well tissue culture plates. After 24 hours, cells were pre-incubated for 15 minutes with 250 μM bromosulfophthalein (BSP, Cayman Chemical, 21058), or 12 hours with 1 mM dimethyloxalylglycine (DMOG, Sigma-Aldrich, D3695). Following the indicated pre-incubation with each inhibitor, the inhibitor-laced media was replaced with organic salts and inhibitor-laced media. For live cell imaging, the cells were washed x3 with PBS and excited with 740 nm light. Fluorescence was measured using a Leica DMi8 microscope with a Cy7 filter cube, PE4000 LED light source, DFC9000GT camera, and LAS X imaging software. Cellular fluorescence was measured at the indicated timepoints, and all conditions were done in triplicate. Fluorescence was quantitated using ImageJ software. Curve fitting was performed with Origin Pro8 software by plotting relative fluorescent units versus time and using a dose-response sigmoidal equation.

3.6.5 Endocytosis inhibition studies

6DT1 cells were seeded at a density of 25,000 cells per well in 24-well tissue culture plates. After reaching 80-90% confluency, cells were serum starved for 2 hours. Following serum starvation, cells were pre-incubated for 30 minutes in 3mM amiloride (Sigma, A7410), 1 hour in 1 mM methyl-β-cyclodextrin (Sigma, C4555), or for 20 minutes with 200 μM dynasore (Abcam, ab120192). Following pre-incubation with various endocytotic inhibitors, inhibitor-laced media was replaced with organic salts and

inhibitor-laced media. After 24 hours cellular fluorescence was measured as described above.

3.6.6 Ultraviolet visible spectroscopy

Organic salts were diluted to a concentration of 5 μM in cell media and combined with the indicated concentrations of inhibitors. For albumin characterization, organic salts were diluted to a concentration of 5 μM in cell media, serum free media (DMEM), and DMEM with the indicated concentrations of BSA. All dyes were characterized using a Perkin-Elmer 25 UV-Vis spectrometer in the wavelength range from 500–1100 nm in normal incidence transmission mode with a resolution of 1 nm and a 1.27 cm path length. Cell media with inhibitors was used as the solvent reference to remove reflections so that the absorption is calculated as 1-transmission.

3.6.7 Bovine serum albumin uptake studies

Purified bovine serum albumin (BSA, Sigma-Aldrich, A7030) was resuspended in serum-free media (DMEM) and was serially diluted to create the indicated concentrations. Indicated concentrations of fluorescent organic salts were added to solutions, and after 14 hours cellular fluorescence was measured as described above.

3.6.8 Photoluminescence

Photoluminescence (PL) spectra were collected using a PTI Spectrofluorometer for monomers of 5 μM $CyPF_6$, completely solubilized in DMSO or associated with 2mg/mL BSA in DMEM without phenol red.

3.6.9 Orthotopic cancer model

All animal protocols were approved and performed in accordance with guidelines set by the Institute of Animal Care and Use Committee (IACUC) of Michigan State University. 6DT1 cells were harvested for tumor implantation at 80% confluence while in the logarithmic phase of growth. 10,000 6DT1 cells in 50 µL of sterile saline were inoculated into the right fourth mammary fat pad of 6-8-week-old syngeneic FVB/NJ female mice (purchased from Jackson Laboratories, Bar Harbor, ME, USA), as described previously (60). Tumor growth was monitored every other day with external caliper measurements to determine tumor length and width to calculate volume, $V = L \times W^2/2$. Animal wellbeing was also monitored by recording mouse weight every other day and watching for potential skin irritation at the tumor site. The presence of protein in urine was monitored using urine reagent test strips (URS-1B/G/K/P, Cortez Diagnostics). Mice were euthanized at a 28-day endpoint, when majority of control mice exhibit excessive morbidity due to tumor burden. Following euthanasia by carbon dioxide asphyxiation and subsequent cervical dislocation, tissues of interest were collected for further analysis.

3.6.10 *In vivo* imaging

For biodistribution studies, at 11 days post orthotopic injection tumor bearing mice were dosed with 1 µmol/kg $CyPF_6$, 3 µmol/kg CyFPhB, or 5 µmol/kg CyTPFB via intravenous tail vein injection. For imaging, mice were anesthetized with 2.5% isoflurane and brightfield and NIR fluorescent images were taken at the indicated time points using a Leica M165FC stereoscope with a 740 nm PE4000 LED light source, DFC9000GT camera, and LAS X imaging software. Using ImageJ, brightfield images were used to

determine regions of interest (ROIs) for the tumor in the right 4th mammary fat pad, the liver, and the left 4th mammary fat pad. ROIs were then overlaid on the NIR fluorescent image for blinded quantitation of fluorescence intensity and normalized to a vehicle injected mouse. The study ended after 5 days upon tumor ulceration due to rapid tumor growth.

3.6.11 Photodynamic therapy

At 9 days post orthotopic injection tumor-bearing mice were randomly divided into 4 treatment groups, 1) vehicle injection (Veh), 2) organic salt injection (CyX), 3) vehicle injection with NIR light irradiation (Veh + NIR), 4) organic salt injection with NIR light irradiation (CyX + NIR). For organic salt injection treatment groups (2 and 4), mice were given a 1-5 µmol/kg intravenous injection of a fluorescent organic salt dissolved in 5% DMSO and 0.03% Tween 20 in 100 µL of sterile saline prior to injection through the lateral tail vein. Vehicle groups (1 and 3) received a tail vein injection of 5% DMSO and 0.03% Tween 20 in 100 µL of sterile saline. ImageJ software was used to quantitate relative brightness and localization within tumor tissue relative to normal tissue at various time points throughout the experimental study. At 48 hours post IV injection of the organic salt, NIR light irradiation groups (3 and 4) were anesthetized with 2.5% isoflurane, placed on a heated pad, and underwent tumor irradiation with an 810 nm LED. Mice received a 120-150 J/cm^2 dose over 15-20 minutes, depending on previously decided treatment conditions. This was repeated 48 hours later. A week following the first organic salt IV injection, the PDT treatment was repeated. The PDT experimental timeline is outlined above (**Figure 3.10A**).

3.6.12 Histology

All histologic preparation and immunohistochemistry staining was performed by the Investigative HistoPathology Laboratory at Michigan State University. Tumor, lung, spleen, kidney, liver, and duodenum were harvested, fixed in formalin, embedded in paraffin, sectioned and stained with hematoxylin and eosin (H&E) for qualitative analysis. Tissues were visualized using an Olympus VS200 research slide scanner at 20x magnification.

3.6.13 Ki67 nuclei staining assessment

Ki67 staining was measured using images taken from healthy cross-sections of tumors. Image processing was performed in ImageJ. The color images were first deconvoluted into H (hematoxylin) and DAB (diaminobenzidine) color channels using Color Deconvolution ("H DAB" deconvolution matrix). Deconvoluted H and DAB images were saved as new TIFF images. For each image, smoothing was applied 5 times, then Auto Local Threshold was performed using Phansalkar's's algorithm to detect stained nuclei. Stained nuclei were counted using Analyze Particles (minimum size 30, minimum circularity 0.3). To check that threshold parameters were appropriate, several output images were manually inspected to confirm that visually identifiable nuclei were properly counted. The percent $Ki67^+$ nuclei was calculated as the ratio of DAB-stained nuclei counts (representing proliferating cells) to H-stained nuclei counts (representing all cells) for each tumor.

3.6.14 TUNEL-area quantification

Terminal deoxynucleotidyl transferase–mediated dUTP nick end labeling (TUNEL) assays were evaluated using ImageJ to determine the percentage of necrotic to total area of each tumor cross-section. Images were acquired using a Leica M165FC stereo microscope operated at 1.6x magnification. Images were duplicated, smoothed to reduce artifacts, and color thresholding was used to select either the $TUNEL^+$ area or the entire tumor area. Representative thresholding can be found in **Figure 3.16** and **Figure 3.17**.

3.6.15 AST and ALT assays

Serum levels for alanine aminotransferase (ALT, Sigma-Aldrich, MAK052) and aspartate aminotransferase (Sigma-Aldrich, MAK055) were measured using commercially available kits according to the manufacturer's protocol. Samples were run in duplicate and averaged for analysis, before averaging levels for each treatment group.

3.6.16 Statistical Analyses

Statistical analyses were performed using an unpaired student’s t-test and all error bars are representative of standard deviation, except where otherwise noted. All displayed data has a minimum of 3 biological replicates. Curve fittings were done using Origin Pro8 and GraphPad Prism software. P-values < 0.05 are reported as statistically significant (*).

3.7 Acknowledgements

The authors thank Elliot Ensink and Amir Roshanzadeh for helpful discussions and critical reading of this manuscript. The authors also thank the Michigan State University (MSU) Mass Spectrometry Metabolomics Core, MSU Investigative Histopathology Laboratory, and Ryan Lewandowski in the lab of Dr. Harkema. This work was supported by the National Science Foundation under CAREER Grant No. (CBET 1845006) to S.Y.L. and a MSU Strategic Partnership Grant. D.B. was supported by the Aitch Foundation MSUFCU Fellowship. M.B. and R.R.L. were supported by the National Science Foundation under Grant No. (CBET 1702591).

3.8 Author Contributions

S.Y.L. and R.R.L. conceived the project. D.B., R.R.L, and S.Y.L. designed the experiments. D.B. performed all *in vitro* and *in vivo* experiments, analysis, and data visualization. H.C.D. designed and assisted with the orthotopic mouse injections and performed AST and ALT assays. M.B. synthesized and collected optical and characterization data of the organic salts. S.T.T. assisted with image analysis and early optimization studies for orthotopic injection and metastatic assessment. M.P.O. assisted with early optimization of PDT studies and IV injections. B.B. assisted with chemical synthesis. D.B., R.R.L, and S.Y.L. wrote the manuscript.

APPENDIX

Compound	Dark IC_{50} (μM)	95% CI	NIR IC_{50} (μM)	95% CI
$CyPF_6$	1.0	0.9-1.1	0.7	0.7-0.8
CyFPhB	9.3	8.0-10.8	3.4	2.9-3.9
CyTPFB	45.2	33.2-149.4	21.6	19.5-23.4

Table S3.1 Half maximal inhibitory concentrations (IC_{50}) of fluorescent organic salts with and without NIR irradiation in 6DT1 cells. IC_{50} values were generated by nonlinear regression analysis using GraphPad Prism.

Geoset	Sample ID	Sample	gene	ID	Mean Value	SD Value
GSE69006	GSM1689995, GSM1689996, GSM1689997. GSM1689998	6DT1 Tumors	gapdh	10386947	12.68333	0.305307
GSE69006	GSM1689995, GSM1689996, GSM1689997. GSM1689998	6DT1 Tumors	Sparc	10386058	13.13948	0.288961
GSE69006	GSM1689995, GSM1689996, GSM1689997. GSM1689998	6DT1 Tumors	slco1b2	10542615	4.599253	0.046681
GPL6096	GSM1703590	6DT1 cell line	actin	6964030	7.86698	NA
GPL6096	GSM1703590	6DT1 cell line	Sparc	6788410	11.7504	NA
GPL6096	GSM1703590	6DT1 cell line	slco1b2	6950727	4.02566	NA

Table S3.2 6DT1 gene expression values. Gene expression data for genes of interest (solute carrier organic anion transporter family member 1B2, slco1b2; Secreted Protein Acidic and Rich in Cysteine, Sparc) and levels of relative controls (glyceraldehyde-3-phosphate dehydrogenase, gapdh; actin) in 6DT1 tumors (n = 4 biological replicates) and cultured cells.

	R^2	Max Uptake	Standard Error	Slope Factor (p)	Standard Error
$CyPF_6$	0.97	2.22E+08	1.17E+07	0.38	0.14
$CyPF_6$ + DMOG	0.84	2.21E+08	1.31E+07	0.98	0.75
$CyPF_6$ + BSP	0.91	3.74E+07	3.42E+06	0.51	0.08
CyFPhB	0.94	1.27E+08	7.96E+07	0.06	0.21
CyFPhB + DMOG	0.95	1.36E+08	1.60E+07	0.35	0.04
CyFPhB + BSP	0.91	3.85E+07	8.71E+06	0.30	0.06
CyTPFB	0.98	2.15E+08	1.14E+07	0.26	0.02
CyTPFB + DMOG	0.97	1.23E+08	7.74E+07	0.52	0.04
CyTPFB + BSP	0.75	5.15E+07	1.43E+07	0.32	0.04

Table S3.3 Sigmoidal curve fitting values. Curve fitting values for graphs in Figure 3.2 were generated using a dose-response sigmoidal function in Origin Pro8.

	Week 1	Week 2	Week 3	Week 4
CyFPhB	< 30 mg/dL	< 30 mg/dL	< 30 mg/dL	< 30 mg/dL
CyFPhB + NIR	< 30 mg/dL	< 30 mg/dL	< 30 mg/dL	< 30 mg/dL

Table S3.4 Urinary protein throughout course of PDT. No significant difference was observed between 3 µmol/kg CyFPhB treatment groups with or without NIR irradiation. Mice were euthanized at week 4 with no detectable proteinuria.

REFERENCES

REFERENCES

1. Lee CH, Kim KW, Lee SM, Kim SY. 2020. Dose-Dependent Effects of Resveratrol on Cisplatin-Induced Hearing Loss. *Int J Mol Sci*. 22(1):E113

2. Broadwater D, Medeiros HCD, Lunt RR, Lunt SY. 2021. Current Advances in Photoactive Agents for Cancer Imaging and Therapy. *Annu Rev Biomed Eng*. 23:29–60

3. Dougherty TJ, Gomer CJ, Henderson BW, Jori G, Kessel D, et al. 1998. Photodynamic Therapy. *JNCI: Journal of the National Cancer Institute*. 90:889–905

4. Chance B. 1998. Near-Infrared Images Using Continuous, Phase-Modulated, and Pulsed Light with Quantitation of Blood and Blood Oxygenationa. *Annals of the New York Academy of Sciences*. 838:29–45

5. Wäldchen S, Lehmann J, Klein T, van de Linde S, Sauer M. 2015. Light-induced cell damage in live-cell super-resolution microscopy. *Sci Rep*. 5(1):15348

6. Usama SM, Thavornpradit S, Burgess K. 2018. Optimized Heptamethine Cyanines for Photodynamic Therapy. *ACS Appl. Bio Mater.* 1(4):1195–1205

7. Wu J, Pan D, Chung LWK. 2013. Near-infrared fluorescence and nuclear imaging and targeting of prostate cancer. *Transl Androl Urol*. 2(3):254–64

8. Bhattarai P, Dai Z. 2017. Cyanine based Nanoprobes for Cancer Theranostics. *Adv Healthc Mater*. 6(14):

9. Jewell EL, Huang JJ, Abu-Rustum NR, Gardner GJ, Brown CL, et al. 2014. Detection of sentinel lymph nodes in minimally invasive surgery using indocyanine green and near-infrared fluorescence imaging for uterine and cervical malignancies. *Gynecologic Oncology*. 133:274–77

10. Hope-Ross M, Yannuzzi LA, Gragoudas ES, Guyer DR, Slakter JS, et al. 1994. Adverse reactions due to indocyanine green. *Ophthalmology*. 101(3):529–33

11. Wang H, Li X, Tse BW-C, Yang H, Thorling CA, et al. 2018. Indocyanine green-incorporating nanoparticles for cancer theranostics. *Theranostics*. 8(5):1227–42

12. Choi CHJ, Alabi CA, Webster P, Davis ME. 2010. Mechanism of active targeting in solid tumors with transferrin-containing gold nanoparticles. *Proc Natl Acad Sci U S A*. 107(3):1235–40

13. Bolleddula J, Shah A, Shadid M, Kamali A, Smith MD, Chowdhury SK. 2020. Pharmacokinetics and Catabolism of [3H]TAK-164, a Guanylyl Cyclase C Targeted Antibody-Drug Conjugate. *Drug Metab Dispos*. 48(11):1239–45

14. Shah DK, Haddish-Berhane N, Betts A. 2012. Bench to bedside translation of antibody drug conjugates using a multiscale mechanistic PK/PD model: a case study with brentuximab-vedotin. *J Pharmacokinet Pharmacodyn*. 39(6):643–59

15. Dougherty TJ, Cooper MT, Mang TS. 1990. Cutaneous phototoxic occurrences in patients receiving Photofrin®. *Lasers in Surgery and Medicine*. 10:485–88

16. Yom SS, Busch TM, Friedberg JS, Wileyto EP, Smith D, et al. 2003. Elevated serum cytokine levels in mesothelioma patients who have undergone pleurectomy or extrapleural pneumonectomy and adjuvant intraoperative photodynamic therapy. *Photochem Photobiol*. 78(1):75–81

17. Broadwater D, Bates M, Jayaram M, Young M, He J, et al. 2019. Modulating cellular cytotoxicity and phototoxicity of fluorescent organic salts through counterion pairing. *Scientific Reports*. 9(1):15288

18. Pei XF, Noble MS, Davoli MA, Rosfjord E, Tilli MT, et al. 2004. Explant-cell culture of primary mammary tumors from MMTV-c-Myc transgenic mice. *In Vitro Cell Dev Biol Anim*. 40(1–2):14–21

19. Ross C, Szczepanek K, Lee M, Yang H, Peer CJ, et al. 2020. Metastasis-Specific Gene Expression in Autochthonous and Allograft Mouse Mammary Tumor Models: Stratification and Identification of Targetable Signatures. *Mol Cancer Res*. 18(9):1278–89

20. Faraji F, Pang Y, Walker RC, Nieves Borges R, Yang L, Hunter KW. 2012. Cadm1 is a metastasis susceptibility gene that suppresses metastasis by modifying tumor interaction with the cell-mediated immunity. *PLoS Genet*. 8(9):e1002926

21. Donohoe C, Senge MO, Arnaut LG, Gomes-da-Silva LC. 2019. Cell death in photodynamic therapy: From oxidative stress to anti-tumor immunity. *Biochim Biophys Acta Rev Cancer*. 1872(2):188308

22. Yang Y, Yang HH, Hu Y, Watson PH, Liu H, et al. 2017. Immunocompetent mouse allograft models for development of therapies to target breast cancer metastasis. *Oncotarget*. 8(19):30621–43

23. Abdul Pari AA, Singhal M, Augustin HG. 2021. Emerging paradigms in metastasis research. *J Exp Med*. 218(1):e20190218

24. Cooper E, Choi PJ, Denny WA, Jose J, Dragunow M, Park TI-H. 2021. The Use of Heptamethine Cyanine Dyes as Drug-Conjugate Systems in the Treatment of Primary and Metastatic Brain Tumors. *Frontiers in Oncology*. 11:1336

25. Shi C, Wu JB, Chu GCY, Li Q, Wang R, et al. 2014. Heptamethine carbocyanine dye-mediated near-infrared imaging of canine and human cancers through the HIF-1α/OATPs signaling axis. *Oncotarget*. 5:10114–26

26. Hagenbuch B, Stieger B. 2013. The SLCO (former SLC21) superfamily of transporters. *Mol Aspects Med*. 34(2–3):396–412

27. Wu JB, Shao C, Li X, Shi C, Li Q, et al. 2014. Near-infrared fluorescence imaging of cancer mediated by tumor hypoxia and HIF1α/OATPs signaling axis. *Biomaterials*. 35(28):8175–85

28. Schulte RR, Ho RH. 2019. Organic Anion Transporting Polypeptides: Emerging Roles in Cancer Pharmacology. *Mol Pharmacol*. 95(5):490–506

29. Yang X, Shi C, Tong R, Qian WP, Zhau HE, et al. 2010. Near Infrared Heptamethine Cyanine Dye-Mediated Cancer Imaging. *Clinical Cancer Research*

30. Guan Y, Zhang Y, Zou J, Huang L-P, Chordia MD, et al. 2019. Synthesis and Biological Evaluation of Genistein-IR783 Conjugate: Cancer Cell Targeted Delivery in MCF-7 for Superior Anti-Cancer Therapy. *Molecules*. 24(22):E4120

31. Merlot AM, Kalinowski DS, Richardson DR. 2014. Unraveling the mysteries of serum albumin—more than just a serum protein. *Front Physiol*. 5:

32. Usama SM, Park GK, Nomura S, Baek Y, Choi HS, Burgess K. 2020. Role of Albumin in Accumulation and Persistence of Tumor-Seeking Cyanine Dyes. *Bioconjugate Chem.* 31(2):248–59

33. Matsumura Y, Maeda H. 1986. A New Concept for Macromolecular Therapeutics in Cancer Chemotherapy: Mechanism of Tumoritropic Accumulation of Proteins and the Antitumor Agent Smancs. *Cancer Res*. 46(12 Part 1):6387–92

34. Han X, Xu X, Tang Y, Zhu F, Tian Y, et al. 2020. BSA-Stabilized Mesoporous Organosilica Nanoparticles Reversed Chemotherapy Resistance of Anaplastic Thyroid Cancer by Increasing Drug Uptake and Reducing Cellular Efflux. *Frontiers in Molecular Biosciences*. 7:390

35. Miele E, Spinelli GP, Miele E, Tomao F, Tomao S. 2009. Albumin-bound formulation of paclitaxel (Abraxane ABI-007) in the treatment of breast cancer. *Int J Nanomedicine*. 4:99–105

36. Chen J, Wang Y, Fang Y, Jiang Z, Wang A, Xue J. 2020. Improved photodynamic anticancer activity and mechanisms of a promising zinc(II) phthalocyanine-quinoline conjugate photosensitizer in vitro and in vivo. *Biomed Opt Express*. 11(7):3900–3912

37. Csanaky IL, Lu H, Zhang Y, Ogura K, Choudhuri S, Klaassen CD. 2011. Organic Anion–Transporting Polypeptide 1b2 (Oatp1b2) Is Important for the Hepatic Uptake of Unconjugated Bile Acids: Studies in Oatp1b2-Null Mice. *Hepatology*. 53(1):272–81

38. Desai N, Trieu V, Damascelli B, Soon-Shiong P. 2009. SPARC Expression Correlates with Tumor Response to Albumin-Bound Paclitaxel in Head and Neck Cancer Patients. *Transl Oncol*. 2(2):59–64

39. Ghinea N. 2021. Anti-Angiogenic Therapy: Albumin-Binding Proteins Could Mediate Mechanisms Underlying the Accumulation of Small Molecule Receptor Tyrosine Kinase Inhibitors in Normal Tissues with Potential Harmful Effects on Health. *Diseases*. 9(2):28

40. Zhao N, Zhang C, Zhao Y, Bai B, An J, et al. 2016. Optical imaging of gastric cancer with near-infrared heptamethine carbocyanine fluorescence dyes. *Oncotarget*. 7(35):57277–89

41. Zhang S, Ma K, Liu Y, Pan X, Chen Q, et al. 2016. Stabilization of Hypoxia-inducible Factor by DMOG Inhibits Development of Chronic Hypoxia-Induced Right Ventricular Remodeling. *J Cardiovasc Pharmacol*. 67(1):68–75

42. Larsen MT, Kuhlmann M, Hvam ML, Howard KA. 2016. Albumin-based drug delivery: harnessing nature to cure disease. *Mol Cell Ther*. 4:

43. Alam K, Farasyn T, Ding K, Yue W. 2018. Characterization of Liver- and Cancer-type-Organic Anion Transporting Polypeptide (OATP) 1B3 Messenger RNA Expression in Normal and Cancerous Human Tissues. *Drug Metab Lett*. 12(1):24–32

44. Silva ZS Jr, Bussadori SK, Fernandes KPS, Huang Y-Y, Hamblin MR. 2015. Animal models for photodynamic therapy (PDT). *Bioscience Reports*. 35(6):

45. Branford S, Rudzki Z, Walsh S, Parkinson I, Grigg A, et al. 2003. Detection of BCR-ABL mutations in patients with CML treated with imatinib is virtually always accompanied by clinical resistance, and mutations in the ATP phosphate-binding loop (P-loop) are associated with a poor prognosis. *Blood*. 102(1):276–83

46. Venkatesan S, Swanton C, Taylor BS, Costello JF. 2017. Treatment-Induced Mutagenesis and Selective Pressures Sculpt Cancer Evolution. *Cold Spring Harb Perspect Med*. 7(8):a026617

47. Stuart-Harris R, Caldas C, Pinder SE, Pharoah P. 2008. Proliferation markers and survival in early breast cancer: a systematic review and meta-analysis of 85 studies in 32,825 patients. *Breast*. 17(4):323–34

48. de Azambuja E, Cardoso F, de Castro G, Colozza M, Mano MS, et al. 2007. Ki-67 as prognostic marker in early breast cancer: a meta-analysis of published studies involving 12,155 patients. *Br J Cancer*. 96(10):1504–13

49. Abubakar M, Orr N, Daley F, Coulson P, Ali HR, et al. 2016. Prognostic value of automated KI67 scoring in breast cancer: a centralised evaluation of 8088 patients from 10 study groups. *Breast Cancer Res*. 18:104

50. Yang M, Antoine DJ, Weemhoff JL, Jenkins RE, Farhood A, et al. 2014. Biomakers distinguish apoptotic and necrotic cell death during hepatic ischemia-reperfusion injury in mice. *Liver Transpl*. 20(11):1372–82

51. Sher Y-P, Hung M-C. 2013. Blood AST, ALT and UREA/BUN Level Analysis. *Bio-protocol*. 3(19):e931–e931

52. Harrod-Kim P. 2006. Tumor Ablation with Photodynamic Therapy: Introduction to Mechanism and Clinical Applications. *Journal of Vascular and Interventional Radiology*. 17(9):1441–48

53. Suzuki T, Tanaka M, Sasaki M, Ichikawa H, Nishie H, Kataoka H. 2020. Vascular Shutdown by Photodynamic Therapy Using Talaporfin Sodium. *Cancers (Basel)*. 12(9):E2369

54. Baell JB, Holloway GA. 2010. New Substructure Filters for Removal of Pan Assay Interference Compounds (PAINS) from Screening Libraries and for Their Exclusion in Bioassays. *J. Med. Chem.* 53(7):2719–40

55. Pfaff E, Schwenk M, Burr R, Remmer H. 1975. Molecular Aspects of the Interaction of Bromosulfophthalein with High-Affinity Binding Sites of Bovine Serum Albumin. *Mol Pharmacol*. 11(2):144–52

56. Chen Q, Feng L, Liu J, Zhu W, Dong Z, et al. 2016. Intelligent Albumin-MnO2 Nanoparticles as pH-/H2 O2 -Responsive Dissociable Nanocarriers to Modulate Tumor Hypoxia for Effective Combination Therapy. *Adv. Mater. Weinheim*. 28(33):7129–36

57. Zhang Q, Li L. 2018. Photodynamic combinational therapy in cancer treatment. *J BUON*. 23(3):561–67

58. Young M, Suddard-Bangsund J, Patrick TJ, Pajares N, Traverse CJ, et al. 2016. Organic Heptamethine Salts for Photovoltaics and Detectors with Near-Infrared Photoresponse up to 1600 nm. *Advanced Optical Materials*. 4:1028–33

59. Traverse CJ, Chen P, Lunt RR. 2018. Lifetime of Organic Salt Photovoltaics. *Advanced Energy Materials*. 8(21):1703678

60. Zhang G-L, Zhang Y, Cao K-X, Wang X-M. 2019. Orthotopic Injection of Breast Cancer Cells into the Mice Mammary Fat Pad. *J Vis Exp*

CHAPTER 4.

ADDITIONAL STUDIES

4.1 Introduction

The following data are included to supplement experiments discussed in previous chapters, as well as summarize inconclusive experiments from the thesis work. These studies are contained within a separate chapter because the experiments were inconclusive, preliminary and not reproduced, or yielded null results. Follow up experiments could be performed for some of the studies, but overall they were considered to be outside the realm of the core thesis work.

4.2 Organic salts in a normal breast cancer cell line

To determine preferential uptake and toxicity of organic salts for cancer cells, cell viability and uptake assays were performed in normal human breast epithelial MCF10A cells. MCF10A cells were purchased from ATCC and maintained in Brugge media (**Table S4.1**). The MCF10A cell line was derived from proliferative breast cancer tissue, is nontumorgenic, and one of the most commonly used *in vitro* breast cell models (1). Cells were treated with the indicated organic salt and 526 mW/cm^2 of 850 nm light over 3 days. Cell viability is reported as cell number on day 4. Absolute quantitative differences from human breast cancer MDA-MB-231 cells are difficult to directly compare due to the slower growth rate of the MCF10A cells, however the relative changes in growth inhibition are similar (**Figure 4.1A-B**). Cancer and normal breast cell lines treated with $CyPF_6$ and CyFPhB display 100% inhibition from the dark control with NIR light excitation. MCF10A cells do appear to be more resistant to CyTPFB with NIR irradiation, but these results would require additional experiments to determine that this result was not due to technical error and is reproducible. This would also need to be performed at a range of concentrations to determine dose response and IC_{50} values.

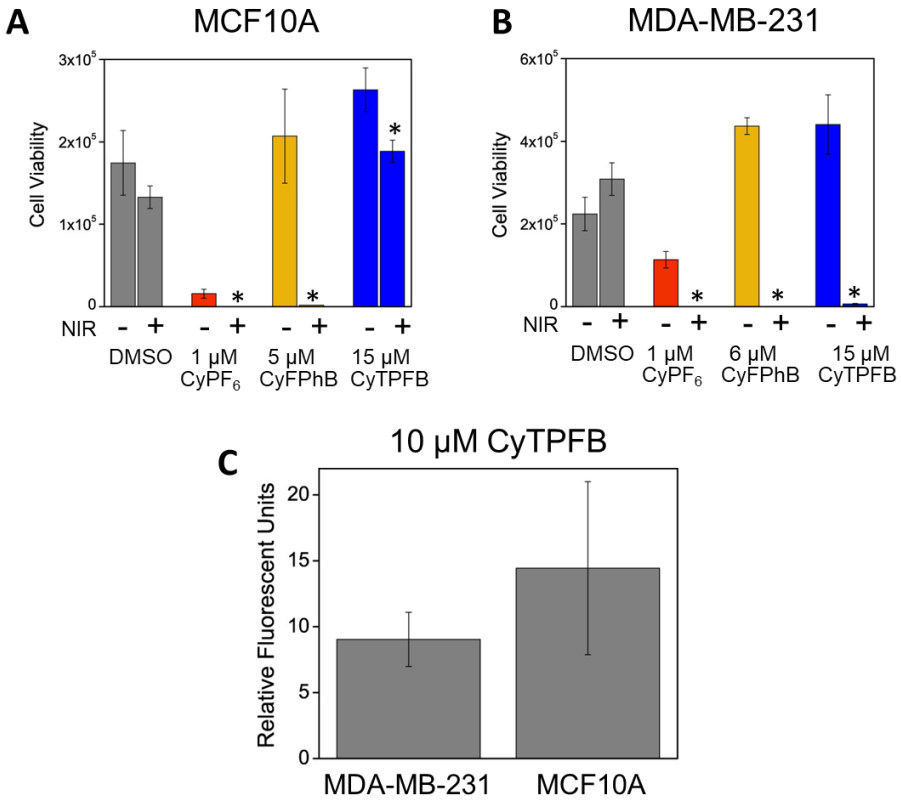

Figure 4.1 Organic salts in human breast epithelial cell lines. Cells were incubated in the indicated concentrations of organic salts with or without NIR excitation for 4 days. On day 4 cell viability was measured by cell count with trypan blue exclusion. (**A**) Normal human breast epithelial MCF10A cells display similar toxicity trends as MDA-MB-231 cancer cell lines. (**B**) Human breast cancer MDA-MB-231 cells are provided as a comparison for MCF10A cells. (**C**) MCF10A and MDA-MB-231 display similar levels of intracellular fluorescence. Data are displayed as means ± S.D., n = 3. Statistically significant differences (p-value < 0.05) are marked with asterisks (*).

Cell viability data is corroborated by organic salt uptake measured by intracellular fluorescence. MDA-MB-231 and MCF10A cells were incubated in 15 μM CyTPFB over 24 hours before fluorescence intensity was measured with a Leica fluorescent microscope using 740 nm excitation and a Cy7 filter cube. Differences in fluorescent signal are not statistically significant (**Figure 4.1C**). OATP1B1/3 has also been shown to be expressed in human epithelial breast tissue, so this effect is not entirely unexpected

or unexplainable (2). It should also be noted that experiments using MCF10A cells were difficult to reproduce consistently. This could potentially be attributed to changes in cell cycle when measurements were made, as normal cell lines display a regular cell cycle that regulates uptake of biomolecules (3). Further experiments should proceed with a more stringent protocol in response to time from cell thawing to experimental initiation, number of cell passages, and shorter experimental timelines for more consistent data. There were also problems culturing the MCF10A cells for more than 3 passages, cells began to undergo morphological changes and slower growth rates as experiments progressed. MCF10A cells also require 15-20 minutes at 37°C incubation with 0.05% trypsin to detach from the culture plate, and 25-30% of cells remain on the plate. This has affected reproducibility and confidence in results, and optimal culturing standards would need to be developed prior to any further in-depth analysis with this cell line. Overall, it was decided these *in vitro* experiments were too artificial to characterize tumor specific uptake, and studies were moved to a more relevant *in vivo* system using a mouse orthotopic cancer model.

4.3 Antioxidant rescue studies

Studies with antioxidant supplementation were performed *in vitro* to determine if the toxicity from organic salt phototherapy could be rescued with the addition of reactive oxygen species (ROS) scavengers. In Chapter 2 I discussed the correlation of mitochondrial ROS generation to phototoxicity in human lung carcinoma A549 cells, which is well supported by existing literature (4). Therefore, it is reasonable to hypothesize that antioxidant supplementation should reduce phototoxicity.

Initial studies were performed in human lung carcinoma A549 cells with N-acetylcysteine (NAC, Sigma-Aldrich A7250), a glutathione (GSH) precursor known to attenuate oxidative stress by reducing disulfide (S-S) bonds, scavenging ROS, and inactivate reactive electrophiles (5, 6). Antioxidant rescue studies were performed following the same protocol for *in vitro* cell viability studies described above, except with the addition of antioxidants to the cell media throughout the experiment. Studies were initially done with CyTPFB as the ROS-inducing photosensitizer, as it displays lower potency than other photosensitizers and it may be easier to observe a rescue effect. Early studies with 7.5 µM and 15 µM CyTPFB did not show any changes to cellular viability with increasing levels of NAC (**Figure 4.2A-B**). When no effect was observed with NAC, studies were done with glutathione monoethyl ester (GSH, Sigma-Aldrich 353905), a cell permeable derivative of reduced glutathione (7). No effect was observed with increasing levels of GSH with 7.5 µM or 15 µM CyTPFB (**Figure 4.2C-D**).

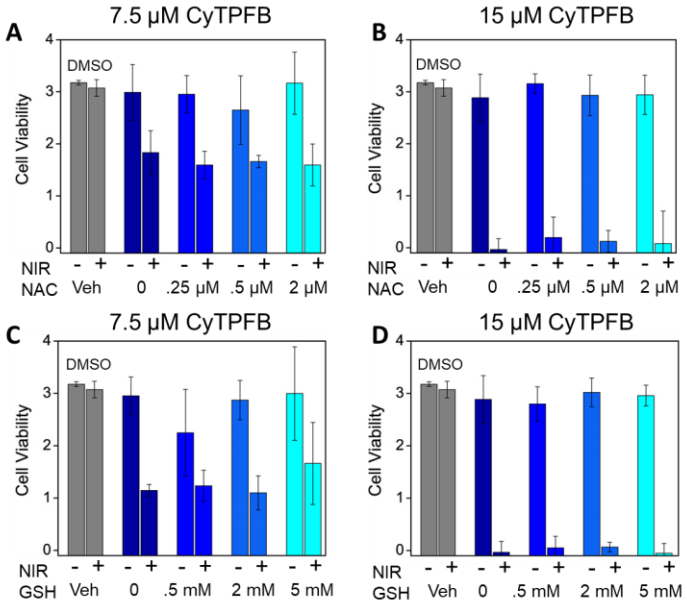

Figure 4.2 Antioxidant supplementation does not lead to a rescue effect in PDT studies with CyTPFB in A549 cells. A549 cells were incubated with increasing conc-

Figure 4.2 (cont'd)

centrations of (**A**, **B**) N-acetylcysteine (NAC) or (**C**, **D**) cell permeable glutathione (GSH) with the indicated concentration of CyTPFB with or without NIR excitation for 4 days. Cell viability is represented as cell doublings per day. There are no statistically significant differences in cytotoxicity or phototoxicity with antioxidant supplementation. Data are displayed as means ± S.D., n = 3. Statistically significant differences (p-value < 0.05) are marked with asterisks (*).

Following the null results in CyTPFB treated A549 cells, later studies were performed using 1.2 µM $CyPF_6$, however with only two light treatments with half the light dosage typically performed (263 mW/cm^2). NAC levels used previously with CyTPFB were too low and levels were increased to 4.2 mM NAC pre-light treatment incubation, 700 µM NAC continuous incubation during the experiment, or 4.2 mM NAC post-light treatment incubation. Early results indicate that there may be a reduction in phototoxicity in A549 cells pre-treated with 4.2 mM NAC prior to light treatment (**Figure 4.3A**). Higher dosages were not used because above 5 mM NAC morphological changes were noticed in the cells. This affect is minor, but optimizations to organic salt dosage, light dosimetry, and timing of treatments may lead to a more significant response.

In Chapter 2, flow cytometry data showed that phototherapy with organic salts generate mitochondrial specific ROS. Therefore, I utilized a mitochondrial targeted antioxidant to directly reduce ROS levels that are driving phototoxicity. Mito-Tempo combines an antioxidant piperidine nitroxide (Tempo) group with a cationic triphenylphosphonium (TPP^+) group which targets the molecule to the mitochondria. Mito-Tempo has been shown to selectively reduce levels of mitochondrial specific ROS (8). Cell viability assays were performed with 1.2 µM $CyPF_6$ and 3 526 mW/cm^2 light

treatments with increasing levels of Mito-Tempo. No results were statistically significant but increasing levels of Mito-Tempo trended with increased cytotoxicity (**Figure 4.3B**). This could be due to mitochondrial-targeting by both Mito-Tempo and $CyPF_6$, which could interfere with electron transport and induce more mitochondrial ROS generation, leading to increased cytotoxicity. Incubation with Mito-Tempo also has the potential to interfere with mitochondrial targeting, when cells were incubated with Mito-Tempo there is shown to be an increase in mitochondrial ROS as measured by MitoSOX using flow cytometry (**Figure 4.3C**). Due to these confounding variables this experimental route was abandoned.

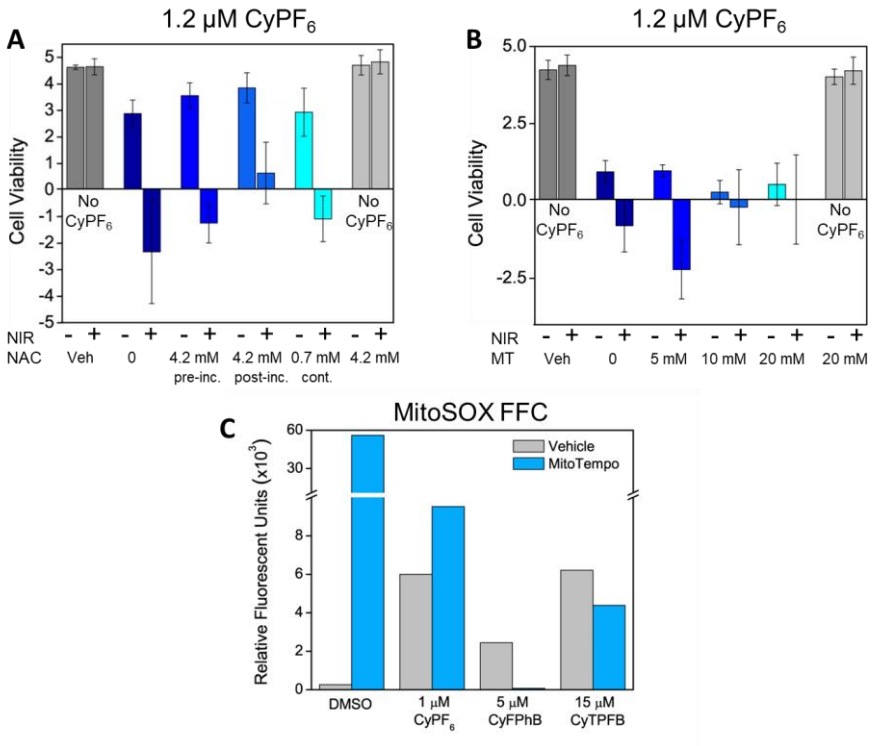

Figure 4.3 Antioxidant supplementation does not lead to a rescue effect in PDT studies with $CyPF_6$ in A549 cells. A549 cells were incubated with increasing concentrations of N-acetylcysteine (NAC) or MitoTempo (MT) and treated with 1.2 μM $CyPF_6$ with or without NIR excitation. Cell viability is reported as cell doublings per day. (**A**) Cells were incubated with 0.7mM NAC throughout treatment, 4.2 mM NAC 24 hours prior to treatment (pre-inc), or 4.2 mM NAC 24 hours after treatment (post-inc).

Figure 4.3 (cont'd)

There is a statistically significant difference in cells pre-incubated with 4.2 mM NAC prior to treatment (**B**) Supplementation of a Mito-Tempo (MT) throughout $CyPF_6$ treatment does not result in a statistically significant difference in cytotoxicity or phototoxicity. Data are displayed as means ± S.D., n = 3. (**C**) Preliminary fluorescence flow cytometry (FFC) results show that incubation with 5mM MitoTEMPO increases MitoSOX fluorescence in A549 cells treated with a DMSO vehicle.

In the preliminary studies discussed above no convincing rescue effect with antioxidants was observed. Promising early results observed with high levels of NAC pre-incubation before light treatment with $CyPF_6$ could be expanded upon with more organic salts, a range of dosages, and ROS quantification. One of the hurdles to this study may be determining appropriate dosages and incubation times to have an adequate reducing pool to inhibit ROS generation and diminish phototoxicity. Mass spectrometry could be used to quantitate intracellular antioxidant levels, determining optimal time points to observe a more robust oxidative stress response. It is also possible this mitochondrial localized effect may be too potent to be significantly mitigated with exogenous antioxidant supplementation. Cell viability studies with lower dosages of organic salts and light treatments could be employed. Alternatively, the CRISPR-cas system could be used to knock down superoxide dismutase, glutathione reductase, catalase, or other cellular antioxidant proteins to enhance phototoxicity.

4.4 Papillary mouse model studies

Early *in vivo* photodynamic therapy studies were performed in a MMTV-Myc mouse tumor model. Orthotopic mammary tumors were generated by the implantation of a tumor chunk derived from the MMTV-Myc papillary and epithelial-mesenchymal-transition (EMT) histological subtypes into the 4^{th} mammary fat pad of 8-week-old FVB

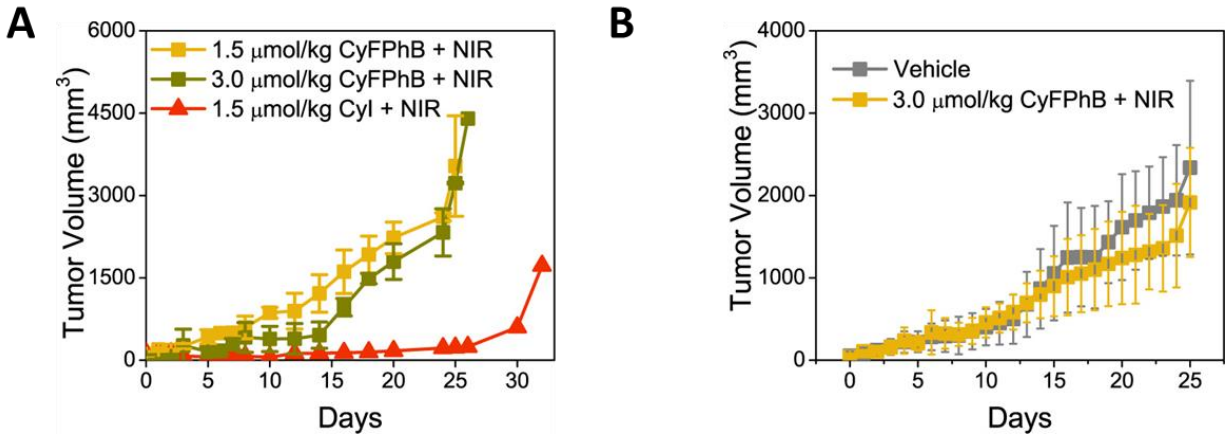

Figure 4.4 Photodynamic therapy studies in a papillary tumor model. No difference observed in tumor growth with 1.5 µmol/kg $CyPF_6$ (n=1) with NIR light (20 J/cm^2). There appears to be a delay in growth, but the tumor did not fully establish and begin growing until day 16. No difference observed in tumor growth with 1.5 (n=3), 3 (n=2), or 5 (n=3) µmol/kg CyFPhB with NIR light (20 J/cm^2). Data are displayed as means ± S.D.

mice (9). EMT tumors did not display tumor specific accumulation of 1.17 µmol/kg CyI or CyFPhB delivered intraperitoneally when tumor volume was approximately 40 mm^2. Tumor specific accumulation was observed in the papillary tumor model, as shown in Chapter 2. However, no changes were observed in tumor growth or appearance following intravenous injection of 1.5 µmol/kg CyI, 1.5 µmol/kg CyFPhB, 3 µmol/kg CyFPhB or 5 µmol/kg CyFPhB and NIR light treatment (**Figure 4.4A-B**). There appears to be a delay in growth in the CyI + NIR tumor, but this is due to an error in tumor implantation which delayed tumor establishment in the 4th mammary fat pad. Once a palpable tumor formed it progressed at the same rate as the other tumors in the study. This papillary tumor model was used in early optimization studies and null results could be due to a number of factors. This PDT regimen only underwent a single IV dose of the organic salt on day 5 and a single light treatment 24 hours later, compared to later optimized studies that underwent 2 courses of PDT treatment as discussed in Chapter

3. Additionally, early PDT studies utilized a low power LED light system which only generated 20 J/cm^2 over 20 minutes of irradiation with 850 nm light. Light intensity assessments also showed a high degree of variability from the LED lamp used for NIR tumor irradiation. Follow-up studies could be performed with the 150 J/cm^2 light dosage utilized in the 6DT1 mouse model discussed in Chapter 3, but these studies would be unlikely to yield any new data of significant interest.

4.5 Cellular uptake of organic salt nanoparticles

Early experiments with a transmission electron microscope (TEM) were used to detect intracellular levels of organic salts prior to procurement of a fluorescent microscope with NIR imaging capabilities. Initial energy dispersive x-ray microanalysis (EDS) studies were performed on organic salt precipitates by Dr. Fan using a JEOL 2200FS ultra-high resolution transmission electron microscope. For elemental analysis, an electron beam is sent into the sample and chemical elements are identified by a characteristic X-ray spectrum. This technique is not quantitative, and primarily used to elucidate chemical composition in material science studies (10). Brightfield images were generated using an omega filter to identify regions of interest. Organic salt precipitates were affixed on lacy carbon grids for elemental analysis to determine composition. Chlorine signal was used to identify the cation and fluorine or iodide to identify the anion (**Table S4.2**). Both the cation and the anion are present in CyI and CyTFM particles (**Figure 4.5, Table S4.3, Table S4.4**).

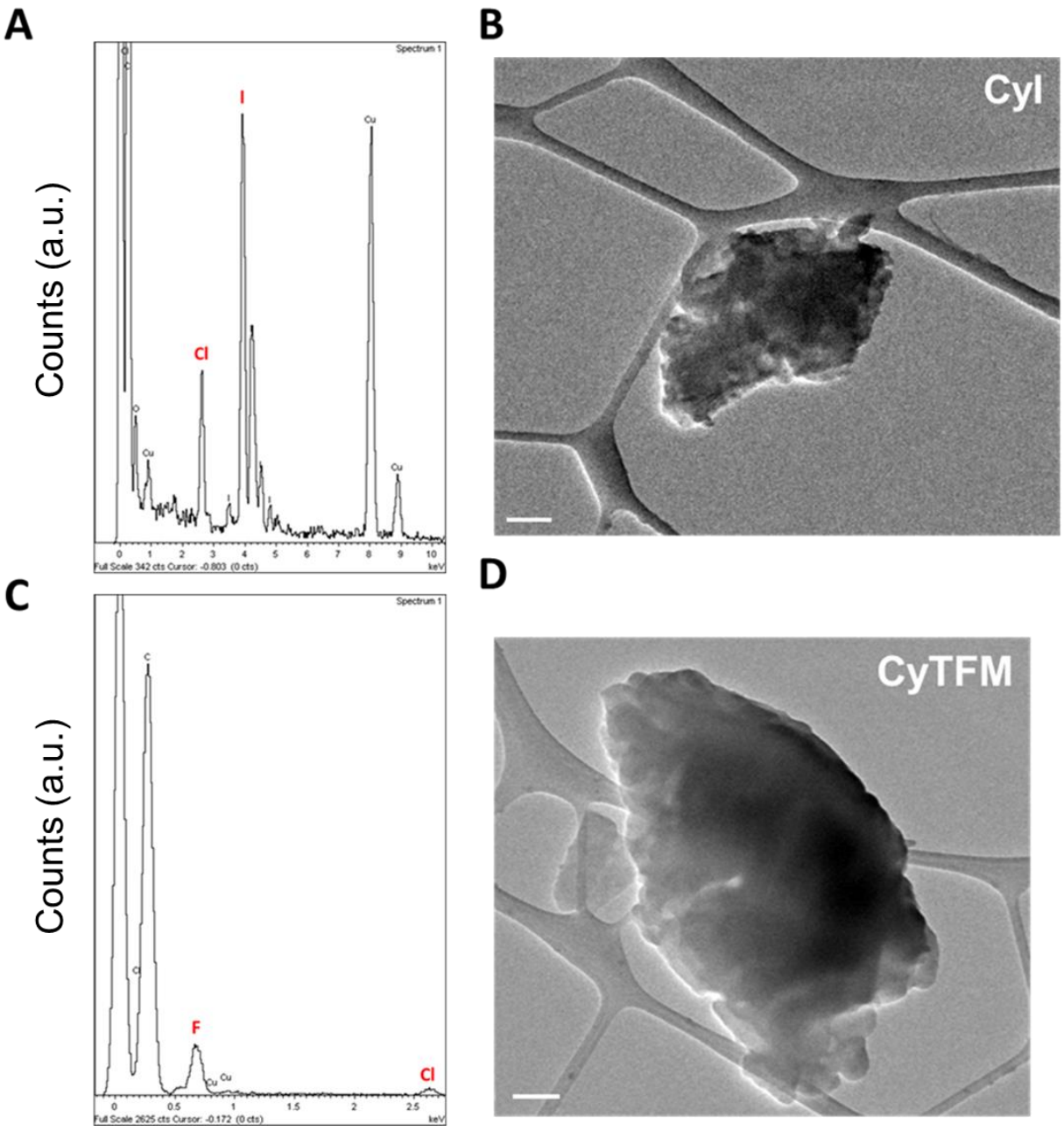

Figure 4.5 TEM-EDS of organic salt particle mounted on lacy carbon grid. (**A**) Elemental spectra of CyI particle. Representative elemental analysis shows that nanoparticle composition includes chlorine (representative element from the Cy^+ cation) and I (representative element from I^- anion). (**B**) Brightfield image of CyI particle. (**C**) Elemental spectra of CyTFM particle. Representative elemental analysis shows that nanoparticle composition includes chlorine (representative element from the Cy^+ cation) and F (representative element from the TFM^- anion). (**D**) Brightfield image of CyTFM particle on lacy carbon grid. Inset = 200 nm.

For intracellular studies, human lung carcinoma A549 cells were incubated for 24 hours with 7.5 µM CyTPFB or an equal volume of vehicle dimethyl sulfoxide (DMSO). Cultured cells were dissociated from tissue culture plates with trypsin and centrifuged to generate a 2 cm cell pellet. Cell pellets were fixed with 2.5% glutaraldehyde for 15

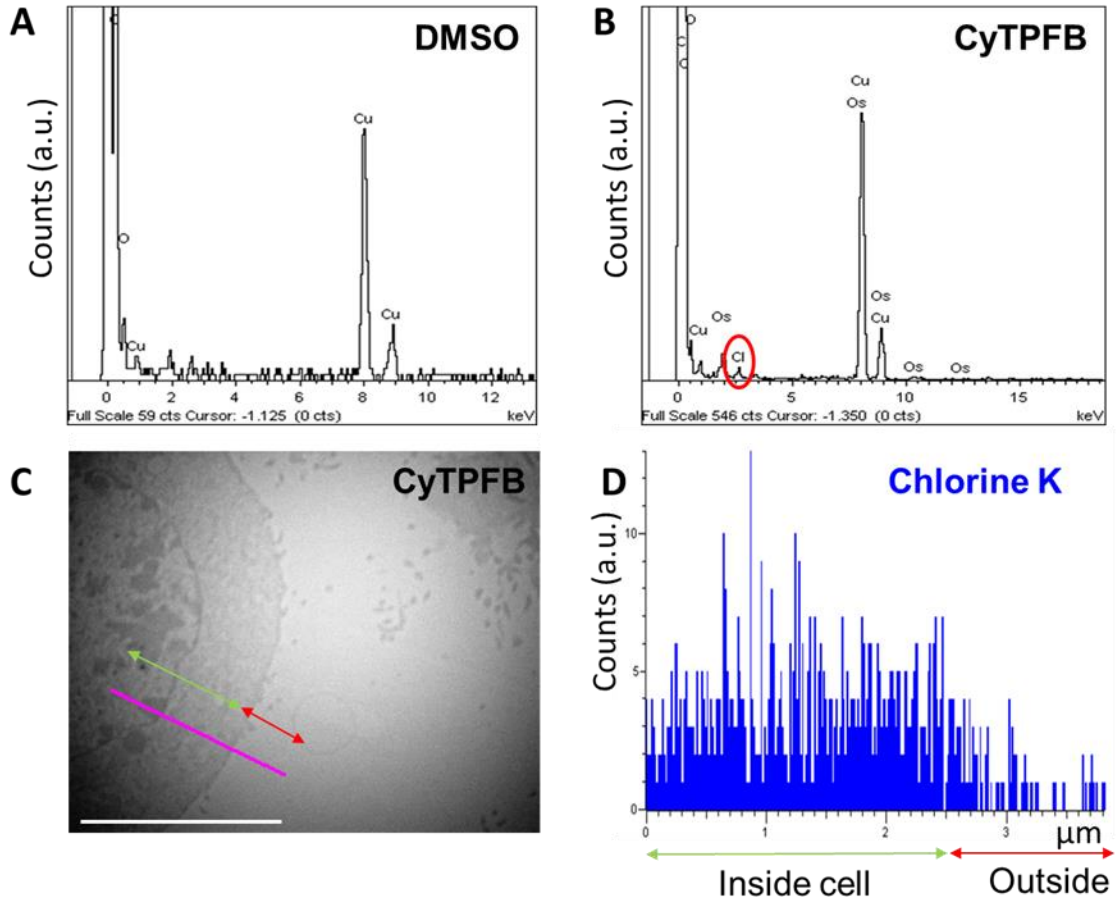

Figure 4.6 TEM-EDS detection of intracellular CyTPFB in an A549 cell. (**A**) Elemental spectra of DMSO treated A549 cells do not display detectable levels of chloride, which is used to identify the presence of Cy^+. (**B**) Elemental spectra of A549 cells incubated with 7.5 µM CyTPFB show detectable levels of intracellular chlorine, confirming the presence of Cy^+. (**C**) Brightfield image of A549 cell with representative line scan for EDS measurements. Inset = 4 µm (**D**) Representative detection counts of chlorine from line scan show that there is an increase within the cellular environment.

minutes at room temperature and stored at 4 degrees. The MSU Center for Advanced Microscopy (CAM) generated 100 nm width sections, stained samples with uranyl

acetate, and fixed them on copper grids for imaging analysis. Brightfield images were used to identify cells and their organelles such as the mitochondria and nucleus. Cells incubated with CyTPFB show increased intracellular levels of chloride (**Figure 4.6**). Chloride was not detectable in cells incubated in the DMSO vehicle control.

These experiments ran into several complications, leading to a shift to an orthogonal method. Initially, staining with lead citrate and uranyl acetate provided the best contrast for brightfield imaging, however the lead (Pb) peak for elemental analysis overlays the Cl peak, inhibiting the detectable signal. Cell pellet sections stained with only uranyl acetate displayed poor resolution to accurately identify unique cellular morphology and the elemental levels of interest remain at lower level of detection. Additional problems with the beam intensity required to accurately be perform EDS also inhibited elemental mapping, as the accelerating voltage necessary to differentiate low level atomic signals (> 200 kV) destroyed the sample (11) . Furthermore, detection of chlorine was possible to identify the cation, but fluorine detection for the anion was not due to peak overlap with intracellular oxygen. Fluoride is also a difficult element to detect using EDS due to its low atomic number (10). For sample processing, glutaraldehyde fixation retains most proteinaceous cellular structures, but poorly retains non-directly crosslinked molecules such as lipids during the subsequent dehydration steps. Glutaraldehyde also makes molecular visualization difficult in tissue due to strong covalent interactions with small molecules of interest and limits electron probe diffusion (12, 13). Lastly, visualization of lipophilic materials of this size is extremely difficult without a heavy metal core due to limited electron density. Collectively, due to the high degree of background, difficulty of detection of atoms of interest, and poor intracellular

resolution it was decided to utilize mass spectrometry for intracellular quantification of organic salts. While mass spectrometry does not allow for elemental mapping at distinct cell areas, it is a more sensitive and quantitative method.

Organic salt quantification by high performance liquid chromatography coupled mass spectrometry (HPLC-MS) shows A549 intracellular concentrations of both the cationic cyanine and the weakly coordinating phenyl borate counterions in A549 cells (**Figure 2.16**). Detection of small hard counterions (I^-, SbF_6^-, PF_6^-) is not possible because they do not bind to a C18 column and are eluted in the salt wash, as high-level salt solutions cannot be sent to the mass spectrometry detector. However, the phenyl borate counterions are easily detectable with this method and shown to be taken up by the cancer cell. The exact mass spectrometry method to quantitate intracellular organic salts is discussed extensively in Chapter 2. There are lower intracellular concentrations of Cy^+ measured for small hard anions, however this could be due to passive toxicity without light irradiation causing a loss of membrane integrity prior to extraction. Organic salts with a lower dark IC_{50} ($CyPF_6$ = 0.9 µM, $CySbF_6$ = 0.9 µM, CyI = 1.0 µM) may experience cell leakage, leading to lower intracellular concentrations. Organic salts with a higher dark IC_{50} are less likely to experience membrane permeabilization (CyTPFB = 19.7 µM, CyFPhB and CyCoCB possess dark IC_{50} values > 20 µM which were extrapolated from observed experimental values, and CyTFM and CyTRIS and did not display a cytotoxic trend at the concentrations evaluated in A549 cells) (**Table S2.4**). While this method does not provide intracellular visualization as seen with EDS-TEM it is less artificial, quantitative, and reproducible.

The uptake of organic salt nanoparticles was also characterized by intracellular UV-vis spectroscopy. As demonstrated in Chapter 2, in aqueous solution organic salts self-organize to form stable nanoparticles, which have been categorized based on size, charge, solubility, chemical stability, and composition. Nanoparticle stability is monitored by UV-vis, identified by hypsochromic and bathochromic shifts in the absorption spectra as compared to the monomeric peak. To determine whether this shift was detectable within the cellular environment, cells were incubated for 24 hours in 1 μM $CyPF_6$, 5 μM CyFPhB, or 15 μM CyTPFB. After trypsin dissociation the cells were resuspended in Hank's buffered salt solution with 2% fetal bovine serum and analyzed using UV-vis spectroscopy (**Figure 2.6**). Due to a high degree of background noise distinct shifts are difficult to characterize, nevertheless, CyFPhB and CyTPFB show a secondary local maxima peak at 764 nm that is not seen with $CyPF_6$. This indicates nanoparticles are present in the cellular environment.

While this data is not irrefutable, at the time of analysis these were the best technical options available. Intracellular elemental analysis tracking has been performed with other nanomaterials in the field, but this technique is generally used with larger nanomaterials with a heavy metal composition that are stable to glutaraldehyde fixation and easily distinguishable from the intracellular environment. The organic salt nanoparticles characterized in this study are small (5-10 nM) and highly lipophilic. This size and lack of easily detectable heavy metal composition makes them biocompatible and ideal for biological applications, but difficult to image with TEM (14). Further intracellular imaging experiments could be attempted at a higher magnification but attempts to couple this with EDS are unlikely to be successful or representative of the

biological environment. Higher resolution results may be possible using freeze-fracture or cryogenic TEM. To elucidate nanoparticle position within cells a superior method would be high resolution confocal fluorescence microscopy at NIR wavelengths.

I have shown that similar amounts of photoactive cation and anions are detectable by mass spectrometry in cellular extracts and that there are shifts in the absorption spectra within live cells. Further experimentation into this route was abandoned due to inconclusive data and the potential that for solid cancer analysis *in vivo*, cellular uptake of organic salt nanoparticles may not necessarily lead to more efficacious antitumor therapy.

APPENDIX

Component	Volume
DMEM/F12	415 mL
Fetal Bovine Serum	75 mL (15%)
EGF (100ug/mL stock)	100 uL (20ng/mL)
Hydrocortisone (1mg/mL stock)	250 uL (0.5 mg/mL)
Cholera toxin (1 mg/ml stock)	50 uL (100ng/mL)
Insulin (10mg/mL stock)	500uL (10ug/mL
Glutamine (stock)	5 mL
Pen/Strep (100x stock)	5 mL

Table S4. 1 Brugge media recipe for culturing MCF10A cells.

	Cation	Anion	Cl	I	F
No dye	NA	NA			
CyI	$C_{42}H_{44}N_2Cl$	I	X	X	
CyTPFB	$C_{42}H_{44}N_2Cl$	$C_{24}BF_{20}$	X		X
CyTFM	$C_{42}H_{44}N_2Cl$	$C_{32}BH_{12}F_{24}$	X		X

Table S4. 2 Theoretical cation and anion elements detectable by TEM-EDS.

Element	Weight %	Atomic %
O K	5.94	28.81
Cl K	8.69	19.01
I L	85.37	52.18

Table S4. 3 Experimental CyI elements detected by TEM-EDS.

Element	Weight %	Atomic %
C K	91.48	94.67
F K	7.72	5.05
Cl K	0.79	0.28

Table S4. 4 Experimental CyTFM elements detected by TEM-EDS.

REFERENCES

REFERENCES

1. Qu Y, Han B, Yu Y, Yao W, Bose S, et al. 2015. Evaluation of MCF10A as a Reliable Model for Normal Human Mammary Epithelial Cells. PLOS ONE. 10(7): e0131285

2. Buxhofer-Ausch V, Secky L, Wlcek K, Svoboda M, Kounnis V, et al. 2013. Tumor-Specific Expression of Organic Anion-Transporting Polypeptides: Transporters as Novel Targets for Cancer Therapy. J Drug Deliv. 2013:863539

3. Patel P, Kansara K, Senapati VA, Shanker R, Dhawan A, Kumar A. 2016. Cell cycle dependent cellular uptake of zinc oxide nanoparticles in human epidermal cells. Mutagenesis. 31(4):481–90

4. Zhou Z, Song J, Nie L, Chen X. 2016. Reactive oxygen species generating systems meeting challenges of photodynamic cancer therapy. Chem. Soc. Rev. 45(23):6597–6626

5. Ezeriņa D, Takano Y, Hanaoka K, Urano Y, Dick TP. 2018. N-Acetyl Cysteine Functions as a Fast-Acting Antioxidant by Triggering Intracellular H2S and Sulfane Sulfur Production. Cell Chem Biol. 25(4):447-459.e4

6. Aldini G, Altomare A, Baron G, Vistoli G, Carini M, et al. 2018. N-Acetylcysteine as an antioxidant and disulphide breaking agent: the reasons why. Free Radical Research. 52(7):751–62

7. Jia Y, Wang H-D, Wang Q, Ding H, Wu H-M, Pan H. 2017. GSH depletion and consequent AKT inhibition contribute to the Nrf2 knockdown-induced decrease in proliferation in glioblastoma U251 cells. Oncol Rep. 37(4):2252–60

8. Du K, Farhood A, Jaeschke H. 2017. Mitochondria-Targeted Antioxidant Mito-Tempo Protects against Acetaminophen Hepatotoxicity. Arch Toxicol. 91(2):761–73

9. Ogrodzinski MP, Teoh ST, Lunt SY. 2021. Targeting Subtype-Specific Metabolic Preferences in Nucleotide Biosynthesis Inhibits Tumor Growth in a Breast Cancer Model. Cancer Research. 81(2):303–14

10. Scimeca M, Bischetti S, Lamsira HK, Bonfiglio R, Bonanno E. 2018. Energy Dispersive X-ray (EDX) microanalysis: A powerful tool in biomedical research and diagnosis. Eur J Histochem. 62(1):2841

11. Egerton RF, Wang F, Crozier PA. 2006. Beam-induced damage to thin specimens in an intense electron probe. Microsc Microanal. 12(1):65–71

12. Hobro AJ, Smith NI. 2017. An evaluation of fixation methods: Spatial and compositional cellular changes observed by Raman imaging. Vibrational Spectroscopy. 91:31–45

13. Migneault I, Dartiguenave C, Bertrand MJ, Waldron KC. 2004. Glutaraldehyde: behavior in aqueous solution, reaction with proteins, and application to enzyme crosslinking. Biotechniques. 37(5):790–96, 798–802

14. Robson A-L, Dastoor PC, Flynn J, Palmer W, Martin A, et al. 2018. Advantages and Limitations of Current Imaging Techniques for Characterizing Liposome Morphology. Frontiers in Pharmacology. 9:

CHAPTER 5.

SUMMARY AND FUTURE DIRECTIONS

5.1 SUMMARY

This dissertation determined how counterion pairing can be used to electronically modify fluorescent organic salts and regulate reactive oxygen species (ROS) generation upon photoexcitation. This research also laid the groundwork for a photosensitizer (PS) development workflow to characterize therapeutic and diagnostic potential on a molecular, cellular, and physiological level. Through my thesis work, I have demonstrated a novel optoelectronic platform to engineer photoactive theranostic agents which will expand their clinical usage in cancer diagnostics and therapy.

The results presented here outline my research contributions to advance clinical photoactive agents, which are summarized in Chapter 1 and published in *Annual Reviews in Biomedical Engineering*. In Chapter 2, I have characterized organic salts and found that pairing a photoactive heptamethine cation with a weakly coordinating anion induces self-organizing nanoparticle formation, maintaining ion interaction in solution and cellular environments. Nanoparticles exhibit similar shifts in redox potential and zeta potential that reflect changes in frontier molecular orbitals. The use of molecular self-assembly to generate nanoparticles with tunable electronic properties for biomedical applications was previously unexplored in aqueous and cellular environments. In human lung carcinoma cell lines (A549), organic salts were found to localize within mitochondria, generate differential levels of ROS, and display a spectrum of toxicity based on anion pairing. Shifts in energy level modulation were found to correlate to phototoxicity, establishing counterion modulation as a means to control cellular toxicity. This modality was previously unexplored in the existing biomedical

literature and had only been extensively studied in photovoltaics (Chapter 2, published in *Scientific Reports,* U.S. Patent No. 6550-000311).

In Chapter 3, I expanded on initial studies in human cancer cell lines in a metastatic breast cancer mouse model. *In vivo* findings establish the clinical relevance of counterion tuning, revealing that a heptamethine cyanine cation paired with a selectively phototoxic aryl borate anion can abolish tumor growth upon light excitation. Photoexcitation induces tumor necrosis at the site of light irradiation with minimal cytotoxic effects to normal tissue. The use of a self-assembled nanoparticle to reduce off-site cytotoxicity in an *in vivo* model was previously unexplored in the literature. Additionally, I examined the role of organic anion transporter proteins and their role in photosensitizer uptake. There is evidence in the literature that OATPs are the primary mediators of cancer cell accumulation of small molecule photosensitizing agents. My results have also implicated albumin-mediated uptake as a potential mechanism which merits further investigation.

Collectively, these studies discovered that counterion tuning can modulate valence energy levels of organic salt nanoparticles in solution to influence generation of ROS and enhance photodynamic therapy (PDT) in a translational animal model of cancer. The knowledge gained through this work will advance photoactive agents and expand their use in the treatment and diagnosis of cancer. Furthermore, this research establishes a foundational optoelectronic tuning platform, which can be used in future investigations of additional PSs and translational cancer models.

5.2 FUTURE DIRECTIONS

5.2.1 Exploration of additional fluorescent organic salts

Having established a counterion platform to independently tune toxicity independent of optical properties, we can now utilize it to generate optimized PSs for clinical diagnostics and therapy. This work was primarily accomplished with a base heptamethine cyanine, which can be covalently modified to generate a fluorophore with more ideal optical properties for even deeper tissue. Cyanines are well-characterized fluorescent molecules, and the effects of their structural alterations are well established in the literature (1). Adjustments to headgroups, changes to the central methane position, and alkyl groups can increase the rigidity to the fluorophore, which will increase quantum yield by limiting vibrational freedom (2). The central methane position is typically occupied by a halide to increase rigidity. For my thesis studies, I utilized a heptamethine cyanine with a chloro-cyclohexyl moiety within the methine bridge; however, this cyanine only displays modest a Stokes shift (wavelength difference between excitation and emission maxima) of 20-30 nm. Alternative electron donating/withdrawing nitrogen groups can be substituted at this position to generate large Stokes shifts greater than 120 nm. This modification also blue-shifts the absorption peak, but this can be compensated for by using base cyanines with extended methine bridges to have a deeper NIR absorbance. Additionally, introduction of asymmetric electronic structures has been shown to increase cyanine Stokes shifts and red shift absorption into the NIR range (3). Dr. Babak Borhan is a collaborator to this work and an expert in the synthesis and modification of cyanine dyes, who could design optimized cyanine dyes for deep tissue imaging. Additionally, our lab has a

NIRvana camera with an InGaAs detector capable of imaging NIR-II wavelengths (900–1700 nm), which are capable of penetrating even deeper into biological tissue (4). While there are cyanine dyes that absorb in this range, this also opens exciting new possibilities for alternative and enhanced photoactive compounds.

Cyanines were originally chosen for this work because they are biocompatible and easily modifiable to absorb in the NIR, making them ideal for deep tissue imaging. Further work should expand upon this work in the cationic heptamethine cyanine model by investigating counterion pairing in a broader group of photoactive ions, such as BODIPY, anionic heptamethine cyanine, rhodamines, and phthalocyanine dyes (5–8).

After engineering optimal photoactive ions, Dr. Richard Lunt's group has a wide range of energy modulating counterions. For this work, I primarily used aryl borates but there are alternative counterion groups as well, such as a series of carboranes that have yielded promising results in early studies. Future work should elucidate the counterion chemical properties that drive the shifts in energy levels of the cationic fluorophore. This could be attributed to numerous anionic chemical properties, such as 1) electronic structure, 2) molecular level interface dipoles, 3) steric hindrance, 4) electron withdrawing ability, and 5) reorganization energies for electron transfer. This could be investigated by a series of methodological substitutions on a base aryl borate to understand the impact of different chemical groups on shifts in valence energy levels. Investigating counterion properties and their effects on photoactive ion energy levels will enable future work to pair specific ions more easily to create desired shifts in energy levels and generate phototoxic or nontoxic organic salts. Furthermore, these shifts in energy level can be designed to generate particular types of ROS through resonant

electron transfer. These optimized phototoxic organic salts could potentially be designed to target different cancer antioxidant systems. Potential for application in various cancer lines could be easily screened using the workflow designed in this thesis. This research established a robust workflow for screening photoactive agents from photophysical to physiological attributes. This will allow future work into additional organic salts to proceed rapidly to further generate optimized photoactive agents.

5.2.2 Expansion of *in vivo* studies

The translatability of findings in preclinical models to human medicine is a constant goal in cancer research. One of the benefits of PDT is that it can be broadly applied to a number of cancers and does not rely on exploiting any particular cancer mechanism. Thus, I believe this work will be highly translatable to additional cancer models and human patients. Problems with clinical PDT generally arise from incomplete tumor ablation and recurrence, which is attributed to insufficient light penetrance and low ROS yields within the heterogeneous tumor environment (9). To assess the viability of PDT and my counterion-tuned phototoxic PSs, additional experiments should be done in a more disseminated, deep-seated cancer model. Our lab has begun working with a syngeneic orthotopic murine model of pancreatic cancer, which I believe would be another test for the efficacy of PDT agents. This model would also allow studies in male and female mice, as therapeutic outcomes in my studies have only been assessed in mammary cancer bearing female mice, as the majority of human breast cancer occurs in females. Another potential model would be inoculating immunocompromised mice with isogenic human breast cancer cell lines, such as MDA-MB-231, a highly metastatic breast cancer cell line. While this does offer insight into human disease, it is

worth noting that the high degree of artificiality of the tumor microenvironment without a fully present immune system may not be the best model for therapeutic efficacy in human patients. Alternatively, also available are humanized CD34+ mouse models that have been used to assess oncogenic progression and pharmacological modulation of the human immune system (10). However, they are expensive, difficult to maintain, and the presence of a humanized immune system requires regular validation (11).

In Chapter 3, I report a reduced percentage of metastatic tissue within the lung of PDT treated mice. While these results were not statistically significant due to an outlier in the PDT cohort whose tumor responded completely and immediately after the first light treatment, they should be followed up in future experiments. Additional light treatments were performed on the outlier mouse to maintain experimental consistency, but there was no tumor present. However, upon necropsy at endpoint, this mouse had a significantly higher degree of lung metastasis than the rest of the PDT cohort. In Chapter 1, I discuss certain PDT regimens that induce an inflammatory response to stimulates the innate immune system (12). The subsequent induction of inflammatory mediators and immune cells prime the adaptive immune system and induce systemic antitumor surveillance (13). This effect is more commonly reported and attributed to low fluence rate light irradiation over multiple periods, which adequately primes the immune system against cancer cells to induce a long-term and far-reaching immune response (14). This may have occurred in my experiment with the outlier mouse, as the differential response to therapy and immediate destruction of the tumor did not induce an effective inflammatory response to prime the adaptive immune system, which would curb metastatic progression.

To elucidate the effects of PDT with organic salts on the adaptive immune system, a more appropriate approach may be to study the abscopal effects of PDT on a distant tumor. While the anti-metastatic potential of PSs is the ideal measurement, lung metastasis can only be measured at experimental endpoint or through difficult and expensive imaging techniques, making study design and optimization difficult. I have adopted a noninvasive orthotopic injection method that would allow inoculation of a primary treatment tumor into the right mammary fat pad, and after 5 days inoculation of a second tumor into the left mammary fat pad (15). This will allow the second tumor to be palpable upon initiation of PDT for the first tumor. Only the first tumor will undergo PDT, but indirect effects of PDT and induction of the adaptive immune system could be studied by growth of the second tumor. Promising findings could be confirmed in a metastatic model and extend into a variety of experiments to study the PDT-induced immune response, such as flow cytometry to characterize immune populations within the tumor, metastatic sites, and systemic circulation.

An additional area of *in vivo* PDT which could be expanded on is the toxicological studies. In my research, I assessed long term toxicity, but not acute toxicity. Additionally, I was not able to deduce the underlying cause of observed cytotoxic reactions or identify a measurable biomarker. Mice that receive more than 3 μmol/kg of $CyPF_6$ or CyI perish rapidly, but this occurs too quickly for detection of any specific molecular signal. To further investigate this effect, wildtype mice should be used for expanded toxicology panels with a series of dosages of each organic salt. I have previously attempted to monitor toxicology with specific enzyme assays, but this narrow approach has not proven successful. Therefore, it may be more efficient to pool

biological replicates to obtain a volume large enough to utilize the Veterinary Diagnostic Laboratory which will provide a comprehensive blood chemistry profile that may help elucidate mechanistic insight.

Lastly, in my studies many assays rely upon fluorescent signal intensity to extrapolate uptake of the organic salts. While this is a commonly used technique, and fluorescent tags are standard for localization and temporal assays, interactions with biological components can influence quantum yields. It was verified that albumin binding does not affect quantum yields in solution, but it is not feasible to study this across the range of biological components which could interact with organic salts. Early cellular uptake assays were verified with ultrahigh-performance mass spectrometry (UPLC-MS) (Chapter 2), and this method will need to be applied to *in vivo* models for exact quantification of organic salt levels within tissues of interest. Furthermore, UPLC-MS will allow characterization of breakdown products of PSs. It is still not clear whether decreases in fluorescent signal are indicative of drug clearance, metabolic breakdown, or instability. Therefore, in-depth pharmacokinetic studies only possible with mass spectrometry will be needed to assess serum levels, urinary clearance, metabolic products, and concentrations in organs. These experiments would be straightforward to perform, as I have previously extracted and quantitated organic salts from cell cultures using a UPLC-MS and have extensive experience with tissue extractions.

5.2.3 Active targeting moieties and nanoparticle incorporation

In my studies I established a reliance on organic anion transporter polypeptides (OATPs) and albumin interaction for cancer cell uptake of organic salts. It is also suggested in the literature that inhibition of macropinocytosis can reduce uptake of

cyanine dyes or albumin conjugated drugs; however, this was not replicable in my work (16). Bromosulfophthalein (BSP) is frequently used as competitive inhibitor in assays to determine the influence of OATP-mediated uptake (17, 18). However, BSP is found to interact with a large range of compounds (19, 20). It possesses structural features similar to many pan-assay interference compounds, which are known to yield false positives and interfere with interpretation of numerous screening assays (21). I have attempted to account for this by including an orthogonal approach by increasing OATPs expression with dimethyloxalylglycine (DMOG), which corroborates BSP inhibition results in that there is dependence on OATP-mediated uptake. I also observed tumor specific accumulation *in vivo,* which has historically in the literature been attributed to OATP expression (22). However, OATP expression is poorly represented in mouse models and drug distribution studies in mice often poorly translate to clinical trials, due to differences in OATP expression, primarily in the liver (23–25). If there is a reliance on OATPs for tumor specific accumulation, this model is unlikely to translate appropriately. Furthermore, complete reliance on OATPs is not likely to be adequate for any kind of clinical strategy, and the next steps should likely be incorporation into a stable, lipophilic nanoparticle with active targeting moieties for tumor biomarkers. There will still be disparities in biodistribution, but this will always be an inherent problem in early animal models. However, to assess the efficacy of exploiting an overexpressed tumor receptor, it would be critical that studies are done in patient-derived xenograft models.

In my work, I did not have the opportunity to assess the potential of counterion tuned organic salts for diagnostic purposes. As mentioned above, to truly assess diagnostic potential in human disease, a specific biomarker must be identified and

targeted, which was outside of the realm of this work. However, further research into this matter is critical for full realization of counterion tuning as a photoactive theranostic engineering platform. The cyanine dyes used in this thesis are commonly used for protein tagging and are easily conjugated via alkyl chain to a number of targeting moieties, which I have outlined in Chapter 1. The effect of tumor-targeting moieties on nanoparticle formation is unknown, and inclusion of linker chemistry adds another level of design complexity. Therefore, my recommendation to continue this work for diagnostic purposes would be stable incorporation into lipophilic nanoparticles. This will allow for stable ion pairing and addition of targeting moieties that do not directly interact with organic salts. Using this nanoparticle delivery system and the IVIS imaging core, diagnostic capabilities could be assessed by measuring correlation with luciferase-tagged cancer cells and organic salt fluorescence. The lipophilic environment may have unexpected impacts on quantum yields and will need to be characterized. This model could also be expanded to a multimodal therapeutic platform, combining selectively phototoxic organic salts for PDT, tumor-targeting molecules, and incorporation of chemotherapeutics to synergize PDT effects.

In conclusion, in my thesis work I established and elucidated counterion tuning for optimizing fluorescent organic salts through independent control of optical and electronic properties. This was demonstrated with *in vitro* and *in vivo* cancer models, which I used to thoroughly investigate fluorescence intensity, uptake, biodistribution, phototoxicity, and nonspecific cytotoxicity. This foundational screening workflow can be used to characterize future photoactive agents for cancer therapy and imaging. Additionally, my results expanded the collective knowledge regarding design of

photoactive molecules as well as insight into preclinical PDT. By elucidating how photophysical properties can be leveraged to improve organic salts for cancer therapy, this work will overcome critical barriers that have limited the clinical adoption of photoactive agents. The findings presented in this thesis illustrate the development of innovative light-activated theranostic agents which will advance cancer diagnostics and therapy to combat the global cancer burden and improve patient outcomes.

REFERENCES

REFERENCES

1. Sun C, Du W, Wang B, Dong B, Wang B. 2020. Research progress of near-infrared fluorescence probes based on indole heptamethine cyanine dyes in vivo and in vitro. *BMC Chem*. 14(1):21

2. Levitz A, Marmarchi F, Henary M. 2018. Introduction of Various Substitutions to the Methine Bridge of Heptamethine Cyanine Dyes Via Substituted Dianil Linkers. *Photochem Photobiol Sci*. 17(10):1409–16

3. Ren T-B, Xu W, Zhang W, Zhang X-X, Wang Z-Y, et al. 2018. A General Method to Increase Stokes Shift by Introducing Alternating Vibronic Structures. *J. Am. Chem. Soc.* 140(24):7716–22

4. Suo Y, Wu F, Xu P, Shi H, Wang T, et al. 2019. NIR-II Fluorescence Endoscopy for Targeted Imaging of Colorectal Cancer. *Advanced Healthcare Materials*. 8(23):1900974

5. Kobayashi H, Ogawa M, Alford R, Choyke PL, Urano Y. 2010. New strategies for fluorescent probe design in medical diagnostic imaging. *Chem Rev*. 110(5):2620–40

6. Grimm JB, Muthusamy AK, Liang Y, Brown TA, Lemon WC, et al. 2017. A general method to fine-tune fluorophores for live-cell and in vivo imaging. *Nat Methods*. 14(10):987–94

7. Pliquett J, Dubois A, Racoeur C, Mabrouk N, Amor S, et al. 2019. A Promising Family of Fluorescent Water-Soluble aza-BODIPY Dyes for in Vivo Molecular Imaging. *Bioconjug Chem*. 30(4):1061–66

8. Chen J, Wang Y, Fang Y, Jiang Z, Wang A, Xue J. 2020. Improved photodynamic anticancer activity and mechanisms of a promising zinc(II) phthalocyanine-quinoline conjugate photosensitizer in vitro and in vivo. *Biomed Opt Express*. 11(7):3900–3912

9. dos Santos AF, de Almeida DRQ, Terra LF, Baptista MS, Labriola L. 2019. Photodynamic therapy in cancer treatment - an update review. *Journal of Cancer Metastasis and Treatment*. 5:25

10. Walsh N, Kenney L, Jangalwe S, Aryee K-E, Greiner DL, et al. 2017. Humanized mouse models of clinical disease. *Annu Rev Pathol*. 12:187–215

11. Tanaskovic O, Verga Falzacappa MV, Pelicci PG. 2019. Human cord blood (hCB)-CD34+ humanized mice fail to reject human acute myeloid leukemia cells. *PLoS One*. 14(9):e0217345

12. Mroz P, Vatansever F, Muchowicz A, Hamblin MR. 2013. Photodynamic therapy of murine mastocytoma induces specific immune responses against the cancer/testis antigen P1A. *Cancer Res*. 73(21):6462–70

13. Cecic I, Stott B, Korbelik M. 2006. Acute phase response-associated systemic neutrophil mobilization in mice bearing tumors treated by photodynamic therapy. *Int Immunopharmacol*. 6(8):1259–66

14. Thong PSP, Olivo M, Kho K-W, Bhuvaneswari R, Chin WWL, et al. 2008. Immune response against angiosarcoma following lower fluence rate clinical photodynamic therapy. *J Environ Pathol Toxicol Oncol*. 27(1):35–42

15. Zhang G-L, Zhang Y, Cao K-X, Wang X-M. 2019. Orthotopic Injection of Breast Cancer Cells into the Mice Mammary Fat Pad. *J Vis Exp*

16. Usama SM, Lin C-M, Burgess K. 2018. On the Mechanisms of Uptake of Tumor-Seeking Cyanine Dyes. *Bioconjugate Chem.* 29(11):3886–95

17. Izumi S, Nozaki Y, Komori T, Maeda K, Takenaka O, et al. 2013. Substrate-Dependent Inhibition of Organic Anion Transporting Polypeptide 1B1: Comparative Analysis with Prototypical Probe Substrates Estradiol-17β-Glucuronide, Estrone-3-Sulfate, and Sulfobromophthalein. *Drug Metab Dispos*. 41(10):1859–66

18. Ishida K, Ullah M, Tóth B, Juhasz V, Unadkat JD. 2018. Transport Kinetics, Selective Inhibition, and Successful Prediction of In Vivo Inhibition of Rat Hepatic Organic Anion Transporting Polypeptides. *Drug Metab Dispos*. 46(9):1251-1258

19. Yao D, Liu L, Jin S, Li J, Liu X-D. 2012. Overexpression of multidrug resistance-associated protein 2 in the brain of pentylenetetrazole-kindled rats. *Neuroscience*. 227:283–92

20. Pfaff E, Schwenk M, Burr R, Remmer H. 1975. Molecular Aspects of the Interaction of Bromosulfophthalein with High-Affinity Binding Sites of Bovine Serum Albumin. *Mol Pharmacol*. 11(2):144–52

21. Baell JB, Holloway GA. 2010. New Substructure Filters for Removal of Pan Assay Interference Compounds (PAINS) from Screening Libraries and for Their Exclusion in Bioassays. *J. Med. Chem.* 53(7):2719–40

22. Yang X, Shi C, Tong R, Qian WP, Zhau HE, et al. 2010. Near Infrared Heptamethine Cyanine Dye-Mediated Cancer Imaging. *Clinical Cancer Research*

23. Alam K, Farasyn T, Ding K, Yue W. 2018. Characterization of Liver- and Cancer-type-Organic Anion Transporting Polypeptide (OATP) 1B3 Messenger RNA Expression in Normal and Cancerous Human Tissues. *Drug Metab Lett*. 12(1):24–32

24. Cheng X, Maher J, Chen C, Klaassen CD. 2005. Tissue distribution and ontogeny of mouse organic anion transporting polypeptides (Oatps). *Drug Metab Dispos*. 33(7):1062–73

25. Kalliokoski A, Niemi M. 2009. Impact of OATP transporters on pharmacokinetics. *Br J Pharmacol*. 158(3):693–705